Geo-electromagnetic monitoring of the Andean Subduction Zone in Northern Chile

Dissertation
zur Erlangung des akademischen Grades
doctor rerum naturalium (Dr. rer. nat.)
im Fachbereich Geowissenschaften
der Freien Universität Berlin

vorgelegt von

Dipl. Geophysiker
Dirk Brändlein

Berlin, 2013

Gutachter:

PD Dr. Oliver Ritter (1. Gutachter)
Freie Universität Berlin, Fachbereich Geowissenschaften, Fachrichtung Geophysik
Deutsches GeoForschungsZentrum GFZ

Prof. Dr. Serge A. Shapiro (2. Gutachter)
Freie Universität Berlin, Fachbereich Geowissenschaften, Fachrichtung Geophysik

Tag der Disputation: 02.07.2013

Abstract

Adapting the magnetotelluric (MT) method for monitoring the dynamic behaviour of the Andean subduction system in Northern Chile is focus of this thesis. Electromagnetic fields, sampled at nine permanent MT stations which cover an area of approximately 250 x 100 km^2 in the Andean fore-arc, are evaluated to monitor the electrical resistivity structure associated with the deep hydraulic system of the subduction zone. The long term monitoring of geo-electromagnetic fields reveals different types of temporal variations of vertical magnetic transfer functions (VTF) in different period ranges which are evaluated and interpreted.

Computation of time series of daily VTFs of an overall length of 4 years exhibit seasonal variations with amplitudes of more than 100 % of their absolute values for different components at all sites of the array. The observed seasonal variation affects almost exclusively the east-west magnetic field component for periods between 100 and 3000 seconds. These ground-based measurements of magnetic and electric fields exhibit statistically significant coherences with the interplanetary electric field (IEF) derived from solar wind and interplanetary magnetic field data of the Advanced Composition Explorer (ACE) satellite. The IEF penetrates the polar ionosphere from where it propagates towards equatorial latitudes by wave guide transmission, with ionosphere and solid Earth acting as conducting boundaries. Signal coherence between IEF and ground data peaks at periods of approximately 90 min and up to the four harmonics. Coherence values reach 0.4 at these periods and depend on the electromagnetic field component. They vary with season and local time. Transfer functions computed between IEF and ground-based electric and magnetic fields show local maxima at similar periods (90 min and harmonics). The coupling between the east-west magnetic field component and the IEF shows significant seasonal variability, much larger than for the other electromagnetic field components. We conclude that the IEF drives primarily a global circuit of Pedersen currents in the ionosphere. Resulting time-varying magnetic fields induce electric currents in the ground. Related ground-based magnetic (primarily north-south) and electric (primarily east-west) signals vary coherently at all local times and seasons. Conversely, magnetic signals caused by the IEF-driven Hall currents depend much on local time and season. We show for the first time that these ionospheric Hall currents cause no induction in the ground, but they generate magnetic signatures that are confined to the waveguide between ionosphere and Earth's surface.

Geo-electromagnetic depth sounding applications as MT assume both spatial and temporal uniform external electromagnetic source fields. The seasonal variation of VTFs exhibits a systematic violation of this basic assumption in Northern Chile. The consequence is a systematic seasonal rotation and length variation of the induction arrows of the period

band between 100 and 3000 seconds. If not taken into account, the structure of an electrical resistivity model of the subsurface, obtained by MT inversion, would be distorted. Removing this source field effect with a low-pass filter allows evaluation of residual variations of the VTF time-series which last longer than one year. During 2008 and 2009, I observe a significant variation of the VTFs in the southern part of the network for periods between 1500 and 4000 seconds. To simulate this variation, a 3D reference resistivity model is obtained by inversion of MT and VTF data using eight stations of the network. A region of high conductivity matches spatially with the hydrated mantle wedge. By trial and error, the 3D reference image of the deep electrical resistivity structure is modified and 3D forward modelling is applied to explain temporal variations in the VTFs similar to our observations. That requires modification of the electrical resistivity structure in a region which coincides roughly with the plate interface directly down-dip of the M_w7.7 2007 Tocopilla earthquake. We speculate that the anomalous temporal variations of the VTFs may be caused by large scale fluid relocation in the aftermath of the seismic event.

Kurzfassung

Die Anpassung der magnetotellurischen Methode (MT) zum Monitoring des dynamischen Verhaltens der Subduktionszone der Anden ist Fokus dieser Doktorarbeit. Dafür werden an neun permanenten MT Stationen, die ein Gebiet von ca. 250 x 100 km^2 im Forearc-Bereich der Anden abdecken, elektromagnetische Felder abgetastet. Die Auswertung dieser Daten soll zur Überwachung des elektrischen Widerstandes dienen, welcher mit dem hydraulischen System der Subduktionszone in der Tiefe zusammenhängt. Die Langzeitaufzeichnung geo-elektromagnetischer Felder offenbart verschiedene Arten zeitlicher Variationen vertikaler magnetischer Übertragungsfunktionen (VTF) in unterschiedlichen Periodenbereichen, welche ausgewertet und interpretiert werden.

Die Berechnung täglicher VTFs und ihre Zusammenfassung zu Zeitreihen einer Gesamtlänge von 4 Jahren zeigen jahreszeitliche Variationen mit Amplituden von mehr als 100% der Absolutbeträge in verschiedenen Komponenten an allen Stationen des Arrays an. Die beobachteten jahreszeitlichen Variationen betreffen fast ausschliesslich die Ost-West Komponente des Magnetfelds für Periodenlängen zwischen 100 und 3000 Sekunden. Die bodengestützten Messungen von magnetischen und elektrischen Feldern zeigen statistisch signifikante Kohärenzen mit dem interplanetaren elektrischen Feld (IEF), das aus Sonnenwind- und interplanetaren Magnetfelddaten des Advanced Compositon Explorer (ACE) Satelliten berechnet wird. Das IEF dringt in die polare Ionosphäre ein, von wo es sich in einem Wellenleiter, dessen leitfähige Begrenzungen von der Ionosphäre und der Erdoberfläche gebildet werden, hin zu äquatorialen Breiten fortpflanzt. Die Signalkohärenz zwischen IEF- und bodengestützten Daten ist maximal für Periodenlängen von ca. 90 min und bis zur vierten Harmonischen. Bei diesen Perioden reichen die Kohärenzwerte bis zu 0.4, hängen aber von der elektromagnetischen Feldkomponente ab. Sie variieren jahreszeitlich und mit der Ortszeit. Übertragungsfunktionen zwischen IEF und bodengestützten elektrischen und magnetischen Feldern zeigen lokale Maxima bei ähnlichen Periodenlängen (90 min und Harmonische). Die Kopplung zwischen der Ost-West Komponente des Magnetfeldes und IEF offenbart signifikante jahreszeitliche Veränderung, die viel grösser als für die anderen elektromagnetischen Feldkomponenten ist. Wir schliessen daraus, dass der IEF hauptsächlich ein globales System von Pedersen-Strömen in der Ionosphäre erzeugt. Die resultierenden zeitveränderlichen Magnetfelder induzieren elektrische Ströme im Boden. Die zugehörigen bodengestützten magnetischen (hauptsächlich Nord-Süd) und elektrischen (hauptsächlich Ost-West) Signale variieren kohärent zu allen Lokalzeiten und mit der Jahreszeit. Umgekehrt hängen die magnetischen Signale, welche durch vom IEF erzeugte Hall-Ströme verursacht werden, sehr stark von der Lokalzeit und der Jahreszeit ab. Wir zeigen erstmals, dass diese ionosphärischen Hall-Ströme keine Induktion im Un-

tergrund verursachen, jedoch magnetische Signaturen erzeugen, die auf den Wellenleiter zwischen Ionosphäre und Erdoberfläche beschränkt sind.

Geo-elektromagnetische Tiefensondierungsmethoden wie MT setzen über die Zeit räumlich gleichförmige externe elektromagnetische Quellfelder voraus. Die jahreszeitliche Variation der VTFs zeigt eine systematische Verletzung dieser Grundannahme in Nord-Chile an. Die Konsequenz ist eine systematische jahreszeitliche Rotation und Längenänderung der Induktonspfeile im Periodenband zwischen 100 und 3000 Sekunden. Wird dies nicht berücksichtigt, kommt es zu einer Verzerrung der Struktur eines elektrischen Widerstandsmodells des Erdinneren, welches durch Inversionsrechnung gewonnen wird. Die Beseitigung des Quellfeldeffektes durch einen Tiefpassfilter ermöglicht die Auswertung verbleibender Variationen in den VTF Zeitreihen, welche länger als ein Jahr andauern. In den Jahren 2008 und 2009 beobachte ich eine signifikante Variation der VTFs im südlichen Teil des Netzwerkes für Periodenlängen zwischen 1500 und 4000 Sekunden. Um diese Variation zu simulieren, wird mit 3D Inversion der MT und VTF Daten von acht der Netzwerkstationen ein 3D Referenzmodell des elektrischen Widerstandes berechnet. Eine Region mit hoher elektrischer Leitfähigkeit stimmt dabei räumlich mit dem hydratisierten Mantelkeil überein. Mit der Trial-and-Error-Methode wird das 3D Referenzmodell der tiefen elektrischen Leitfähigkeitsstruktur verändert und Vorwärtsrechnungen durchgeführt, um Variationen der VTFs, ähnlich den Beobachteten, zu erklären. Dies erfordert die Modifizierung der elektrischen Widerstandsstruktur in einer Region, welche grob mit der Grenzschicht der tektonischen Platten direkt unterhalb des Hypozentrums des M_w7.7 Tocopilla Erdbebens übereinstimmt. Wir spekulieren, dass die anomale zeitliche Variation der VTFs wahrscheinlich durch grossvolumige Fluidverlagerungen in der Folge des seismischen Ereignisses verursacht wurde.

Contents

Introduction

Fluids play a key role in ocean-continent subduction zones. The down going oceanic lithosphere contains hydrous minerals which form at mid ocean ridges by hydrothermal alteration. The oceanic plate absorbs additionally fluids by seafloor weathering (e.g. Stern, 2002) and ocean basin sediments (von Huene & Scholl, 1991). Following Schmidt & Poli (1998), the subducted material continuously releases water down to maximum depths of approximately 300 km, depending on the thermal state of the slab. These authors also infer that below the fore-arc 30-70 % of the subducted fluids are released. Hacker (2008) pointed out that approximately 50 % of the subducted fluid is expelled by the closure of pores at shallow depths, causing serpentinisation of the overlying mantle wedge (Peacock, 1990). The transport of fluids to greater depths occurs mostly sequestered in hydrous minerals of altered crust and serpentinized mantle (Stern, 2002; Rüpke, 2004). With increasing pressure and temperature at greater depths, the interaction of devolatilization of fluids from the subducted materials and asthenospheric mantle generates magmas at convergent margins. Approximately 35 % of the remaining subducted fluids reach post-arc depths (> 135 km) (Hacker, 2008).

At the subduction system in Northern Chile, the overriding continental lithosphere is significantly deformed during various phases of the seismic cycle. The oceanic Nazca plate subducts at a rate of approximately 6-7 cm/yr under the South American Plate (Angermann et al., 1999). Chlieh et al. (2004) found that during the inter-seismic period the thrust interface is fully locked down to a depth of approximately 35 kilometres. As a consequence, the motion of the down going plate is accommodated by deformation and faulting of the overriding plate (e.g. Allmendinger & González, 2010; Chlieh et al., 2004). The inter-seismic period lasts for 100 - 150 years (Comte & Pardo, 1991), during which elastic strain accumulates before it is released in subsequent co-seismic periods of the earthquake cycle. The release of elastic energy of the M_w7.7 2007 Tocopilla earthquake caused decimetre scale deformation with a rupture area of approximately 160 km by 50 km along the convergent margin on the plate interface in a depth of 30 - 50 km (e.g. Schurr et al., 2012). Chlieh et al. (2004) observed that the subsequent post-seismic period showed widespread aseismic slip on the plate interface for 3.3 years after the 1995 M_w8.1 Antofagasta Earthquake. Such post-seismic activity can be due to large scale fluid flow as suggested by Husen & Kissling (2001) who observed increased vp/vs ratios

30 days after the Antofagasta Earthquake. In contrast, fluid relocation and according pore pressure changes are also capable of triggering earthquakes (e.g. Segall, 1989) as dehydration processes and associated fluid release may reduce the effective stress of rocks, resulting in brittle fracturing (Raleigh & Paterson, 1965).

The presence of fluids strongly affects the electrical conductivity of rocks. Already small amounts of brines (in interconnected veins) can suffice to increase the bulk conductivity of rocks or an entire region of the subsurface by several orders of magnitude (e.g. Guéguen & Palciauskas, 1994). Over the past years, several research teams reported from non-volcanic tremor signals at active plate boundaries (Obara, 2002; Rogers & Dragert, 2003; Nadeau & Dolenc, 2005). As sources of these signals, flow-induced oscillation in channels transporting (magmatic) fluid at a depth range of 20 - 40 km were suggested.

A correlation between deep fluids, tremor and creep along the central San Andreas Fault could be established with magnetotelluric (MT) data (Becken et al., 2011). Zones of high electrical conductivity provide evidence for fluids migrating into the creeping section of the fault that originate from a region that is also responsible for stimulating tremors. These findings can explain why motion along the fault results in strong and potentially damaging earthquakes on locked and dry segments and in less harmful abundant microseismicity towards the creeping segments of the fault. High fluid pressures appear to play a crucial role in the weakening of faults as along-strike variations in tremor activity are related to strength variations in the lower crust and upper mantle.

The Integrated Plate Boundary Observatory Chile (IPOC, http://www.ipoc-network.org/) was established to monitor the dynamic behaviour of an active deep subduction system with a network of combined geophysical and geodetic sensors. The entire IPOC network consists of 19 multi-parameter stations distributed over an area of 700 km^2 at the north Chilean fore-arc. Installation of sites began in 2006, carried out by the Helmholtz Centre Potsdam - GFZ German Research Centre for Geosciences. The geophysical instruments are deployed in caverns excavated into bedrock to minimize climatic influences. The stations are connected via satellite link to the GFZ. Besides seismicity, ground motion, tilt and creep, electrical conductivity is one of the physical parameters under investigation. Electromagnetic field data is gathered at 9 of the 19 observations sites.

The MT monitoring measurements within the IPOC started early 2007 with the installation of instruments at seven (PB01 - PB07) of the pre-existing 19 multi parameter sites which also provide GPS and seismological data. The observatory stations are located in the Coastal Cordillera and Longitudinal Valley between Antofagasta and Iquique in the north Chilean segment of the Andean fore-arc. Site PB09 was installed early 2010 and PB15 in 2011. The objective of the project is to monitor and analyse electromagnetic

(EM) data to decipher possible changes in the subsurface resistivity distribution, e.g. as a consequence of large scale fluid relocation.

MT monitoring has been attempted before. Continuous recordings of electric field data from 1988-1995 at the San Andreas Fault in Parkfield (California) did not show any statistically significant variations of the telluric currents (Park, 1991, 1996). A two year (1996-1997) MT monitoring experiment near Parkfield did also not show any significant observational changes that were unambiguously above random background noise levels (Eisel & Egbert, 2001). Kappler et al. (2010) reported seasonal variations of apparent resistivity which they interpreted as a consequence of varying rainfall. Egbert (2002) pointed out that redundant measurements based on arrays of sites rather than relying on single stations are required to improve signal to noise ratios and control of statistical properties. The MT component of IPOC consists of a network of MT stations specifically designed to monitor the subsurface electrical resistivity structure. The data presented here suggest strongly and for the first time that it is possible to decipher changes in the deep hydraulic system of a ocean-continent subduction zone with MT.

Interaction of solar wind and earth's dipole magnetic field generates a wide range of geomagnetic variations with periods ranging from several years to fractions of seconds. Earth's magnetosphere and ionosphere are the predominant origins of geomagnetic variations which induce electric currents into the conductive earth's interior. Passive electromagnetic depth sounding methods use these currents to probe the electrical conductivity structure of Earth's subsurface. Electromagnetic parameters of the subsurface can be determined from the ratio of horizontal electric and magnetic field components using the MT method (Tikhonov, 1950; Cagniard, 1953). Vertical magnetic fields are entirely of internal origin and reflect lateral variations of the electrical conductivity structure (Schmucker, 1969). The sources of the geomagnetic field variations are located at such great distance from the point of observation at earth's surface that the external magnetic fields can be assumed as spatially uniform at mid-latitudes. Making plane wave assumptions for far-field sources, the obtained transfer functions are constant in space over geological time scales. However, deviations of the external magnetic fields from spatial homogeneity have been reported before. For example, MT measurements from two MT monitoring sites at the San Andreas Fault, California, showed source field inhomogeneities for periods of 10 - 30 seconds (Egbert et al., 2000). These authors explained the observation as an interaction of geomagnetic Pc3 pulsations and strong man made electromagnetic noise caused by a DC railway system. The source field inhomogeneity found its expression as local daytime dependent variations of horizontal magnetic transfer functions.

Already Nishida (1968b) reported on coherent magnetic field variations with periods of approximately 1 h, occurring almost simultaneously at equatorial and auroral latitudes.

These ground-based observations were classified as DP2 fluctuations. Nishida (1968a) also suggested varying characteristics of interplanetary electromagnetic field penetrating the ionosphere as the origin of these DP2 fluctuations. Ever since, this matter is a subject of controversy (e.g. Matsushita & Balsley, 1972; Kawasaki & Akasofu, 1972). Kikuchi et al. (1978) suggested a model for coupling between magnetospheric electric fields and the polar and equatorial ionosphere. The model comprises instantaneous horizontal transmission of the polar ionospheric electric field to the equatorial ionosphere. The polar electric field generates equatorward directed Hall currents in the ionosphere and inverse currents in the ground. These two current systems are connected by vertical displacement currents. Prompt penetration of polar magnetic DP2 fluctuations to equatorial latitudes was studied in more detail by Kikuchi et al. (1996). They explain the instantaneous, direct propagation of DP2 type signals from polar to equatorial latitudes with a parallel plate transmission line model, where ionosphere and solid Earth act as electrical conductors. Kikuchi et al. (1996) concluded that the polar electric field causes a Hall current at polar and middle latitudes and the equatorial response results from a Pedersen current enhanced by the Cowling effect. Nicolls et al. (2007) reported the frequency-dependent relationship between interplanetary electric field (IEF) data recorded by the Advanced Composition Explorer (ACE) satellite in the solar wind at L1 and ground-based magnetometer data beneath the equatorial electrojet from two sites in Peru. These authors computed a transfer function between IEF and EEJ intensity which displayed a peak at a period of approximately 2 h. Manoj et al. (2008) found significant coherences between equatorial and interplanetary electric fields with multiple peaks for periods between 2 h and 20 min. These observations were based on vertical ionospheric drift measurement by a low-latitude radar (JULIA), recorded between 08 and 15 local time, and interplanetary data recorded with the ACE satellite. Manoj et al. (2008) found the largest penetration effect at local noon time, but no significant seasonal dependence was observed.

In this study we show for the first time the influence of interplanetary electric field penetration to low geomagnetic latitudes on individual magnetic and electric field components of ground-based measurements in northern Chile. With the new data we can establish a clear seasonal dependency between the penetration effect and the electromagnetic field components and also a significant difference between daytime and nighttime. At low geomagnetic latitudes the conductivity of the ionosphere shows a high degree of anisotropy depending on season and local time. By investigating the response of the various magnetic and electric components at the surface to interplanetary electric field we determine the induction effect of the Hall and Pedersen currents.

CHAPTER 1

Geo-Electromagnetic depth sounding applications

In the 1950s Tikhonov (1950) and Cagniard (1953) introduced magnetotellurics (MT), a geophysical method based on the principle of electromagnetic induction in the Earth. The induction processes are the consequences of natural variations of geomagnetic fields caused by interaction of solar wind and Earth's magnetosphere. Ratios between electric and magnetic fields observed at Earth's surface are used to probe the electrical conductivity structure in the ground from tens of metres to tens of kilometres depth. In addition, the interpretation of ratios between horizontal and vertical magnetic field components which reveals lateral resistivity contrasts in the ground is referred to as geomagnetic depth sounding (GDS).

1.1 Electromagnetic induction in the Earth

The fundamental principles of electrodynamics are described by Maxwell's equations. For polarisable and magnetisable, isotropic and homogeneous media they can be written in differential form as:

$$\nabla \cdot \vec{E} = \frac{\varphi}{\epsilon} \quad , \tag{1.1}$$

$$\nabla \times \vec{E} = -\frac{\partial \vec{B}}{\partial t} \quad , \tag{1.2}$$

$$\nabla \cdot \vec{B} = 0 \quad , \tag{1.3}$$

$$\nabla \times \vec{B} = \mu \vec{j} + \mu\epsilon \frac{\partial \vec{E}}{\partial t} \quad . \tag{1.4}$$

$\vec{E}$ denotes the electric field $[Vm^{-1}]$, $\vec{B}$ the magnetic flux density $[T]$ [1], $\vec{j}$ the electric current density $[Am^{-2}]$ and φ electric charge density $[Cm^{-3}]$. $\epsilon = \epsilon_0\epsilon_r$ $\left[\frac{As}{Vm}\right]$ denotes the

[1] B is referred to as magnetic field.

permittivity and $\mu = \mu_0\mu_r \left[\frac{Vs}{Am}\right]$ the permeability. For Earth's materials applies $\epsilon_r \leq 20$ and $\mu_r \approx 1$, consequently holds $\epsilon \approx \epsilon_0$ and $\mu \approx \mu_0$.

Using Ohm's law $\vec{j} = \sigma\vec{E}$, where $\sigma[Sm^{-1}]$ denotes the electrical conductivity, Maxwell-Ampere's equation (eq. 1.4) can be transformed to:

$$\nabla \times \vec{B} = \mu_0\sigma\vec{E} + \mu_0\epsilon_0\frac{\partial\vec{E}}{\partial t} \quad . \tag{1.5}$$

Applying the vector Laplace operator to an arbitrary vector field $\vec{A}$:

$$\Delta\vec{A} = \nabla(\nabla\vec{A}) - \nabla \times (\nabla \times \vec{A}) \quad , \tag{1.6}$$

equation (1.5) can be transformed to

$$\Delta\vec{B} = \mu_0\sigma\frac{\partial\vec{B}}{\partial t} + \mu_0\epsilon_0\frac{\partial^2\vec{B}}{\partial t^2} \quad . \tag{1.7}$$

If transforming analogously Faraday's law (1.2), both results can be written as:

$$\Delta\vec{F} = \mu_0\sigma\frac{\partial\vec{F}}{\partial t} + \mu_0\epsilon_0\frac{\partial^2\vec{F}}{\partial t^2} \quad , \tag{1.8}$$

with $\vec{F}$ denoting $\vec{E}$ or $\vec{B}$. The first term describes diffusion and the second term wave propagation of electromagnetic fields in a medium.

The sources for induction processes in the ground in the considered period range 10^1 - 10^5 s are geomagnetic variations caused by interaction of Earth's magnetosphere and solar wind. Consequently, the penetration depth is small against the source dimensions (Schmucker, 1987) and the source fields can be assumed at the point of observation at Earth's surface as plane waves with a time dependency $e^{i\omega t}$. In MT case, the first term in equation (1.8) becomes dominant which results in:

$$\Delta\mathbf{F} = i\omega\mu_0\sigma\mathbf{F} = k^2\mathbf{F} \quad , \tag{1.9}$$

where $\mathbf{F}$ denotes the Fourier transform of $\vec{F}$, $\omega = \frac{2\pi}{T}$ denotes the frequency (T = period) and $k = \sqrt{i\omega\mu\sigma}$ the complex wave number. The inverse real part of k is a measure for the penetration depth of electromagnetic waves and is called skin depth $\delta(\omega)$:

$$\delta(\omega) = \frac{1}{Re(k)} = \sqrt{\frac{2}{|k^2|}} = \sqrt{\frac{2}{\omega\mu\sigma}} \quad , \tag{1.10}$$

which represents the depth where the electromagnetic field has decayed to $1/e$ of the amplitude at the surface.

1.2 Transfer functions of magnetotellurics and geomagnetic depth sounding

External magnetic fields penetrate in vertical direction into Earth's subsurface and in turn electric and secondary magnetic fields are induced. Consequently, ratios between different electric and magnetic field components can be used to estimate electromagnetic properties of the subsurface. Transfer functions (TF) are constructed using these ratios. The MT impedance tensor **Z** is calculated as the ratio between horizontal magnetic and electric field components in the frequency domain:

$$\mathbf{E} = \mathbf{Z}\,\mathbf{B} \quad \Rightarrow \quad \begin{pmatrix} E_x(\omega) \\ E_y(\omega) \end{pmatrix} = \begin{pmatrix} Z_{xx}(\omega) & Z_{xy}(\omega) \\ Z_{yx}(\omega) & Z_{yy}(\omega) \end{pmatrix} \begin{pmatrix} B_x(\omega) \\ B_y(\omega) \end{pmatrix} \quad , \tag{1.11}$$

with $Z_{ij} = \frac{E_i}{B_j}$ $(i, j = x, y)$. A right handed Cartesian coordinate system is used with x directed positive to north, y to the east and the vertical z is directed positive downward. As the impedance **Z** is a complex quantity, the components can be displayed as absolute value $|Z_{ij}|$ and phase ϕ_{ij}:

$$Z_{ij} = |Z_{ij}|\, e^{i\phi} = \left|\frac{E_i}{B_j}\right| e^{i\varphi} \;\; ; \quad \phi_{ij} = arctan\left(\frac{Im(Z_{ij})}{Re(Z_{ij})}\right) \quad . \tag{1.12}$$

From the absolute value of the impedance the apparent resistivity ρ_a $[\Omega m]$ of the subsurface is computed as:

$$\rho_{aij}(\omega) = \frac{\mu_0}{\omega}\,|Z_{ij}|^2 \quad . \tag{1.13}$$

For GDS, the ratio between complex frequency domain horizontal and vertical magnetic field components is considered. In a homogeneous medium, only horizontal electric currents are induced and no vertical magnetic field component exists. Non-zero vertical magnetic fields occur only if lateral conductivity contrasts in Earth's subsurface exist and, hence, they are completely of interior origin. Vertical magnetic transfer functions (VTFs) $\vec{T}_i(\omega)$ are calculated as follows:

$$B_z(\omega) = (T_x(\omega)\;\; T_y(\omega)) \begin{pmatrix} B_x(\omega) \\ B_y(\omega) \end{pmatrix} \quad . \tag{1.14}$$

VTFs can be displayed as real and imaginary induction arrows $\vec{P}$ and $\vec{Q}$:

$$\vec{P}(\omega) = Re\,[T_x(\omega)]\,\hat{x} + Re\,[T_y(\omega)]\,\hat{y} \qquad (real\ part); \tag{1.15}$$

$$\vec{Q}(\omega) = Im\,[T_x(\omega)]\,\hat{x} + Im\,[T_y(\omega)]\,\hat{y} \quad (imaginary\ part). \tag{1.16}$$

$\hat{x}$ and $\hat{y}$ denote the unit vectors in x and y direction, respectively. In this thesis the convention of Wiese is used to display $\vec{P}$ and $\vec{Q}$ (Wiese, 1962). Consequently, when plotted on a map the real induction arrow tend to point away from a highly conductive structure.

CHAPTER 2

A network of permanent MT monitoring sites in Northern Chile

In this chapter, geological and tectonic information about the survey area is given. Also the MT installations of the IPOC, which I partly set-up and maintained myself twice a year since May 2009, and the new electrode design, developed with support by our technicians from Niemegk, are described.

2.1 The Andean subduction system in Northern Chile

2.1.1 Geologic setting

The subduction system in Northern Chile consists of the continental South-American plate and the under-thrusting oceanic Nazca-plate. This subduction system formed the central Andes, the highest mountain Plateau created by a modern ocean-continent convergent plate boundary (Allmendinger et al., 1997) and the frictional properties of the thrust interface give rise to major earthquakes with moment magnitudes > 8.0 (e.g. Comte & Pardo, 1991).

The main geological units of the fore-arc are aligned according to the north-south striking contact of the two tectonic plates (Figure 2.1). These units are the Coastal Cordillera, the Longitudinal Valley and the Chilean Precordillera. They represent former locations of the volcanic arc which can be classified as follows (e.g. Scheuber & Reutter, 1992; Hartley & Evenstar, 2010):

- The approximately 3 km high and 50 km wide Coastal Cordillera consists of the remnants of the Jurassic arc with andesitic tufts and lavas of approximately 10 km thickness and large dioritic batholiths. The most significant structure is the Atacama

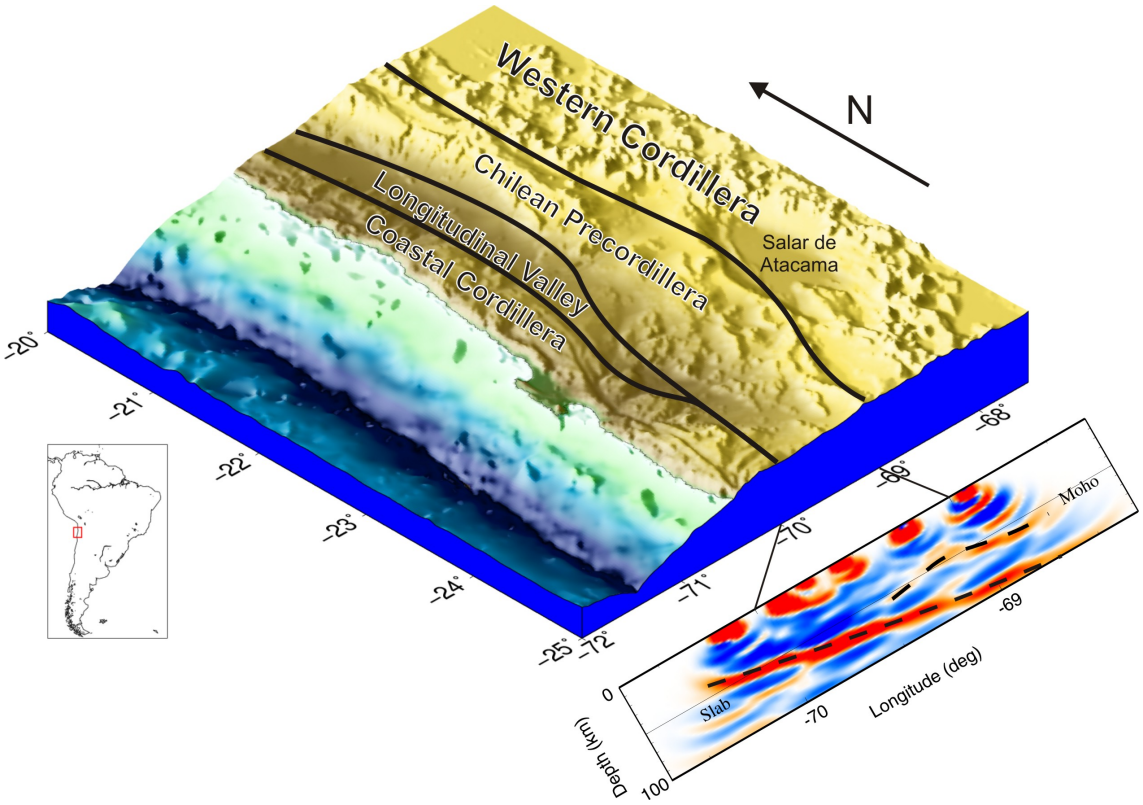

Figure 2.1: Principal geological units of the fore-arc of the Andean subduction system (borders simplified after Scheuber & Reutter, 1992). From west to east: the Coastal Cordillera represents the Jurassic-Early Cretaceous magmatic arc, the Longitudinal Valley the Mid-Cretaceous arc, the Chilean Precordillera the latest Cretaceous-Palaeogene arc and the Western Cordillera the recent Miocene-Holocene magmatic arc. The vertical section at the lower right corner shows migrated receiver functions at 22°S by Sodoudi et al. (2011); positive phases are indicated by red and negative phases by blue colours.

Fault zone, a strike parallel strike-slip zone extending from approximately 20°S to 30°S with a total length of more than 1,000 km (Fig. 2.2).

- The Longitudinal Valley has an elevation of approximately 1,000 m and is 50 km wide at 22°S. Most parts of the Mid-Cretaceous arc in the Longitudinal Valley are covered by younger formations, typically Oligocene to Holocene strata with more than 1,000 m thickness.

- The Precordillera is more than 4,000 m high and approximately 50 km wide at 22°S and represents the Late Cretaceous to Eocene volcanic arc. A number of reverse- and strike-slip-faults delimit blocks of Palaeozoic and Mesozoic strata, the major

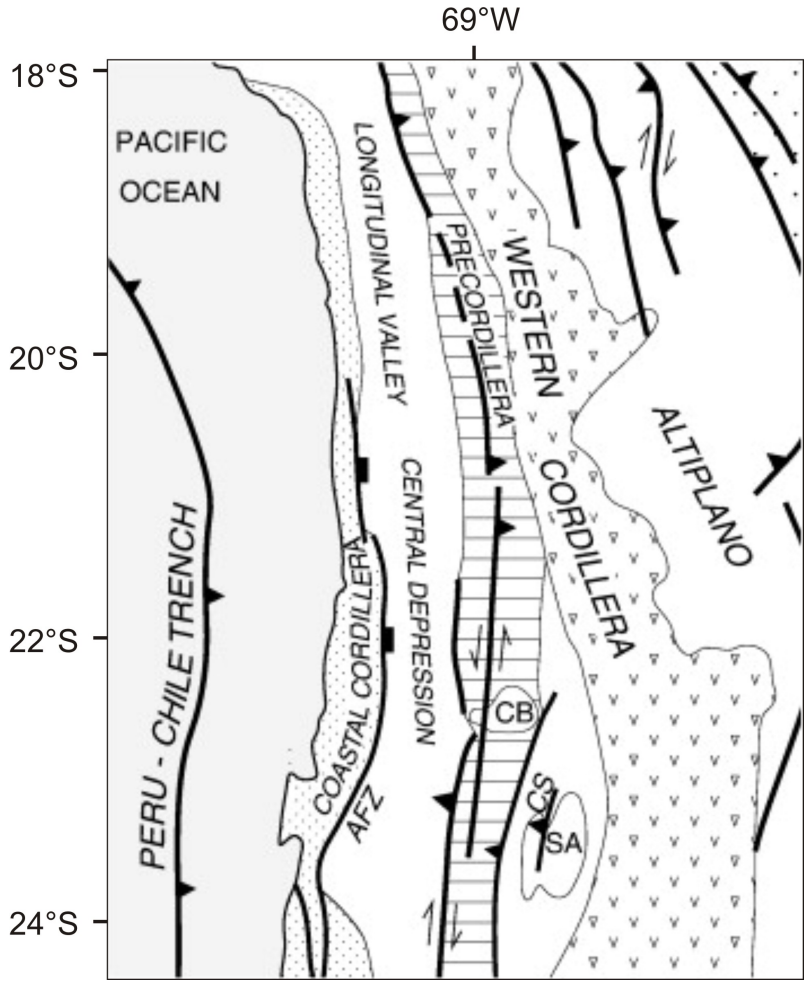

Figure 2.2: Morphotectonic units of the Central Andes (modified after Hartley & Evenstar, 2010). AFZ - Atacama fault zone, the strike-slip-fault in the Precordillera represents the Argomedo-West Fissure fault system, SA - Salar de Atacama, CS - Cordillera de la Sal, CB - Calama Basin.

active faults are strike-slip Argomedo and West Fissure fault system (Fig. 2.2).

- The most recent volcanic arc is the Western Cordillera which is approximately 50 km wide at 22°S. The average altitude is approximately 4,000 m with peaks higher than 6,000 m. Palaeozoic to Oligocene rocks, which form the basement, are unconformably overlain by lavas and ignimbrites of this newly formed arc. The andesitic and dacitic lavas and rhyolitic ignimbrites are up to 2,500 m thick.

2.1.2 Subduction geometry, earthquake cycle and fluids

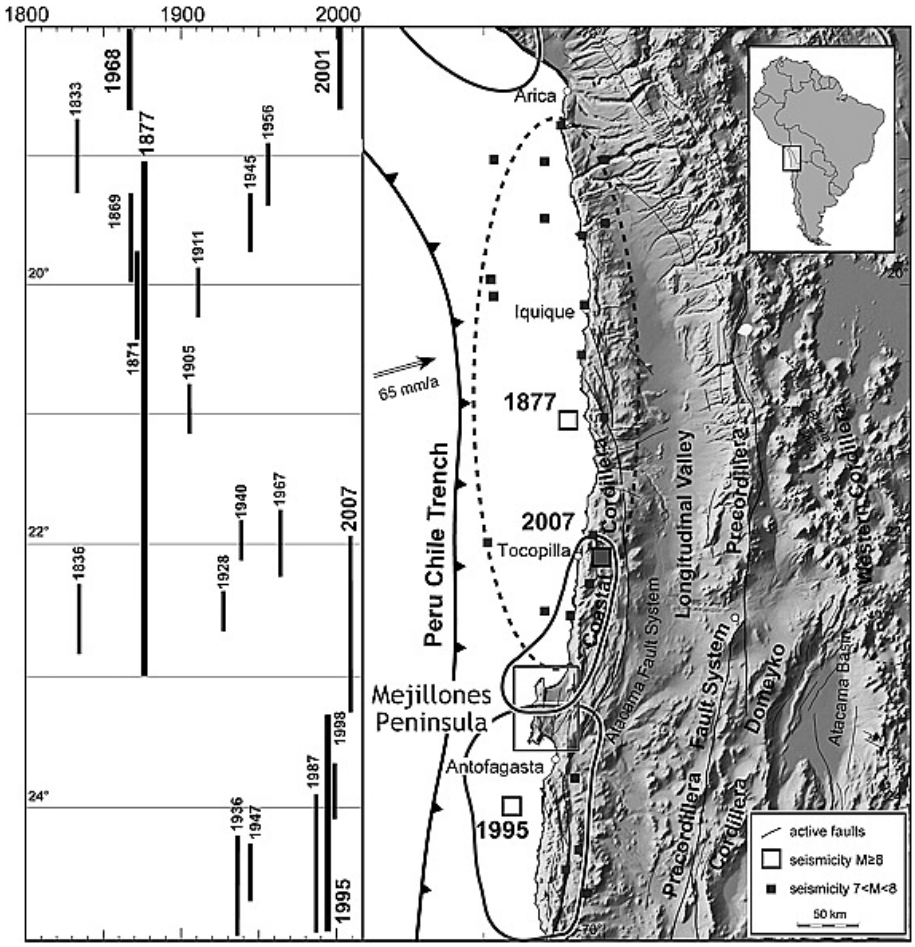

Figure 2.3: Rupture areas of major earthquakes since 1800 in Northern Chile (Victor et al., 2011). Sequence and lengths of ruptured segments are displayed on the left hand side.

Based on the age of subducted lithosphere, the Andean subduction system represents an end-member type (Stern, 2002): the young, hot and buoyant oceanic lithosphere of the Nazca plate underthrusts the continental plate and the convergence precedes with a velocity of approximately 6.7 cm/yr (Angermann et al., 1999). The buoyancy of the down-going plate results in a relatively shallow dip of the subduction and establishes a compressional arc type. The angle of subduction at the Andean subduction zone varies along strike, the segment in Northern Chile shows a gradual transition of this angle from steep subduction north of 20°S with approximately 30° slab dip to nearly flat subduction at approximately 28 - 32°S (Cahill & Isacks, 1992). There is only very little sediment load in the northern part of the Chilean Trench as consequence of the arid conditions of the Atacama Desert.

Consequently, subduction erosion affects the non-accretionary margin in this region (e.g. von Huene, 2003). The lack of significant sediment flux into the trench generates high frictional strength at the plate interface (Oncken et al., 2006). This configuration leads to an unstable behaviour of the seismogenic zone and an inter-seismically locked segment of the thrust interface which breaks in recurrent great earthquakes (Schurr et al., 2012). Another consequence of this strong coupling at the seismogenic zone are several strike-aligned strike slip faults in the fore-arc such as the prominent Atacama Fault System in the Coastal Cordillera (Fig. 2.2). The thrust interface of the Andean subduction system is segmented both in strike (Fig. 2.3) and in dip direction (Fig. 2.4).

In strike direction, segmentation is expressed by repeatedly ruptured individual segments of the subduction zone (Comte & Pardo, 1991) which appear to accommodate primarily the convergence between the Nazca plate and the South-American plate. The consequences are frequent earthquakes which are among the largest on Earth. In February 2010, a M8.8 earthquake ruptured the Constitución gap in south-central Chile. The segment of the Chilean margin which is estimated to rupture next is the 500 km long seismic gap in Northern Chile, approximately located between latitudes 18°S and 23°S (Comte & Pardo, 1991). This particular segment was last completely ruptured in 1877 by an $M > 8.5$ earthquake (Comte & Pardo, 1991). All other segments of the margin to the north and to the south have been broken within the last 20 years. In 1868, the segment to the north had been broken and was partly ruptured again in 2001 by an earthquake of a similar magnitude, the Mw8.4 Arequipa earthquake. The adjacent segment to the south was ruptured 1995 by the Mw8.1 Antofagasta earthquake (Delouis et al., 1997) which started below Mejillones Peninsula and propagated southward. Later in November 2007, the M7.7 Tocopilla earthquake (Schurr et al., 2012) ruptured southern parts of the segment which broke last in 1877, thereby releasing only 2.5 % of the moment deficit which accumulated on the plate interface in the previouse 130 years (Béjar-Pizarro et al., 2010).

In dip direction, subduction thrust faults can roughly be divided into segments according to the frictional properties of the interface, in down-dip direction these are: a shallow aseismic, an intermediate seismogenic and a deep transitional zone (Hyndman et al., 1997). Chlieh et al. (2004) found that during the inter-seismic period the thrust interface is fully locked down to a depth of approximately 35 kilometres. As a consequence, the motion of the down going plate is accommodated by deformation and faulting of the overriding plate (e.g. Chlieh et al., 2004; Allmendinger & González, 2010). The inter-seismic period lasts for approximately 100 - 150 years (Comte & Pardo, 1991); elastic strain accumulates within this time span and is released during the subsequent co-seismic period of the earthquake cycle. During the M7.7 2007 Tocopilla earthquake, the release

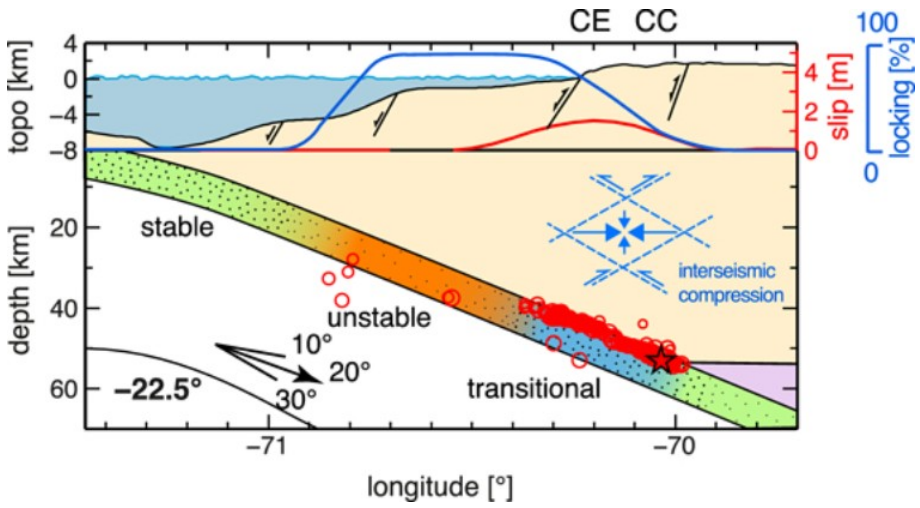

Figure 2.4: Cross-section through aftershocks of the M7.7 Tocopilla earthquake and fore-arc topography/bathymetry (Schurr et al., 2012). CC Coastal Cordillera, CE Coastal Escarpment. Red circles indicate projected aftershock locations from the section 15 km north and south of 22.5°S. The slip of the Tocopilla earthquake is indicated by the red curve, the locking of the seismogenic zone by the blue curve. The authors infer three frictional regimes: (*i*) "Stable (green): velocity-strengthening, earthquake-nucleation/propagation inhibited, no aftershock but afterslip, aseismic creep, variable locking." (*ii*) "Transitional/conditionally stable (blue): velocity-weakening, earthquake-nucleation/propagation at low pore fluid pressures, small to large earthquakes with incomplete stress drops/heterogeneous remnant stress field, aftershocks/afterslip, aseismic creep/partial locking." (*iii*) "Unstable (orange): velocity-weakening, earthquake-nucleation possible, rupture propagation sustained, great earthquakes with complete stress drop, few aftershocks/afterslip".

of elastic energy caused decimetre scale deformation (Motagh et al., 2010). The rupture area was estimated by these authors as approximately 160 by 50 km along the convergent margin on the plate interface in a depth of 30 - 50 km. Chlieh et al. (2004) observed that the subsequent post-seismic period showed widespread aseismic slip on the plate interface continuing for 3.3 years after the Mw8.1 Antofagasta Earthquake in 1995. The consequence of such post-seismic activity can be large scale fluid flow as concluded by Husen & Kissling (2001) based on increased vp/vs ratios during 30 days after the Antofagasta Earthquake. Monitoring and analysing EM data to decipher and image possible changes in the resistivity distribution of the subduction system, possibly caused by such relocation of big volumes of highly conductive fluids, is the objective of this thesis.

Fluids play a key role in such subduction zones as in Northern Chile. The subduct-

ing oceanic crust contains hydrous minerals which are formed at mid-ocean ridges by hydrothermal alteration. Additionally, water is added to the oceanic plate by seafloor weathering (e.g. Stern, 2002). Ocean basin sediments also contribute fluids to the subduction system (von Huene & Scholl, 1991). Following Schmidt & Poli (1998), the subducted material continuously releases water down to maximum depths > 300 km depending on the thermal state of the slab. These authors also infer that below the fore-arc 30 - 70 % of the subducted fluids are released. Hacker (2008) clarified that around 50 % of the subducted fluid is expelled by the closure of pores in shallow depths. Fluids released from the subduction slab hydrate the overlaying mantle wedge forming sepentinite (Peacock & Hyndman, 1999). The transport of fluids to greater depths occurs mostly sequestered in hydrous minerals in altered crust and serpentinised mantle material (Stern, 2002; Rüpke, 2004). Under the high pressure and temperature regime at greater depths, the interaction of fluids devolatilised from the subducted materials with the asthenospheric mantle is responsible for the magmas at convergent margins. Approximately 35 % of the remaining subducted fluids reach post-arc depths (Hacker, 2008).

2.2 Installations and configuration of the IPOC MT monitoring stations

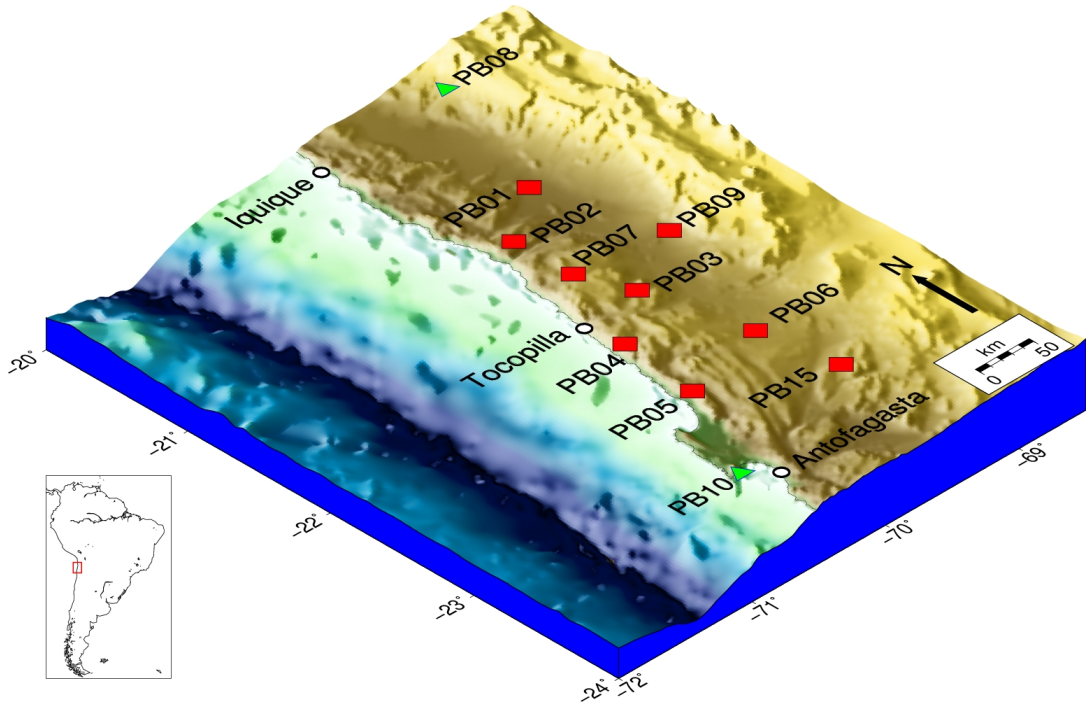

Figure 2.5: Locations of permanent MT monitoring stations of the Integrated Plate Boundary Observatory Chile in the North-Chilean Coastal Cordillera and Longitudinal Valley (c.f. Fig. 2.1), indicated by red symbols.

The Integrated Plate Boundary Observatory Chile (IPOC) was established to monitor the dynamic behaviour of an active deep subduction system with a network of combined geophysical and geodetic sensors. The IPOC network consists of 19 multi-parameter stations distributed over an area of 700 km^2 at the North-Chilean fore-arc. The installation of sites began in 2006, carried out by the Helmholtz Centre Potsdam - GFZ German Research Centre for Geosciences.

Besides seismicity, ground motion, tilt and creep, the electrical conductivity of the subsurface is one of the physical parameters under investigation to probe possible changes in the deep hydraulic system of the subduction zone which might be related to temporal modifications of the conductivity structure beneath. Electromagnetic field data is gathered at 9 of the 19 observation sites at the Coastal Cordillera and Longitudinal Valley in Northern Chile (Figure 2.5). MT sites PB01 to PB07 are operating since beginning of 2007, PB09 was installed in 2010 and PB15 in 2011.

The geophysical instruments are mostly deployed in caverns excavated in rock to minimize climatic influences and to prevent weathering due to the extreme climate of the Atacama Desert (Figure 2.6). The opening of the caverns is closed by an insulating door

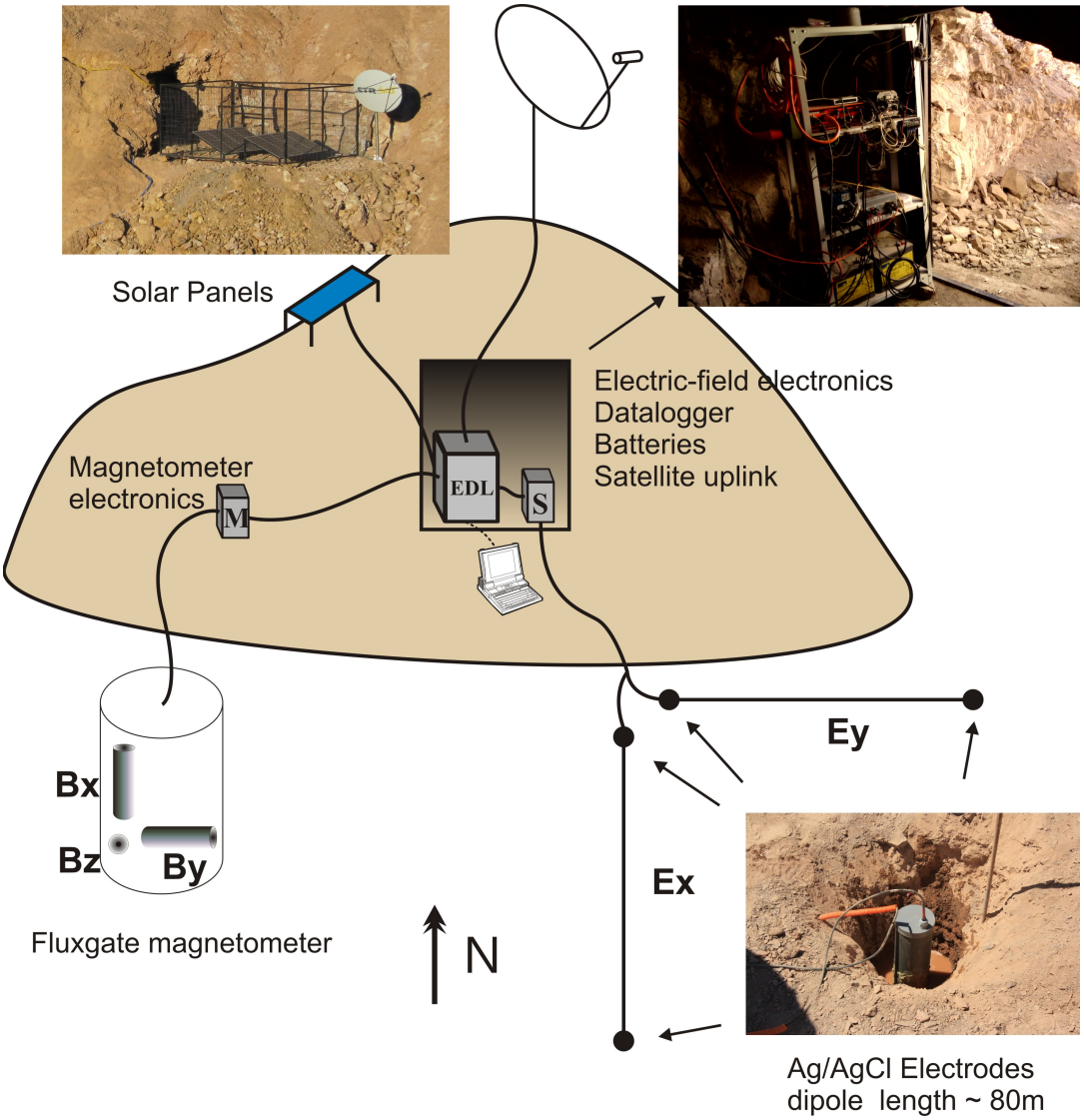

Figure 2.6: Principle set-up of an IPOC MT monitoring site. The sensors are installed outside of the cavern (not shown). The dipoles for electric field sampling are installed at the nearest flat area. All sensors and cables are buried to prevent influences of temperature variations. The cavern contains the data logger, electronics for electric field sampling, preamplifier and and the technical infrastructure. The data is transmitted via satellite uplink to the GFZ.

and the stations are connected via satellite link to the GFZ in Potsdam. Solar panels and batteries ensure uninterrupted power supply for all instruments favoured by the dry and stable climate in the Atacama Desert. The part of the MT equipment installed mostly inside the caverns are the signal processing device for sampling of the electric field (CASTLE sensorbox) and the data logger (Earth Data Logger - EDL). A GEOFON SeiscomP PC, which handles the near real-time communication via satellite, the batteries and the solar controller are also deployed in each cavern.

All MT sensors are placed outside the caverns as far as possible away from the power supply of the stations to avoid EM noise. The sensors are completely buried at a depth of approximately one metre to minimise temperature effects. At this depth the daily temperature variations reduce significantly and seasonal variations are neglectable (see section 2.2.1) as indicated by the temperatures measured at the electronic box of the magnetometer (Box M in Figure 2.6). The magnetometer is connected via a separated box, which contains the electronics, to the data logger. This box is also deployed outside the cavern and buried in the ground under an isolating layer of polystyrene.

The holes for the electrodes were excavated using a pneumatic hammer, at some sites explosives had to be used due to the rigidity of the bedrock and lack of sediments. Therefore, to have as few holes as possible, mostly a L-configuration set-up was used. The L-configuration requires three holes, one at the centre and two at the end of the electric dipoles (Figure 2.6). The magnetometers are buried at a distance of at least 20 metres away from the caverns. The control unit of the magnetometer is several metres away from the magnetic sensor to prevent any influence. It is also buried and additionally isolated with an overlying layer of polystyrene.

At station PB15 the cavern was excavated in a steep area which does not provide a reasonably plain surface for setting up the electrode dipoles. In this case the MT part is configured as a stand-alone station at a distance of approximately 300 metres (Figure 2.8) with a WLAN connection to the cavern and the satellite uplink thereafter.

Figure 2.7 *(following page)*: The four figures at the top show the installation of site PB09. The trenches for electric field dipoles were excavated at the nearest flat area. All cables are buried completely which is a major effort since channels of a total length of more than 250 m have to be excavated. The lower two figures on the left hand side show outdoor installations at sites PB07 and PB04, the figure at the lower right hand side shows the instruments and installations in the cavern at site PB01.

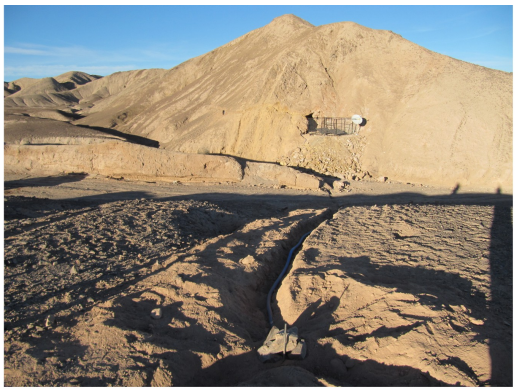

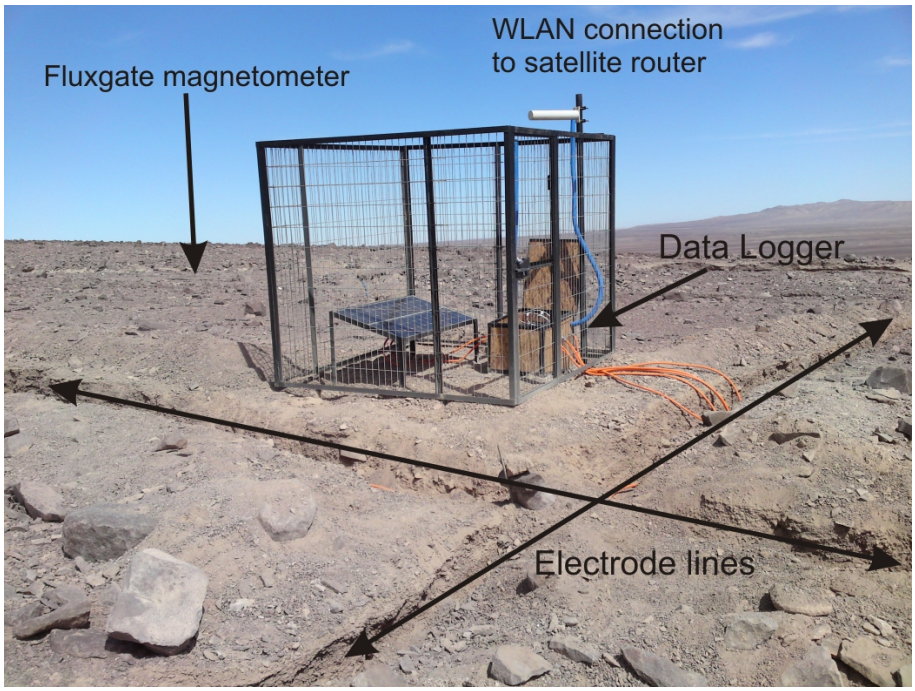

Figure 2.8: Stand-alone configuration of the MT instruments at site PB15. An isolated box contains the data logger, the electronics of the magnetometer and the Sensorbox for the electric field sampling. A separate power supply had to be installed, the data is transmitted via WLAN to the cavern which is located in a distance of approximately 300 m.

2.2.1 Instrumentation

A uniform set of sensors and electronic devices for data acquisition was installed at each IPOC MT monitoring site. The entire equipment was initially provided by the Geophysical Instrument Pool Potsdam (GIPP) of the GFZ German Research Centre for Geosciences. In 2010, it was handed over to the Universidad de Chile with the Seismological Service of Chile and to the Universidad Catolica del Norte.

The magnetic fields are sampled by three component Geomagnet fluxgate magnetometers with a passband of DC - 10 Hz. Instruments installed in this region are typically exposed to ground motion due to the intense earthquake activity. The specific construction of the magnetometers avoids tipping of the vertical magnetic component since the vertical level is aligned automatically by a pendulum. Furthermore, these magnetometers act as variometers since the static magnetic field is removed from the signal by subtracting a compensation field which depends on the instrument and location of the station.

The electric field is sampled with non-polarisable Ag/AgCl electrodes with an elec-

trolyte which consists of a saturated KCL solution. The input signal is preconditioned by a CASTLE Sensorbox which is deployed in the cavern. The Sensorbox is programmed to set-up amplification of the channels. Electrodes and CASTLE Sensorboxes are designed and manufactured by GFZ in Niemegk.

For recording, 6 channel GPS synchronised Earth Data Loggers (EDL, EarthData PR6-24) are used. These are 24 bit systems, originally developed for seismic data logging. The signals of the electromagnetic fields are continuously sampled at a rate of 20 Hz. The data stream of the EDLs is tapped by a SeiscomP PC (http://geofon.gfz-potsdam.de/geofon//seiscomp/pc104.html) using SEEDLink real-time protocol which sends 512 byte MiniSEED data files (section 3.1) via satellite link to the GFZ in Potsdam. All instruments installed at the time of writing are listed in the appendix.

Since 2007, the MT stations were maintained twice a year to control the operation of the instruments and to collect data by means of redundancy. Consequently, the temperature of magnetic sensors and electronic control units were controlled both in southern hemisphere winter and summer. The peak difference of seasonal daytime temperature of the magnetic field sensors is approximately 1.5°C. The control unit of the magnetometers exhibits a daytime peak difference from summer to winter of 2°C. The EDLs are configured to log the internal temperature of the instrument itself and the hard disk drive. Here the temperature of both electronic and hard drive show at day and night times a seasonal variation of around 2°C. The very small differences of temperature amplitudes can be explained on the one hand by almost complete absence of seasons in this region of the Atacama Desert at low height above sea level. On the other hand, the isolation of the instruments in the ground or in the cavern dampens temperature variations effectively.

2.2.2 Electric field measurements

The extremely dry ground of the Atacama causes huge problems for electric field measurements because contact resistances are mostly in the order of MΩ and electrolyte is leaking. As the electrodes must be left in the ground unattended for several months, regular refilling is not possible. After the first deployment in 2007, most electrodes ran dry after several weeks. They were replaced in 2008 by new ones which were coated in aluminium foil to prevent the electrolyte from leaking. Processing of 10 days of electromagnetic field data showed reasonable data quality, but after few months the foil oxidised which resulted in electrolyte leakage and poor data quality again. Since the bentonite at several sites was not completely dry, I made a second attempt to improve this approach.

In June 2009, new electrodes were inserted, now with a modified coating (Fig. 2.9). First, a layer of polythene film was placed around the bentonite to protect the aluminium

foil from humidity inside. The bottom was left out to ensure contact to the ground. The entire electrode was enclosed by two more layers of aluminium foil to prevent electrolyte from leaking. The data quality produced by these triple-coated electrodes was worse than the one-coated version (Figure 2.10).

We learned that the humidity inside the coating was preserved because it tends to evaporate upwards, most likely due to temperature. With this in mind, at the end of 2010, we placed the electrodes in plastic tubes which were closed upwards, but open downwards and filled with humid bentonite (Figure 2.11). The space between bentonite and the lid serves as water reservoir. The water from this reservoir evaporates at a very low rate since the bentonite is nearly impermeable. When the bentonite dries out and cracks appear, the water moisturises it again and impermeability is recovered.

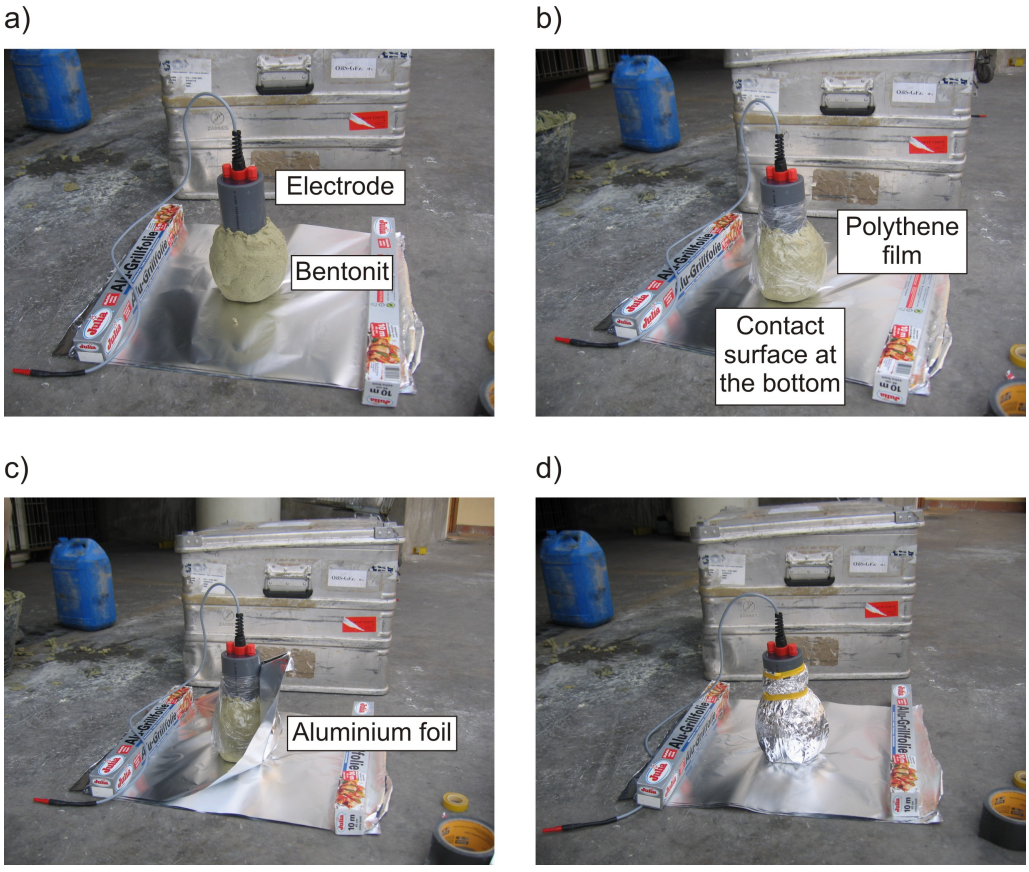

Figure 2.9: Preparation of the modified, triple-coated electrodes. The bentonite (a) is enclosed by a layer of polythene film (b) with an opening at the bottom. The polythene film was expected to prevent the outer layers of aluminium foil (c, d) from oxidation. Moisture kept longer, but data quality poor.

For the cable of the electrode a tight screw fitting is installed at the lid of the tube. A check-up eight months after the first installation exhibited remaining water on top of the bentonite. The data quality was maintained, given the the local noise conditions (Figure 2.10).

Figure 2.10 *(following page)*: Figure to illustrate the data quality of electric field measurements for different electrode configurations. Since the quality of the magnetic field recordings is maintained, temporal variations of ρ_a and ϕ are mainly caused by the electric field. a) Time series of daily apparent resistivity component ρ_{yx} and phase ϕ_{yx} for a period of 1020 s at site PB05. Vertical black lines indicate turn of the years, vertical green lines indicate times of installation of new electrodes. Each daily transfer function value is estimated by processing of 3 days of electric and magnetic field time series using the robust processing scheme EMERALD (section 3.1). The various apparent resistivity and phase curves in b - e originate from times indicated by vertical dashed black lines in a. The apparent resistivities and phases in b - e are processed using geo-electromagnetic field data from 10 days. b) Results directly after installation of the station when the electrodes were buried only with bentonite. The effect of leaking electrolyte is observed after several months (red double arrow in a). The poor data quality of the xy-components is a result of the strong current channelling in the Coastal Cordillera (Lezaeta, 2001) c) Data from electrodes enclosed by aluminium foil. The initial data quality is comparable to b, but the effect of gradual foil oxidation results in decreasing data quality which can be observed in a. d) The initial data quality of electrodes enclosed by polythene film and aluminium foil (Fig. 2.9) is significantly worse than in b and c. This is the consequence of the reduced contact surface due to the polythene film. After several weeks, the influence of oxidation of the aluminium foil shows its negative influence again. e) The new electrode configuration (Fig. 2.11) caused a constantly good data quality which now holds for more than a year (not shown).

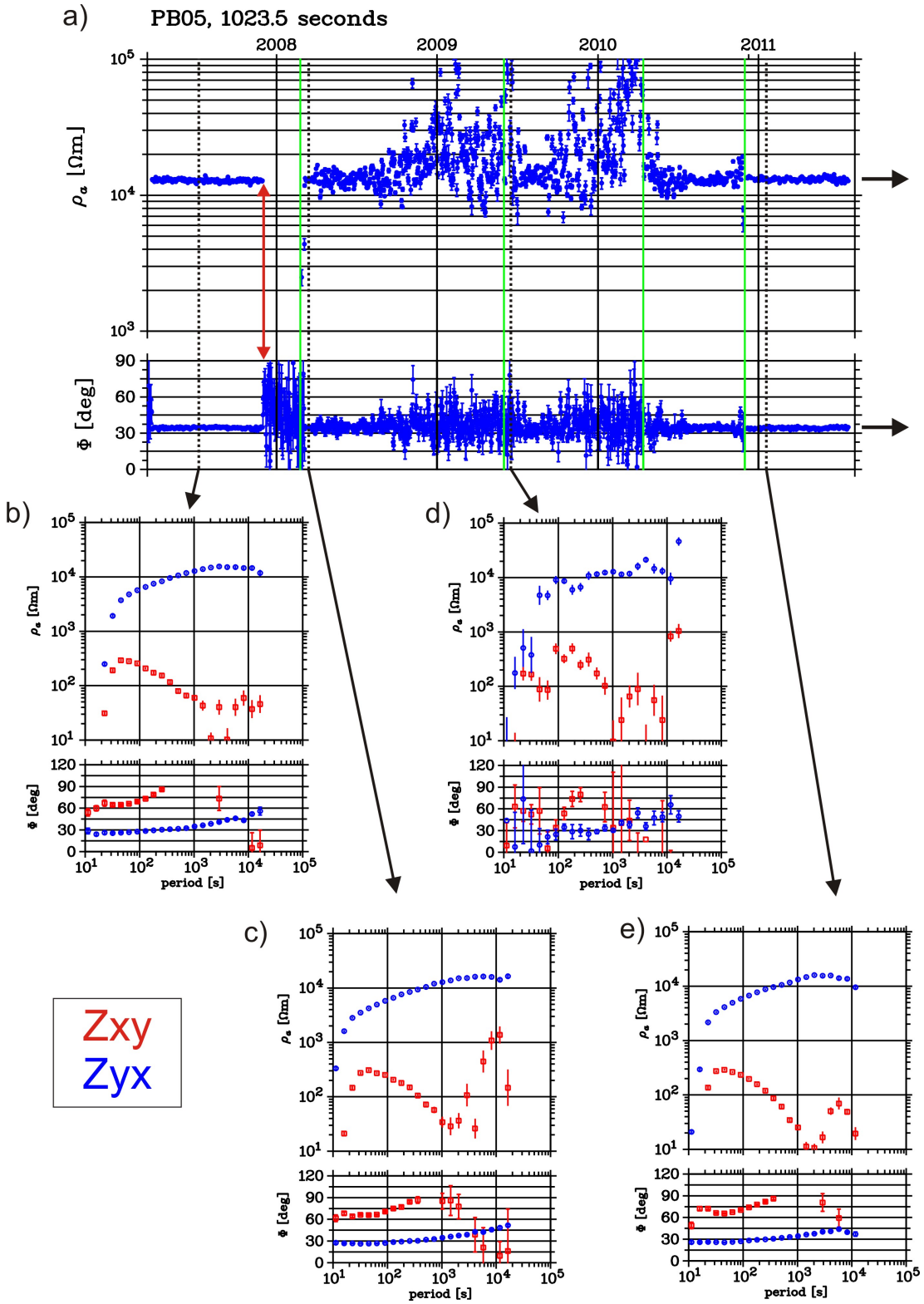
a)
PB05, 1023.5 seconds
2008
2009
2010
2011
ρ_a [Ωm]
Φ [deg]
b)
d)
c)
e)
period [s]
Zxy
Zyx

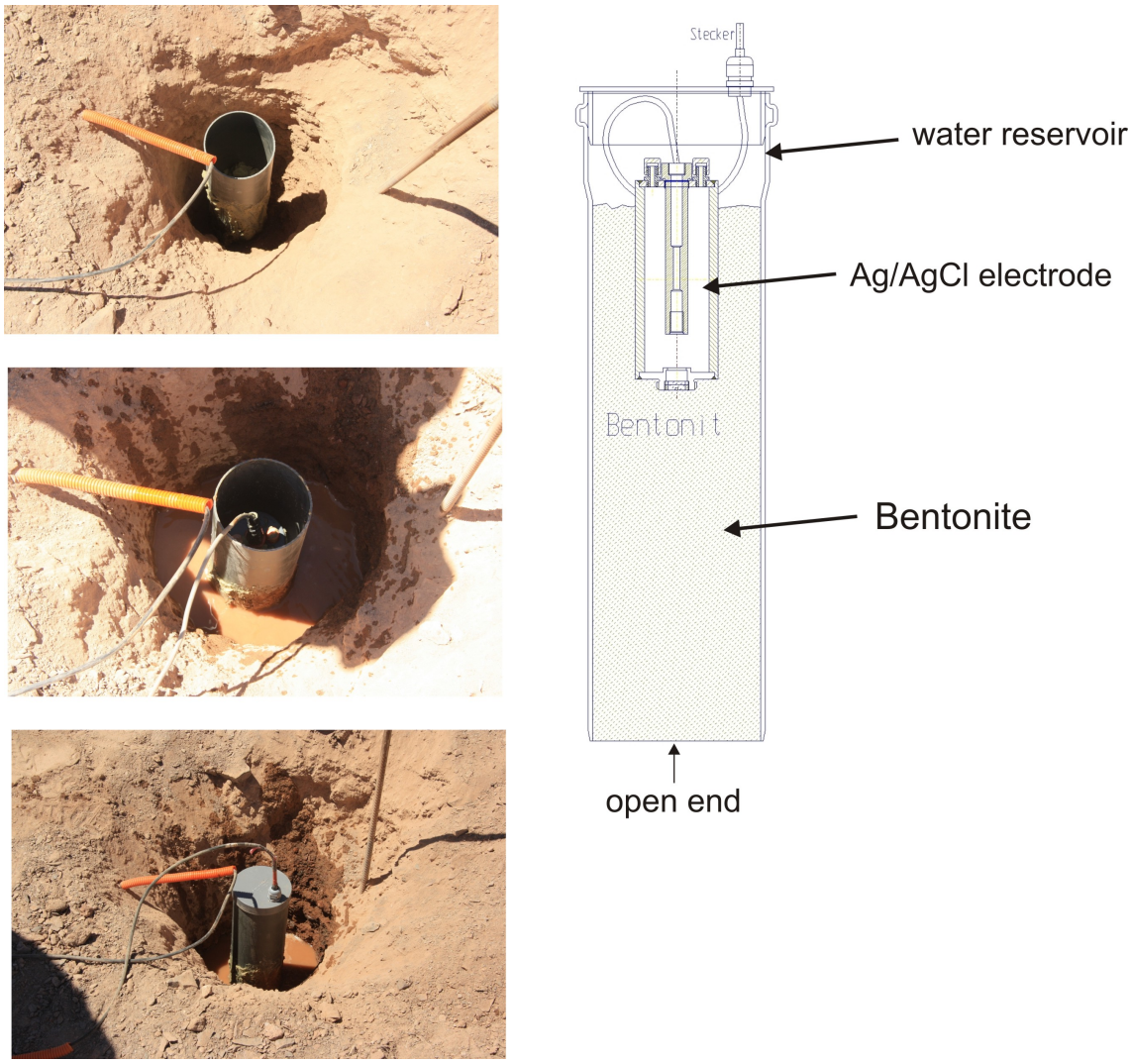

Figure 2.11: New electrode configuration for long term electric field measurements which proofed stable for over one year in the extreme arid climate of the Atacama Desert. On the left hand side the installation is shown. First the plastic tube is put into the hole. The tube is filled with bentonite, then the Ag/AgCl electrode is inserted, subsequently the remaining volume of the tube is filled with water. Finally the tube is closed with a water proof lid with a through-connection for the electrode cable. The right hand side shows a cross section through the new electrode design.

CHAPTER 3

Geo-Electromagnetic monitoring and source field inhomogeneities

The concept which I developed to organise monitoring data and evaluation is presented in this chapter. A predominant source field effect in the data is quantified and the cause is identified. Since long term stable electric field measurements became only possible in 2011 (see section 2.2.2), mostly magnetic field data is considered hereinafter.

3.1 Processing concept

MT transfer functions and VTFs (see section 1.2) are typically computed using time series of electric and magnetic fields of several days to weeks, depending on the depth and volume of the target and, thus, frequency. Reproducing this data by forward modelling or data inversion gives a snapshot of Earth's electrical resistivity structure. In contrast, the focus of this study is to adapt the MT method to monitor possible variations of the electrical resistivity structure in Earth's interior. Consequently, a different approach has to be applied; the entire electric and magnetic field time series are divided into segments of a fixed length which are used to calculate daily VTFs. To estimate a daily set of VTFs, the robust processing procedure EMERALD (Electro-Magnetic Equipment, Raw-data And Locations Database), described in Ritter et al. (1998), Weckmann et al. (2005), and Krings (2007), were used. This eventually results in time series of VTF components which are used for all further investigations.

An estimate for a daily VTF is obtained by processing of a three day long data segment which is several times band-pass filtered in a cascade decimation scheme. The individual band-pass filtered data are subdivided into shorter time windows and subsequently transformed into frequency domain. To improve statistical properties, the resulting cross- and auto-spectra of individual time frames are stacked in the frequency domain. The VTFs

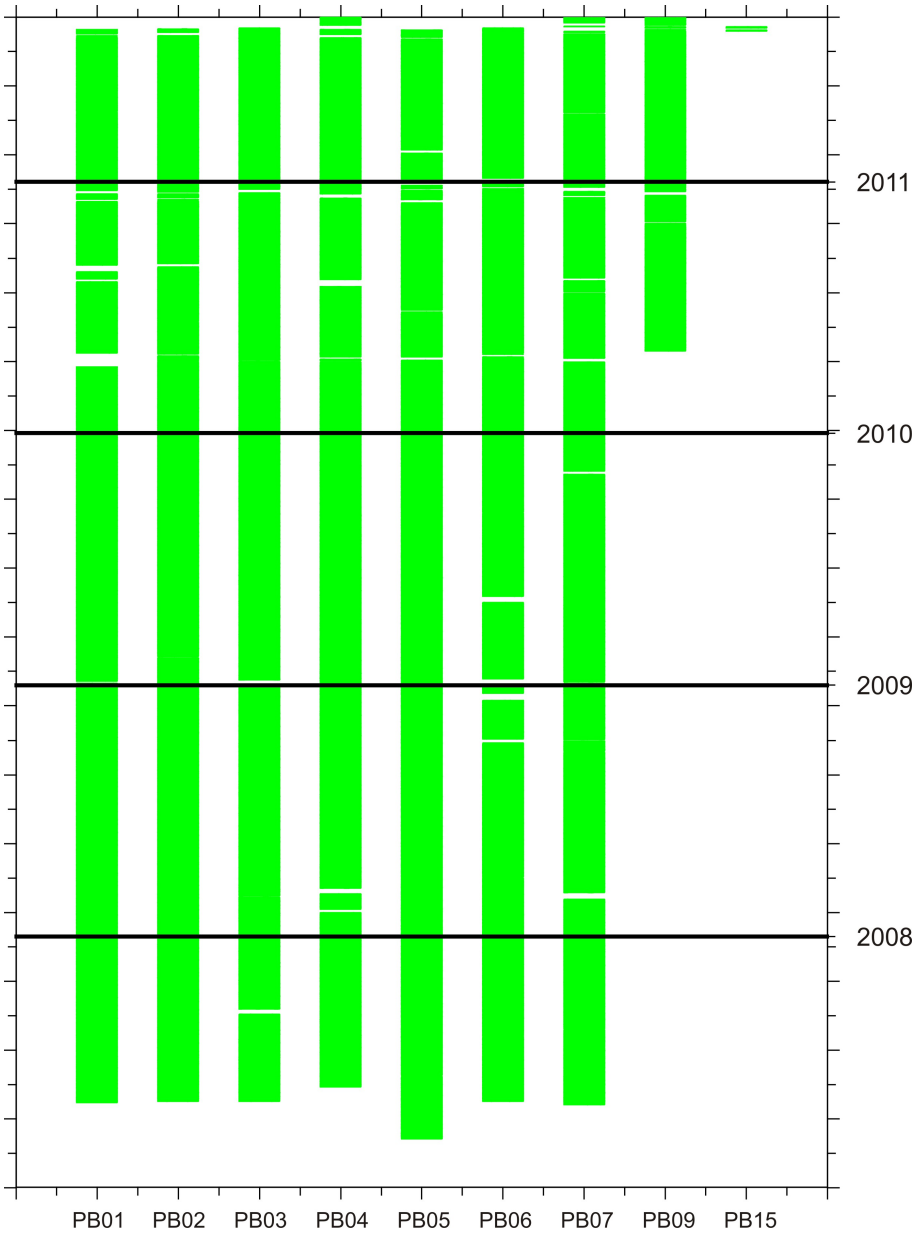

Figure 3.1: Green bars indicate existing VTF data of the various IPOC MT monitoring stations at the time of writing. Horizontal black lines indicate turn of year. At sites PB09 and PB15, MT instruments were installed in 2010 and 2011. Stable electric field data exists since the beginning of 2011.

are calculated from these spectra as explained in section 1.2. A VTF estimate for the next day is obtained by advancing the time series by one day and repeating the procedure described above. At the time of writing we have obtained VTF-time series with a total

length of more than 4 years (2007 - 2012) (Figure 3.1) for a range of periods between a few seconds and several thousand seconds for each site.

The whole procedure of computing VTFs for different sites and periods had to be automated due to the enormous amount of data: at the end of 2012 the complete database had a volume of more than 3.5 TB. I created scripts, in this case Windows Powershell, which comprehensively control execution of the individual processing steps and general data handling. The database contains all data, including intermediate results at different processing steps which can be used for a reprocessing, e.g. with different processing parameters. A folder for each site contains daily subfolders (Fig. 3.2) for raw time series, filtered time series and results like spectral information and transfer functions.

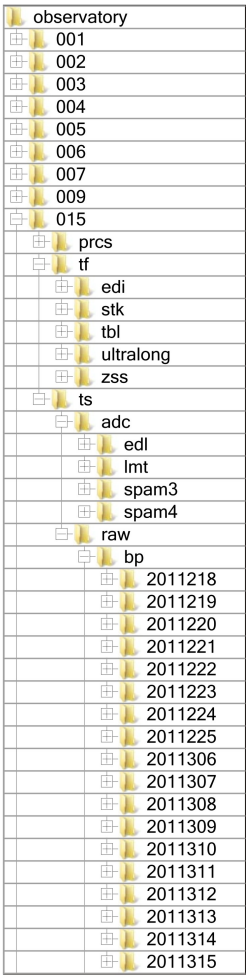

Figure 3.2: Database structure, exemplarily shown for site PB15 (015). Paths for transfer functions (tf) and EM time series of different states of processing (ts). Both paths contain folders for daily data, shown are the folders for daily bandpass filtered time series (bp).

In order to assure redundancy, there are two different ways of gathering the data. At one hand, data is read-out manually from the EDLs (section 2.2.1) when maintaining the stations, at the other hand the data is transmitted via satellite connection. In both cases, the data is available in different subformats of the 'Standard for the Exchange of Earthquake Data' (SEED) format (http://www.iris.edu/manuals /SEED_chpt1.htm). In this case MiniSEED is used which is a 'data only' format for time series which is self-sufficient without any additional information, as for example header files.

The data which is read-out directly from the EDL can immediately be used for processing because of pre-existing EMERALD tools which convert the miniseed data into the EMERALD data format as required by the processing. The EMERALD data format consists of pairs of related files, the extract file (.XTR) which is an ASCII header file containing all relevant information about the station as for example coordinates, used sensors, dipole length and amplification; and a data file (.RAW) containing the binary data streams with individual event headers.

In contrast, the satellite data is transmitted via SEEDLink protocol, a robust data transmission which prevents data loss even if the client is disconnected and reconnected during transfer. For this reason the MiniSEED files are reorganised and compressed differently as requested by the existing EMERALD tools. To automate this procedure for the large volume of transmitted data I created bash script functions under Linux which use pre-existing tools and organise the data handling.

Afterwards both kind of MiniSEED files are suitable for EMERALD processing and following processing steps are applied: first the MiniSEED data is transformed into EMERALD format. Subsequently, resampling is applied since the sampling rate is 20 Hz and the EMERALD processing accepts at the time of writing only sampling rates in a 2^n scheme. Then the time series are band-pass filtered in a cascade decimation scheme and cut into daily files which are stored in daily folders for each station (Fig. 3.2). After all data is prepared in this way, time series of requested days can easily be merged together for further processing steps, e.g. to compute spectra. The resulting spectral information and transfer functions are also stored in daily folders for each site (tf\stk in Fig. 3.2) which can then be examined. This whole process was repeatedly applied until data of more than four years were processed and archived.

3.2 Time series of vertical magnetic transfer functions

For monitoring purposes, it is desirable to amplify variations of the VTF time series. Therefore the daily values of the time series are scaled by subtraction of the median value for each frequency and component:

$$\delta T_i(\tau, d) = T_i(\tau, d) - median(T_i(\tau, d)), \tag{3.1}$$

d denotes the day, i the components x, y and τ the period length.

Processing more than 4 years of data reveals an unexpected behaviour in the δT_i time series: a pronounced seasonal variation mainly in the the real parts of the east-west component δT_y at all sites of the network. Exemplary time series of real and imaginary parts of δT_i at site PB03 for a period of 720 s are plotted in Figure 3.3. The value of δT_y varies systematically, showing maxima in winter and minima in summer of the southern hemisphere. The seasonal variation occurs in a wide period range from approximately 100 seconds up to at least 3000 seconds mainly in δT_y (Fig. 3.4). At some periods and sites the amplitude of the seasonal variation exceeds 100 % of the absolute value of T_y! This is a very unexpected effect which influences the size and location of electrical resisitvity contrasts of the subsurface in a model calculation significantly (c.f. section 4.5).

Seasonal temperature variations can be excluded as a cause for the observations since all magnetic field components would be affected equally. The sensors sampling the magnetic field components are integrated into one instrument. Additionally, much care was taken to prevent influence of temperature effects on the sensors by placing them in approximately 1 meter depth which reduces temperature variations to negligible values.

The IPOC network is located directly eastward of the coast of the Pacific Ocean, and the seasonal variation is observed in the east-west component δT_y. To test if seasonal changes of electrical resistivity of the seawater, which could be the consequence of varying seawater current systems, may cause the observed variation of δT_y, 2D forward models were computed (c.f. section 4.2) using the WINGLINK software package. The variation was simulated by two different forward calculations with unrealistically diverging values

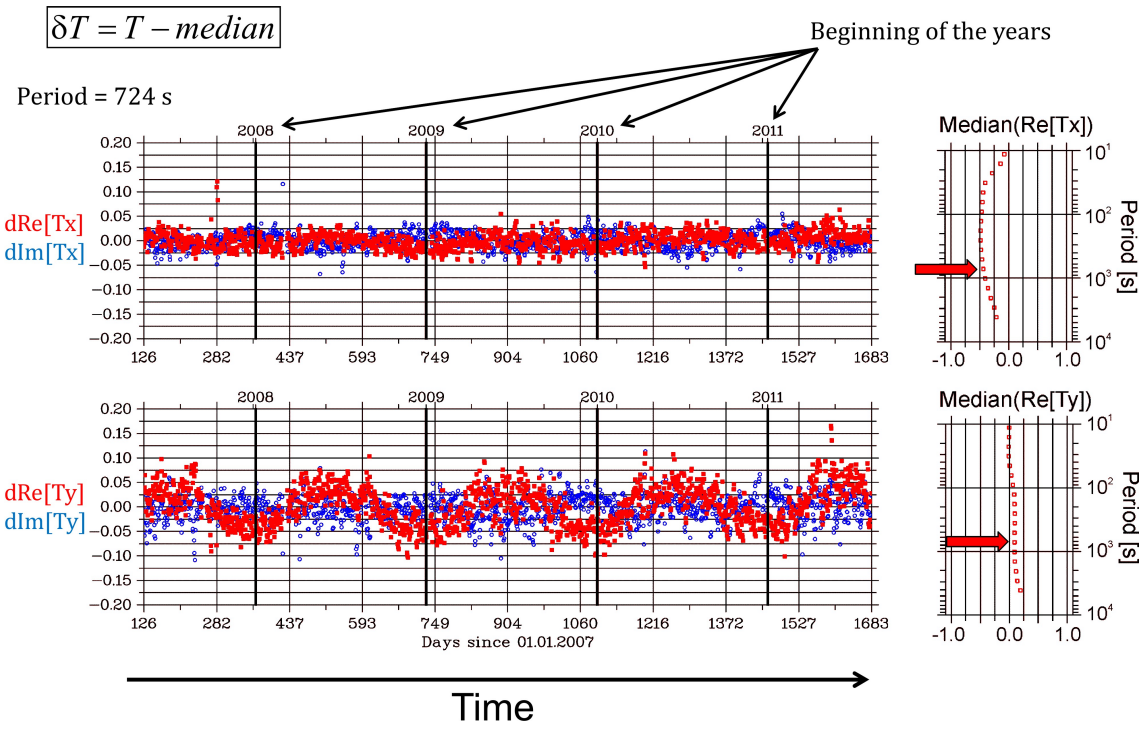

Figure 3.3: Exemplary time series of differences between daily VTFs and the according median for site PB03 for more than 4 years; each point in the panels on the left hand side represents one day. This is shown for a period of 724 seconds which corresponds to a defined induction volume (skin depth). Unexpectedly, the real part of δT_y exhibits a clear and distinct seasonal variation. The panels at the right hand side show the median values for the real parts of all periods, the corresponding value for the period 724 seconds is indicated by red arrows.

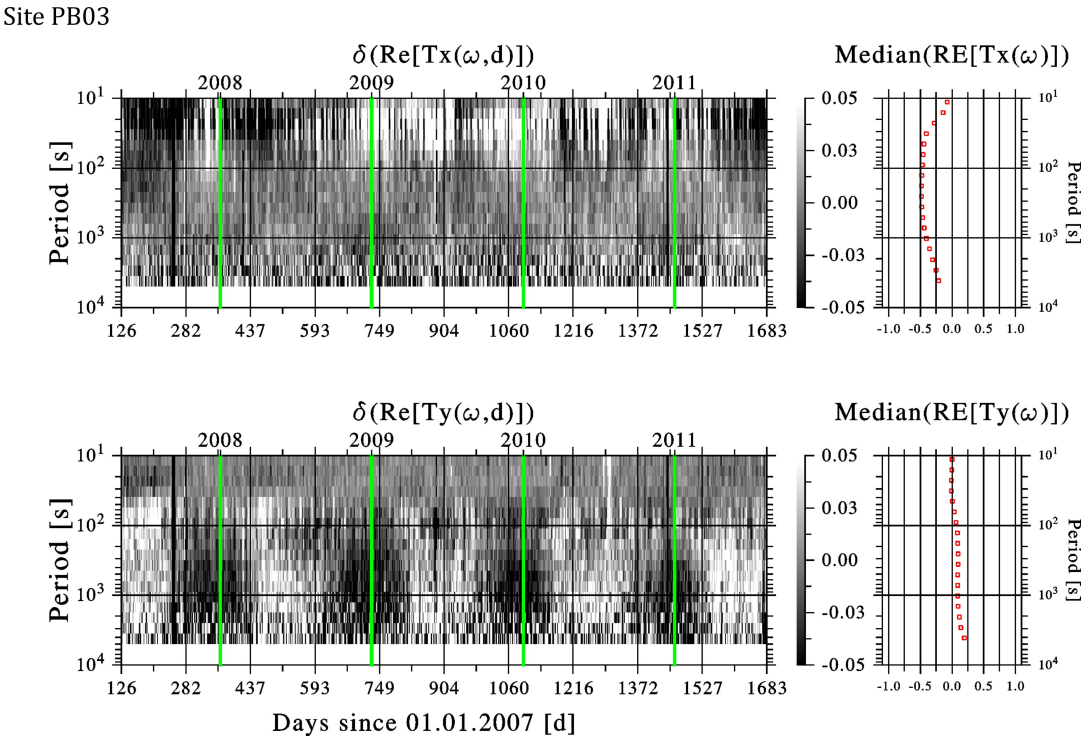

Figure 3.4: Time series of differences between daily VTFs and the according median at site PB03 for all evaluated periods. Each horizontal line represents one period. The corresponding median, which represent the zero level, is plotted at the right hand side. By observing a range of periods, we monitor several induction spaces. The seasonal variation of the real part of δT_y can be observed in a wide period range from approximately 100 s up to at least 3000 s.

for seawater resistivity of 0.2 and 0.3 Ωm (Fig. 3.5). The predicted data at a location with an identical distance to the ocean as site PB03 were calculated. Geometry including topography is fixed, setting the resistivity for the land mass to 100 Ωm. The observed effect in the measured data, which is at PB03 larger than 0.1, was not reproduced, the difference of the resulting T_y components is below 0.02 for periods 100 - 3000 s (Fig. 3.6).

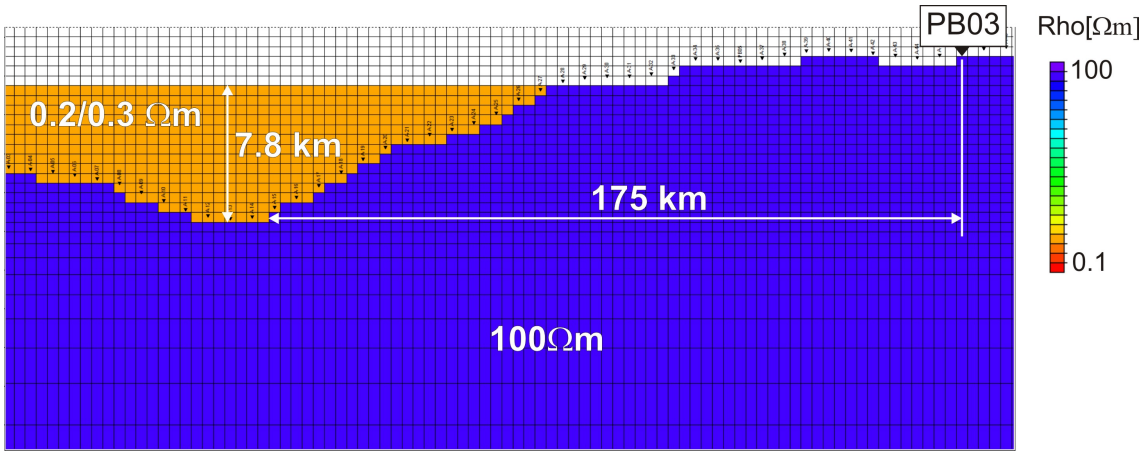

Figure 3.5: Excerpt of a 2D model of electrical resistivity mimicking the trench of the Andean subduction system and relative position of PB03.

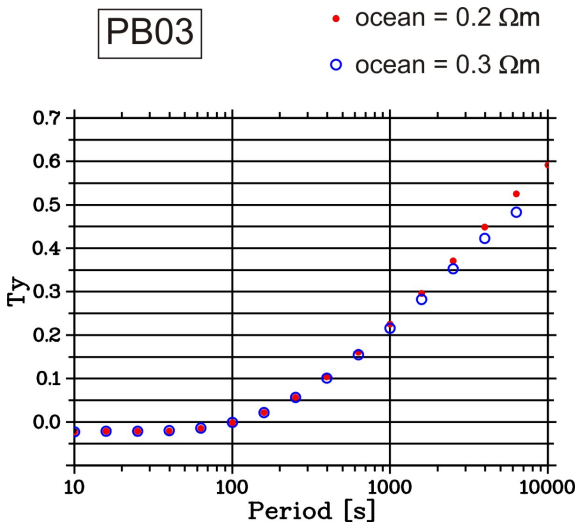

Figure 3.6: Comparison of the predicted T_y at PB03, derived by different seawater resistivities 0.2 and 0.3 Ωm (Fig. 3.5). The variation of T_y for periods 100 - 3000 s is not in the range as the observed seasonal variations in Figure 3.4. The negative values for periods $<$ 100 s are caused by topography of the Andes east of PB03.

3.3 Source field inhomogeneities and influences on MT and GDS sounding

The following sections are partly published in Brändlein et al. (2012).

3.3.1 Seasonal variation of VTFs

To quantify size and direction of the seasonal variations of VTFs, we applied a band-pass filter with a narrow pass-band around one year to the time series. This is conducted by a digital filter which is implemented by transforming the δT_i time series to the Fourier domain, multiplication of the Fourier coefficients with a suitable Parzen window (Parzen, 1962) and subsequent backward transformation into time domain.

As preparation for Fourier transformation, a few gaps in the data which originate from interruptions for maintenance of the instruments are removed by linear interpolation. In total, missing data points are less than 3 %. Furthermore, the VTF time series are smoothed with a median filter to attenuate scattering; by trial and error we chose a length of 20 data points for the running median window. As described in section 3.2, a median value of the entire time series is subtracted from each sample to emphasize variations of the VTFs. Tapering is applied to prevent sharp discontinuities at the beginning and end of a VTF time series segment. Both ends of the time segment were padded with zeros (half of the length of the original time series) to dampen oscillations. Subsequently, the VTF time series were transformed to frequency domain (Fig. 3.7).

To extract only the seasonal effect from the data we multiplied the Fourier coefficients with a modified Parzen window keeping only the period band around the annual variation. The residual spectral information was then transformed back into time domain. The band-pass filtered time series δT_y^{BP} at 720 s in Figure 3.7 (red curve) contains solely information on seasonal variations. The maxima and minima coincide approximately with winter and summer solstices of the southern hemisphere. As for the unfiltered VTFs, this is most clearly observed in the east-west component δT_y^{BP} (c.f. Figs 3.3 and 3.4). To quantify this distortion, we inspect the seasonal variations of real induction arrows more closely

To obtain the amplitude of the variation we start from the band-pass filtered daily differences δT_y^{BP} between VTFs and the median. A limited time span of approximately half a year is evaluated to cover the maximum and minimum values of the δT_y^{BP} variation (transparent green rectangle in Fig. 3.7). We search for maximum and minimum values $\delta T_y^{BPmax/min}$ in this time span. Subsequently, δT_x^{BP} from the corresponding days is picked to assure consistency. From these values the seasonal difference is calculated for the various components, sites and periods by:

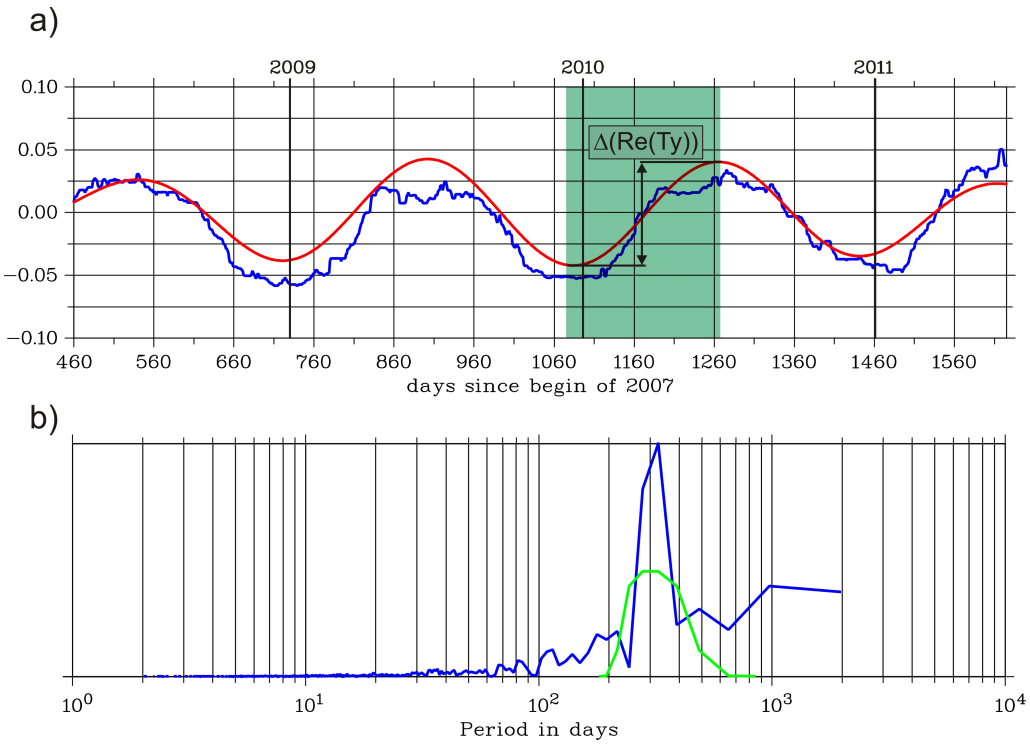

Figure 3.7: a) Smoothed time series of daily differences δT_y for site PB03 at a period of 720 s for more than 4 years (blue curve). The red curve represents the band pass filtered δT_y^{BP} time series which contains only periods of approximately one year. The considered time span for evaluation of variation amplitudes δT_y is indicated by the transparent green rectangle. b) Coefficients of the Fourier transformed time series. They are multiplied by the filter function in green which is an adapted Parzen window and subsequently inverse Fourier transformation is applied.

$$\Delta T_i(\tau) = \delta T_i^{max}(\tau) - \delta T_i^{min}(\tau) \quad , \tag{3.2}$$

i denotes the components x, y and τ the period length. From the ΔT_i we derive absolute values of variations of the induction vectors (Fig. 3.8):

$$\left|\Delta\vec{P}(\tau)\right| = \sqrt{(\Delta T_x(\tau))^2 + (\Delta T_y(\tau))^2} \quad . \tag{3.3}$$

The $\left|\Delta\vec{P}(\tau)\right|$ of all sites can be interpolated laterally over the network and plotted as colour coded contours in a plain view (Fig. 3.9). To emphasize the actual sense of motion of the induction vectors, caused by the seasonal variation, the median values of the initial T_i time series are added to the selected maximum and minimum $\delta T_i^{BPmax/min}$.

The results are used to plot summer and winter induction vectors at each site (Fig. 3.9).

At periods < 100 s the induction vectors show no significant seasonal variation. For periods > 100 s we observe a systematic east-west orientation of the variation, consistently at all sites and with increasing amplitudes for increasing period. The absolute value of the variation is roughly uniform over the network extend and increases to values > 0.1 at a period of 2000 s. In summary, the induction vectors point consistently more eastwards in southern hemisphere winter when compared to the summer position.

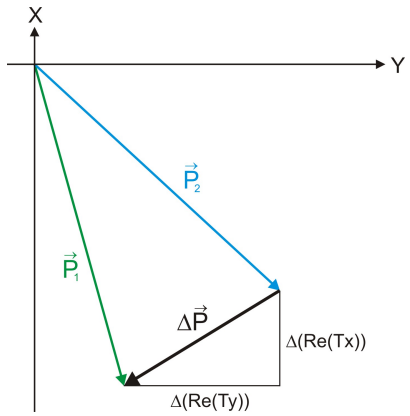

Figure 3.8: Conceptual figure to illustrate the construction of the difference vector $\Delta\vec{P}$. The blue and green induction vectors visualise hypothetical turning points of the variation.

The spatially uniform amplitude variation over the network area indicates a source field effect as cause. If not taken into account, this can lead to biased MT modelling and consequently to misinterpretation of the data. The effect of source field inhomogeneities in MT data are well known at high latitudes (e.g. Lezaeta et al., 2007) but only few occurrences have been reported from mid-latitudes. For example, measurements at two MT monitoring sites at the San Andreas Fault, California, revealed inhomogeneous source fields for periods of 10 - 30 s. Egbert et al. (2000) explained these observations as an interaction of Pc3 pulsations and strong man made EM noise caused by a DC railway system. The source field inhomogeneity found its expression as local daytime dependent variations of horizontal magnetic transfer functions. In a different study at four stations in North America, time varying vertical magnetic fields (induction vectors) were observed over a time span of 12 days for period bands of 67 - 100 seconds and 200 - 500 seconds (Anderson et al., 1976).

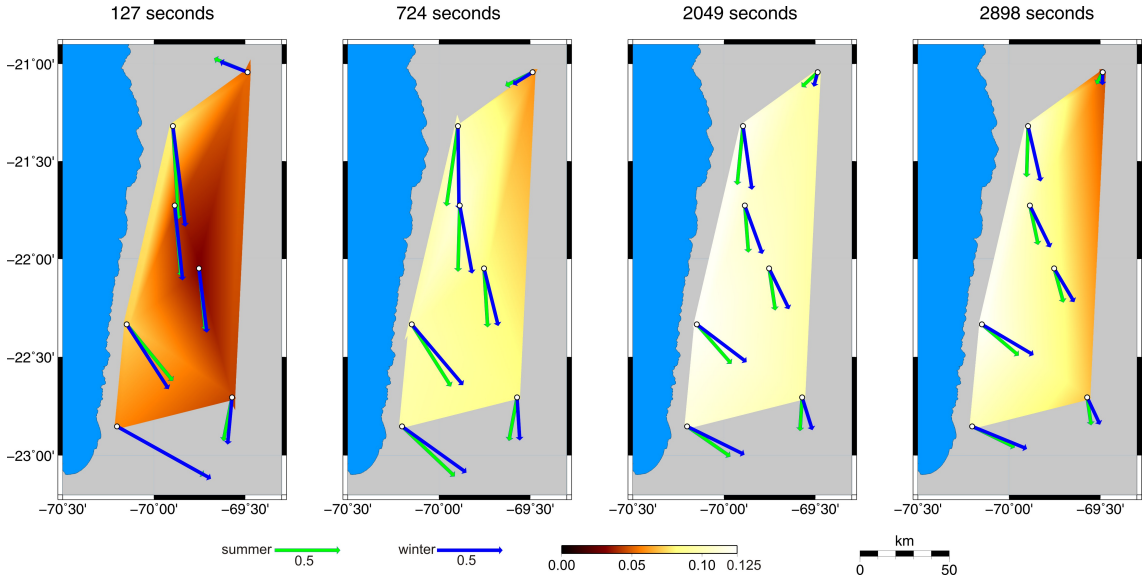

Figure 3.9: Size and direction of the seasonal variation at exemplary periods. The green induction vectors indicate the setting in southern hemisphere summer (c.f. Fig. 3.7), the blue induction arrows in winter. The underlying contour plot shows the distribution of the interpolated absolute value of the difference arrows (equations 3.2 and 3.3) over the network area. At periods < 100 s no significant variation can be observed. For increasing periods an increasing variation amplitude can be observed. The variation amplitude shows nearly uniform values over the network extend. During summer the induction arrows are smaller and deviated towards W when compared to winter.

3.3.2 Influences of ionospheric current systems

VTFs are ratios between vertical and horizontal magnetic field components (equation 1.14). To understand which particular magnetic field component is responsible for the variations described in section 3.3.1, time series of power spectral densities (PSD) are examined.

PSDs are squared absolute values of Fourier transforms B_i of magnetic field time series; i represents x, y or z direction. Since B_i is complex, the square of the absolute

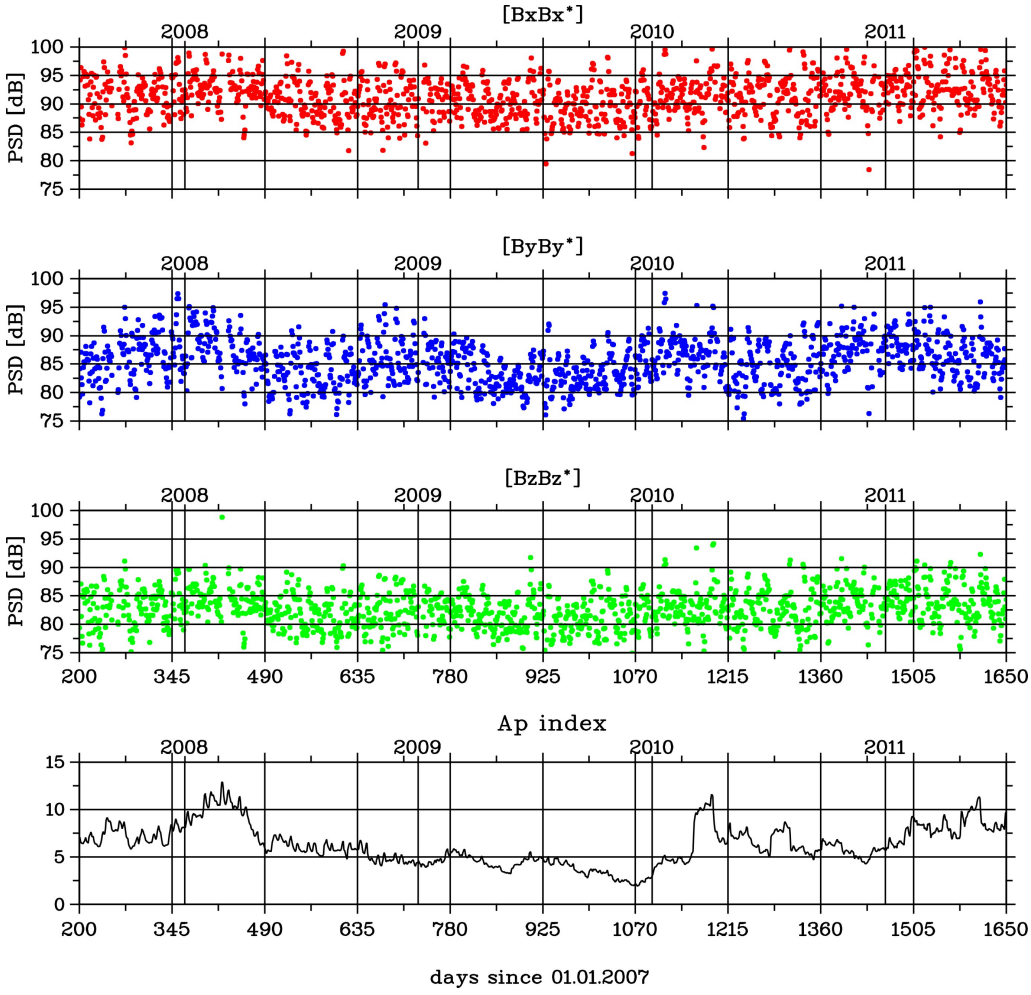

Figure 3.10: Time series of daily magnetic field auto spectra at site PB03 for a period of 2049 s. A pronounced seasonal variation is visible in the east-west component $B_y B_y^*$ (blue dots). The bottom panel shows monthly averages of the Ap index. The median of daily Ap indices during this time span is 4.0.

value is obtained by multiplication of B_i with the complex conjugate B_i^*. To calculate time series of PSDs we apply modules of the robust magnetotelluric data processing package EMERALD described in section 3.1.

An estimate for a daily PSD is obtained from a three day long data segment which is repeatedly band pass filtered in a cascade decimation scheme. The individual band pass filtered data are subdivided into shorter time windows and subsequently transformed into frequency domain. To improve statistical significance, the resulting power spectra of individual time frames are stacked in the frequency domain. A PSD estimate for the next day is obtained by advancing the time series by one day and repeating the procedure described above. Eventually, this results in a continuous stream of frequency dependent PSDs. Figure 3.10 shows PSD-time series over the whole time for site PB03 at a period of 2048 s. A pronounced seasonal periodicity is clearly visible, but predominantly in the east-west magnetic field component (labelled $[B_y B_y^*]$ in Fig. 3.10). The maximum power spectral amplitudes are observed during summer of the southern hemisphere and minimum values correspond to winter.

The seasonal variation of the PSD time series can be extracted from the data by using a narrow band pass filter centred on a period of one year as described previously for VTFs in section 3.3.1. The filtered PSD time series $\bar{P}_i$ contains solely information on seasonal variations, the maxima and minima coincide with southern hemisphere summer and winter solstices, respectively, with a delay of approximately one month. This is most clearly observed in the east-west component $\bar{P}_y$ (not shown, c.f. Fig. 3.10). To quantify the magnitude of the variations during half a year we sum up individual daily differences of the filtered PSD time series for each site, period and component. Figure 3.11 shows the resulting magnitudes interpolated laterally over all sites at exemplary periods of 90 s, 700 s and 2000 s. Sites PB09 and PB15 had to be excluded as they were installed only in 2010 and 2011, respectively.

The size and distribution of seasonal PSD variations shows a similar pattern for all considered periods. The east-west component $\bar{P}_y$ varies by approximately 4 dB quite con-

Figure 3.11 *(following page)*: Spatial distribution of seasonal variations of magnetic field PSD over the IPOC network in Northern Chile. Amplitudes are colour coded and interpolated over the network area. (left) The $B_x B_x^*$ component, (middle) the $B_y B_y^*$ component, and (right) the $B_z B_z^*$ component. Rows are for periods 90 s, 724 s and 2049 s. For periods > 100 s, the east-west component exhibits an amplitude variation of more than 4 dB, roughly consistent at all sites. The variation of the vertical and north-south components is weaker, typically below 2 dB.

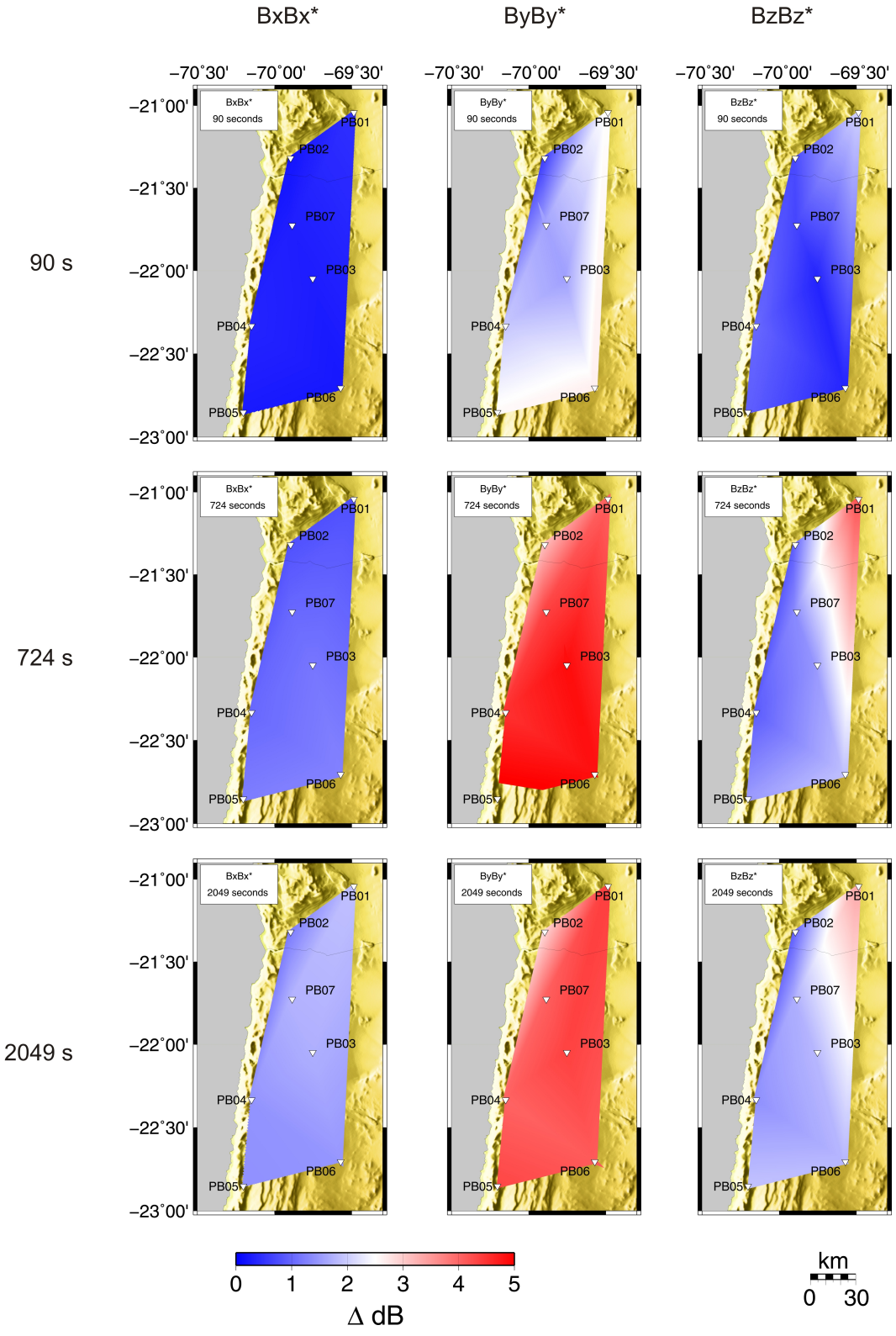
BxBx*
ByBy*
BzBz*
90 s
724 s
2049 s
−70˚30'
−70˚00'
−69˚30'
−21˚00'
−21˚30'
−22˚00'
−22˚30'
−23˚00'
BxBx* 90 seconds
ByBy* 90 seconds
BzBz* 90 seconds
BxBx* 724 seconds
ByBy* 724 seconds
BzBz* 724 seconds
BxBx* 2049 seconds
ByBy* 2049 seconds
BzBz* 2049 seconds
PB01
PB02
PB07
PB03
PB04
PB05
PB06
0 1 2 3 4 5
Δ dB
km
0 30

sistently over the entire network which means the signal power of this particular magnetic field component doubles during summer compared to winter. In comparison, the magnitudes of seasonal $\bar{P}_x$ and $\bar{P}_z$ variations are much smaller, typically below 2 dB. At site PB01 the $\bar{P}_z$ variation increases to more than 3 dB which is attributed to a local effect. For shorter periods ($<$ 100 s), the seasonal variation of $\bar{P}_y$, $\bar{P}_x$ and $\bar{P}_z$ decreases and show magnitudes below 2 dB.

To characterize the causes for seasonally variations of the PSDs in more detail, we examine the diurnal variation of activity time. For this purpose, the magnetic field data of the entire year 2009 is divided into 12-hour time segments. We chose a length of 12 hours to ensure the statistical significance of the PSDs at periods of up to several thousand seconds and to allow characterization of the magnetic field at varying daytime segments. Data from opposite diurnal time segments (e.g. daily segments of 06:00-18:00 and the opposite diurnal segments from 18:00 - 06:00) are processed separately using the processing steps described in section 3.1. By testing all different diurnal time segments we can identify times which show the largest contrast in seasonal variation. Time segments where at least 12 hours long to avoid scattering at longer periods. To emphasize variations of the PSD time series, the absolute values are scaled by subtracting the median.

Figure 3.12 shows a maximum seasonal variation of more than 5 dB in the $B_y B_y^*$ component for time segments recorded between 08:00-20:00 local time (LT). Variations of the other magnetic field components hardly exceed 2 dB. The opposite diurnal time segments from 20:00-08:00 LT caused also only variations of approximately 2 dB. Seasonal variations average out when processing time segments from 00:00-12:00 and 12:00-24:00 LT, respectively (not shown). In summary, seasonal variations of the east-west magnetic field PSDs appear to maximize in a time window centred on local noon between 08:00 and 16:00 LT.

Time dependency of the spectral relation between electric and magnetic Fields

In order to identify a time dependency of ratios between horizontal electric and magnetic field spectra we use transfer functions Z_{xy} and Z_{yx} to compare data from different daytime segments and different seasons. These transfer functions represent the off-diagonal elements of the magnetotelluric impedance tensor (section 1.2). The impedances are used to estimate apparent resistivities which are a period dependent quantity. Consequently, apparent resistivity can be seen as an average resistivity value of a hemisphere with radius δ (electromagnetic skin depth, see section 1.2) and increasing periods reflect larger volumes

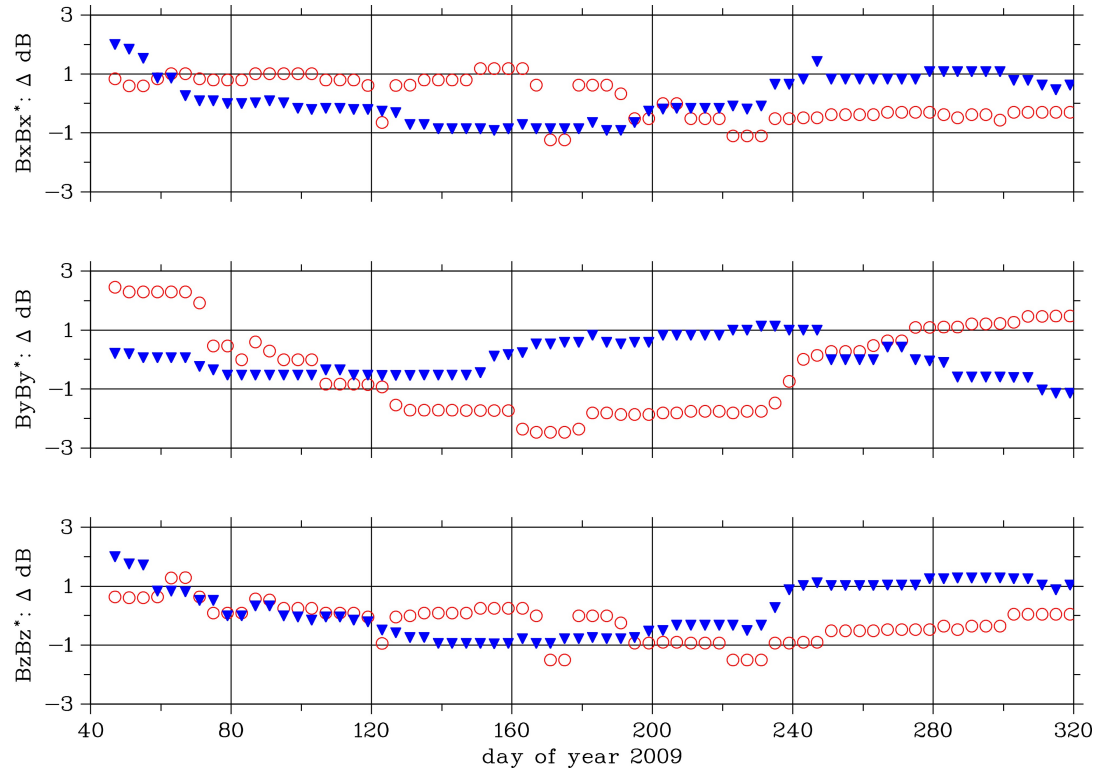

Figure 3.12: Dependency of PSD time series on local time, shown for site PB02 at a period of 1447 s for 2009. The red curve indicates PSDs of time segments recorded between 08:00 and 20:00 LT. The blue triangles represent PSDs of time segments between 20:00 and 08:00 LT. The maximum variation of approximately 5 dB is observed for the daytime data of the east-west component (red curve).

of Earth's subsurface. The periods considered here roughly reflect sounding depths in the range of a few kilometres and several tens of kilometres. Normally, the electrical resistivity structure in these depths is expected to remain constant on time scales of several years. To test the validity of this assumption we calculate impedance tensor transfer functions for a range of times, e.g., different local times or seasons. Differences are calculated as:

$$\Delta Z^{12} = \frac{|Z^1| - |Z^2|}{|Z^1| + |Z^2|} \quad . \tag{3.4}$$

The superscripts indicate that the transfer functions Z characterize the ratios between electric and magnetic field spectra at different time sectors. Since the spectra are complex, Z is also complex and we use absolute values for evaluation. For the computation of each individual transfer function Z we use data from equal 8 h time segments of 30 consecutive days. We chose 8 h because this time interval enables us to evaluate eventual variations

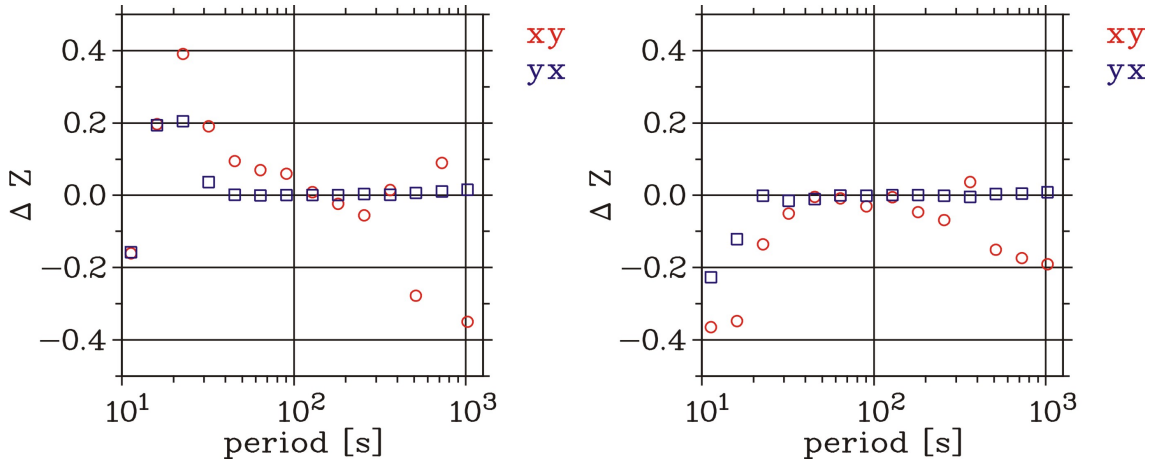

Figure 3.13: (left) Normalized differences between daytime (08:00-16:00 Chile local time) and nighttime (20:00-04:00 Chile local time) transfer functions from 30 days starting with 10 January 2011 between electric and magnetic field spectra. (right) Differences between daytime (08:00-16:00 Chile local time) data in summer (30 days starting with 10 January 2011) and winter (30 days starting with 20 June 2011). Clearly, the xy component of the impedance tensor shows temporal variations. The average Ap index level of the considered days in summer is 6.4, in winter 8.0.

of Z during 24 h. The use of daily time windows of 8 h allows reliable evaluation of Z up to maximum period lengths of approximately 1000 seconds.

We compare day (Z^1, 08:00 - 16:00 Chile local time) and night (Z^2, 20:00 - 04:00 Chile local time) from 30 days of southern hemisphere summer starting with 10 January 2011. The resulting differences show only for Z_{xy} a clear time dependency with negative ΔZ_{xy} at periods from 100 to 1000 seconds (Fig. 3.13, left panel). This is consistent with higher magnitudes of east-west magnetic field PSD during day compared to night as found for summer (Fig. 3.12). For calculating Z_{xy} we divide by magnetic field spectra, and consequently Z_{xy} becomes smaller during daytime when compared to nighttime; thus ΔZ_{xy} becomes negative.

When comparing 8 h daytime segments (08:00 - 16:00 Chile local time) of summer (Z^1, 30 days starting with 10 January 2011) with those from winter (Z^2, 30 days starting with 20 June 2011), we obtain a similar result for periods > 100 s (Fig. 3.13, right panel). ΔZ_{xy} is negative at periods between 100 and 1000 seconds, while ΔZ_{yx} is nearly zero over the entire period range for day and night, summer and winter.

In summary, the ratio between east-west electric and north-south magnetic field (Z_{yx}) remains constant, as expected, during day and night and summer and winter for periods

from 20 to 1000 seconds. In contrast, the ratio between north-south electric field and east-west magnetic field, and thus Z_{xy}, varies with daytime and season.

To recapitulate these results: PSD time series of horizontal and vertical magnetic fields recorded at 7 monitoring stations in Northern Chile exhibit a pronounced temporal variation of the east-west component with an amplitude of about 5 dB for periods between 100 and several thousand seconds. This pronounced variation of B_y is observed between solstice seasons and day- and nighttime. Seasonal variations are also observed for the north-south and vertical magnetic components but with three orders of magnitude smaller power. For the calculation of the seasonal PSD time series, continuous magnetic field time series of 3 subsequent days are used, and hence, the PSDs represent an average over day and nighttimes and varying geomagnetic activity levels. The ratio between north-south magnetic field and east-west electric field is constant throughout the seasons and also for day and night. In contrast, the ratio between east-west magnetic field and north-south electric field varies with daytime and season. As the amplitudes of the PSDs seasonal variations are approximately uniform over the area of the IPOC network, we can exclude an influence of seasonal varying electrical properties of the nearby Pacific Ocean as cause. Such an influence should affect the magnetic fields at sites near the coast more than sites further inland. Using segments of a day for the computation of PSDs shows that the seasonal variation of $B_y B_y^*$ originates primarily from the time sector 08:00 to 16:00 LT.

Interplanetary electric field data

We suggest that local time and seasonal dependence of $B_y B_y^*$ is caused by interaction of solar wind and the ionosphere. The penetration of the solar wind into the ionosphere can be characterized in different ways. Manoj et al. (2008) reported a best correlation between interplanetary electromagnetic fields and equatorial ionospheric data when comparing the interplanetary electric field component IEY.

To verify an influence of penetrating interplanetary electric fields on ground-based electromagnetic field observations at the IPOC stations, we used solar wind data from the Advanced Composition Explorer (ACE) satellite (Fig. 3.14). This satellite orbits the L1 libration point in the interplanetary space, and 1 min data are provided by NASA/GSFCs through OMNIWeb (http://omniweb.gsfc.nasa.gov/). The ACE data are time shifted to the bow shock nose of Earth's magnetosphere. IEY can be calculated from the ACE magnetic field and solar wind velocity as

$$IEY = v_{sw} \times B_z \quad , \tag{3.5}$$

x, y and z directions correspond to the Geocentric Solar Magnetospheric (GSM) coor-

dinate system. In GSM coordinates, the x axis is directed from Earth to sun, the y axis is perpendicular to Earths magnetic dipole pointing toward evening section (eastward) and the z component points northward, completing the triad. **E** denotes the interplanetary electric field, **B** the interplanetary magnetic field and v_{sw} the solar wind velocity in negative x direction.

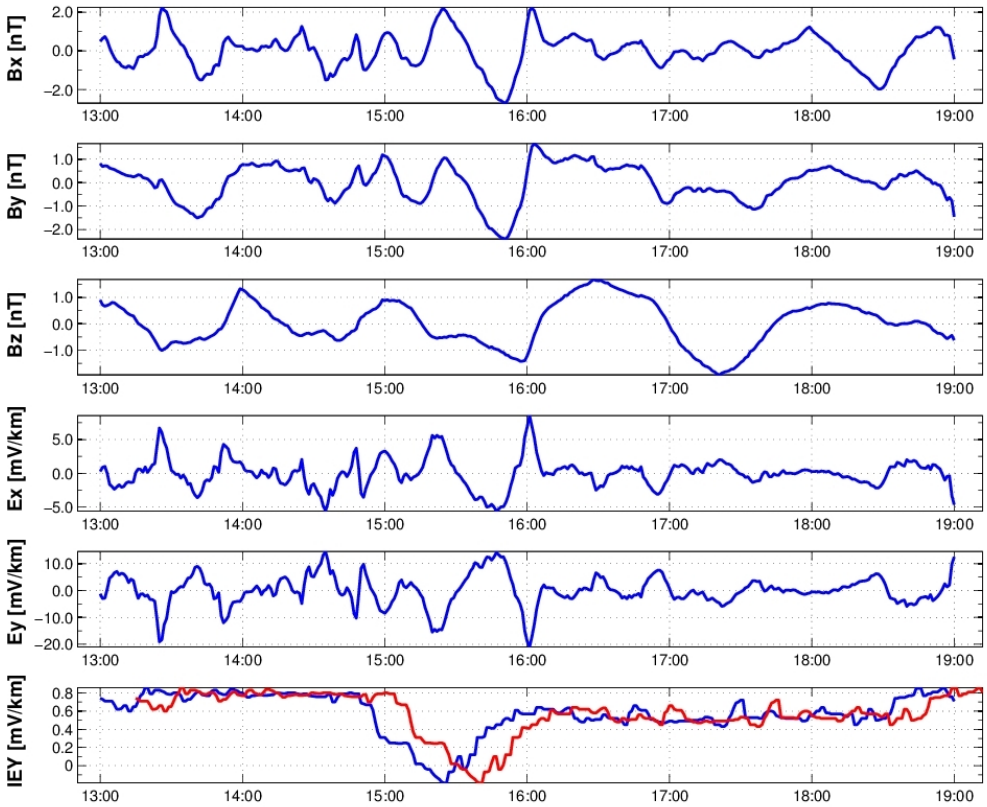

Figure 3.14: Exemplary synchronous 6 h time windows (30 January 2011, 09:00 - 15:00 Chile local time) of electromagnetic field data from site PB05 and interplanetary electric field data at the L1 libration point from ACE satellite. (top to bottom) Three magnetic field and two electric field components of site PB05. The blue curve in the lowermost panel shows IEY time series propagated to the bow shock; the red curve is time shifted by 15 min which is the signal delay time between the bow shock nose of Earth's magnetosphere and the IPOC stations at Earth's surface in Northern Chile.

Signal coherency between IEY and ground stations

For comparison, our IPOC time series are resampled to 1 min sampling, analogous to the ACE data (Fig. 3.14); missing data points are linearly interpolated. Then, we can calculate magnitude squared coherences $C_{IPOC-IEY}$ between the IEY and the various IPOC components. $C_{IPOC-IEY}$ is the ratio of the magnitude squared cross power spectral density of the IEF and respective IPOC components ($P_{IPOC-IEY}$), and the product of the power spectral densities of both signals (P_{IEY} and P_{IPOC}):

$$C_{IPOC-IEY}(\tau) = \frac{|P_{IPOC-IEY}(\tau)|^2}{P_{IEY}(\tau)P_{IPOC}(\tau)} \quad . \tag{3.6}$$

τ is the period length in seconds. The magnitude squared coherence is a measure for the linear dependency of both signals. Values are normalized, ranging between 0 and 1, independent of signal amplitudes. The cross power spectral density is the Fourier transformed cross correlation function, the power spectral density is the Fourier transformed auto correlation function. To compute power spectral densities we use a Hamming window of 4 h length.

In Figure 3.15, magnitude squared coherences are shown for time segments from 10:00 to 14:00 LT of 30 subsequent days. This daytime window shows the highest coherence values; it was found by trial and error. Averaging over 30 days is a compromise between achieving some statistical significance and resolving seasonal variations. Particularly, we are interested to compare southern hemisphere summer and winter time coherences. For southern hemisphere summer time, we used 30 days of data starting from 10 January 2011, and for winter time, 30 days starting from 20 June 2011. The significance levels of the computed coherences are 0.1 with 95% confidence intervals following Thompson (1979). Coherences are computed for periods between 1000 and 10000 s, but above 5000 s resolution decreases.

Figure 3.15 shows coherences for southern hemisphere summer between IEY and ground-based data exemplary for sites PB05 and PB09. Two peaks with values of 0.2 to 0.35 appear at periods of approximately 1800 s and 2700 s (30 min and 45 min). The B_y components of the IPOC stations exhibit the highest coherences with the IEY.

For southern hemisphere winter time, high coherences at 30 min and 45 min are also visible but they appear more concentrated on narrow period bands (Figure 3.16). In addition, enhanced coherences appear for periods of approximately 90 min (5400 s) and 22.5 min (1350 s) with values ranging between 0.2 and 0.4. These 4 periods could reflect a fundamental mode of 90 min and three harmonics.

Coherences between IEY and the IPOC electric fields show a similar behaviour as the magnetic fields, but with lower values. These relatively low coherences between IEY and

electric fields can be attributed to local effects which are mainly observed in the electric fields. Nighttime (22:00 to 02:00 local time) southern hemisphere summer data reveals coherences mostly below 0.2 (Figure 3.17).

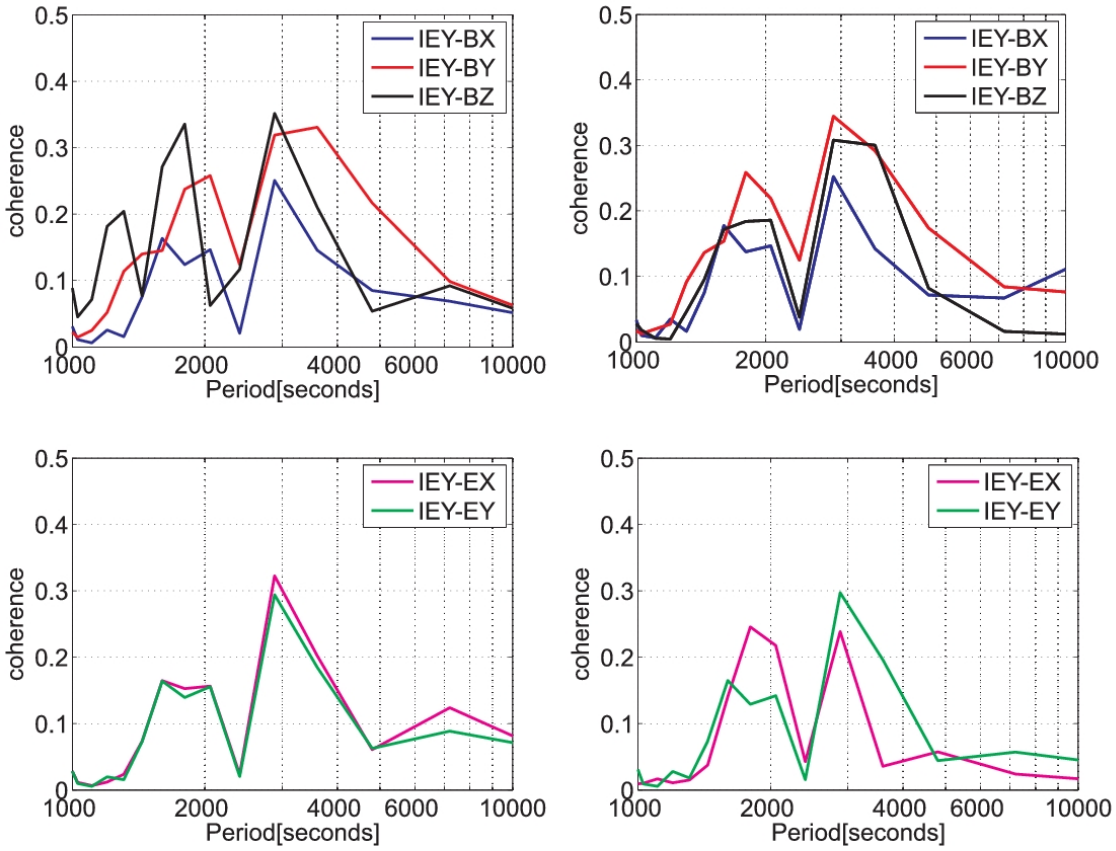

Figure 3.15: Summertime coherences between IEY and (bottom) electric and (top) magnetic field components of the IPOC sites (left) PB05 and (right) PB09. We used data from the daytime segment between 10:00 and 14:00 local time from 30 consecutive days starting with 10 January 2011. The coherences peak at periods of approximately 1800 s (30 min) and 2700 s (45 min). The average Ap index level during the considered period is 6.4.

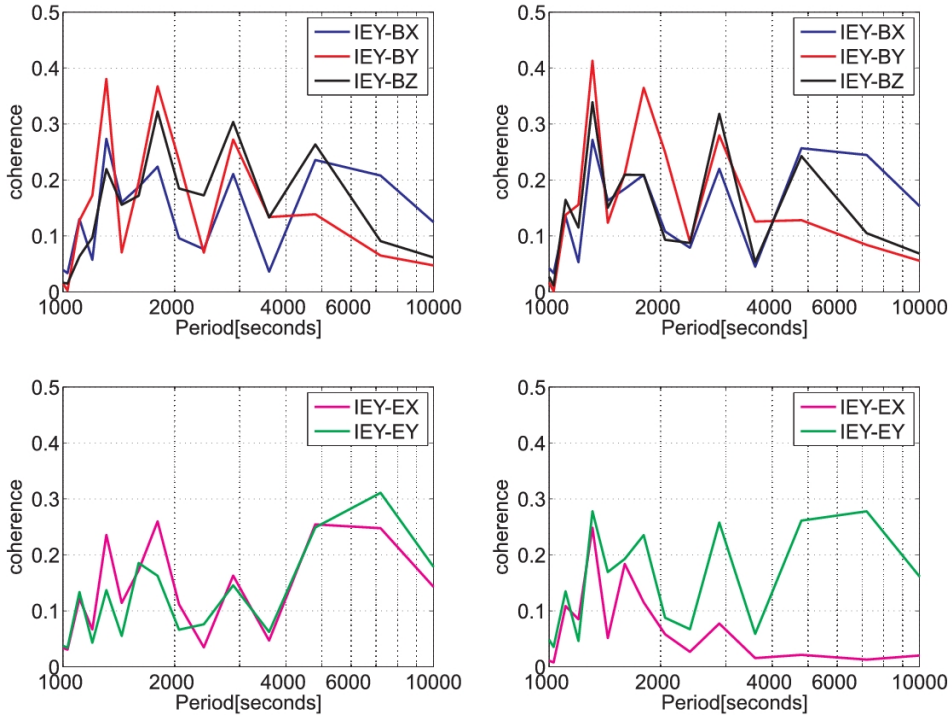

Figure 3.16: Wintertime coherences between IEY and the (bottom) electric and (top) magnetic field components of IPOC sites (left) PB05 and (right) PB09. Data are taken from 4 h (10:0014:00 local time) daytime intervals of 30 consecutive days starting with 20 June 2011. The average Ap index level during the considered period is 8.0.

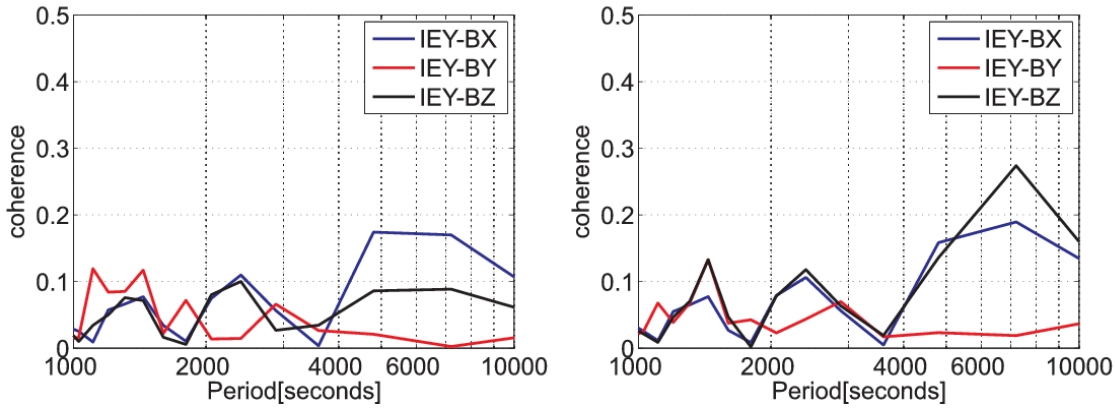

Figure 3.17: Coherences between IEY and magnetic field components of sites (left) PB05 and (right) PB09 computed for 30 nighttime segments (22:0002:00 local time) starting with 10 January 2011. The average Ap index level during the considered days in summer is 6.4, in winter 8.0.

Signal time delay between the bow shock nose and the IPOC stations

Cross correlation sequences are used to compute the time delay between electromagnetic signals from the bow shock nose of Earths magnetosphere and the IPOC stations at Earths surface in Northern Chile. The interplanetary electromagnetic field at the bow shock nose is represented by the IEY component and we chose site PB05 for comparison, since this site showed highest coherences with the IEY. The prompt penetration effect of the IEY, which we are trying to identify, is one of a multitude of geomagnetic variations which are all superimposed. Therefore, it is necessary to carefully select suitable time windows with clearly observable IEY signals for a cross correlation. We found a window length of 90 min as appropriate to compute the normalized cross correlation $\rho_{IEY-IPOC}$:

$$\rho_{IEY-IPOC} = \frac{Cov(IEY\ IPOC)}{\sqrt{var(IEY)}\sqrt{var(IPOC)}} \tag{3.7}$$

The numerator contains the covariance of both time series; the denominator consists of the product of the standard deviations. Figure 3.18 reveals a time delay of approximately

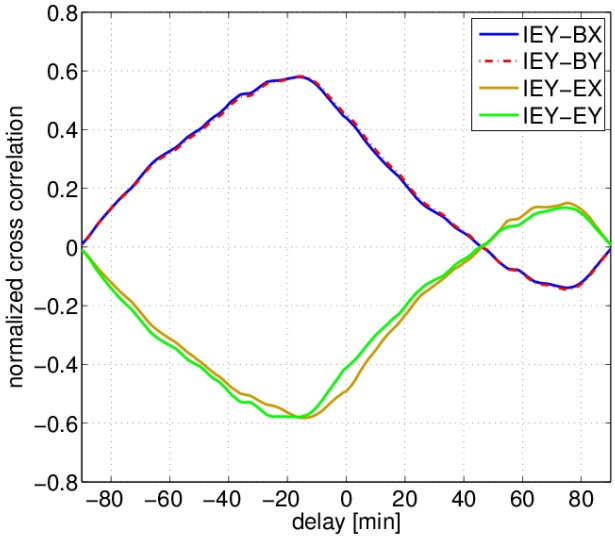

Figure 3.18: Cross correlation sequences between IEY and horizontal magnetic and electric field components at site PB05. A maximum correlation appears at a time delay of approximately 15 min. Positive correlation coefficients indicate that ground-based B_x and B_y vary in phase with IEY, the negative correlation coefficients indicate an antiphase variation of E_x and E_y with IEY.

15 min between IEF and IPOC signals by averaging cross correlation coefficients of selected time segments. We found several episodes of such 1 h time windows of southern hemisphere summer data confirming a delay time of 15 min between the bow shock nose and the IPOC stations.

Transfer functions between IEY and ground stations

The interplanetary electromagnetic fields penetrate to low geomagnetic latitudes via Earths magnetosphere and ionosphere. This process can be regarded as a linear system, with the interplanetary electric field as input and the ground based electric and magnetic fields as output. The relation between input and output channels can be described by transfer functions (TF). We compute TF as the ratio between cross power spectral density of the two considered signals ($P_{IEY-IPOC}$) and the power spectral density of the input (P_{IEY}):

$$TF_{IEY-IPOC}(\tau) = \frac{P_{IEY-IPOC}(\tau)}{P_{IEY}(\tau)} \tag{3.8}$$

We compensate the time lag of 15 min between input and output signals by shifting the IPOC data in time. The ground-based electric field data are scaled to the same units as the interplanetary electric field (mV/m). The magnitudes of the resulting non-dimensional TFs are plotted on logarithmic scales, using 20*log($TF_{IEY-IPOC}$): a ratio of 0.1 corresponds to -20 dB, 0.01 to -40 dB, etc. The TFs between IEY and IPOC magnetic field components provide relative information on the coupling mechanism. For computation of the power spectral densities we use 8 h time windows centred around local noon (c.f. Fig. 3.12) from 30 subsequent days of southern hemisphere summer (starting at 10 January 2011) and winter time (starting at 20 June 2011). We use PB05 and PB09 as the ground-based observation sites since they exhibit high coherences with the IEY. In the following, the TFs are labelled as TF_{IEY-BY} where the second term of the subscript denotes the used IPOC electromagnetic field component.

During summer and daytime, TFs between IEY and all electromagnetic field components at both IPOC sites show maximum values at periods of approximately 90, 45 and 30 min (Fig. 3.19). At these periods, we also observe high coherences between IEY and ground-based electric and magnetic fields (c.f. Fig. 3.15). Comparison between IEY and IPOC electric fields reveals that TF_{IEY-EY} is significantly larger than TF_{IEY-EX} at both sites. This can be attributed to stronger coupling of the interplanetary IEY with the ground-based E_y component. Horizontal magnetic field TFs between IEY and IPOC are larger than vertical magnetic field TFs for the period range 1000 to 10,000 s at both sites. The phases of all TFs are principally below -100 or above +100 degree except for

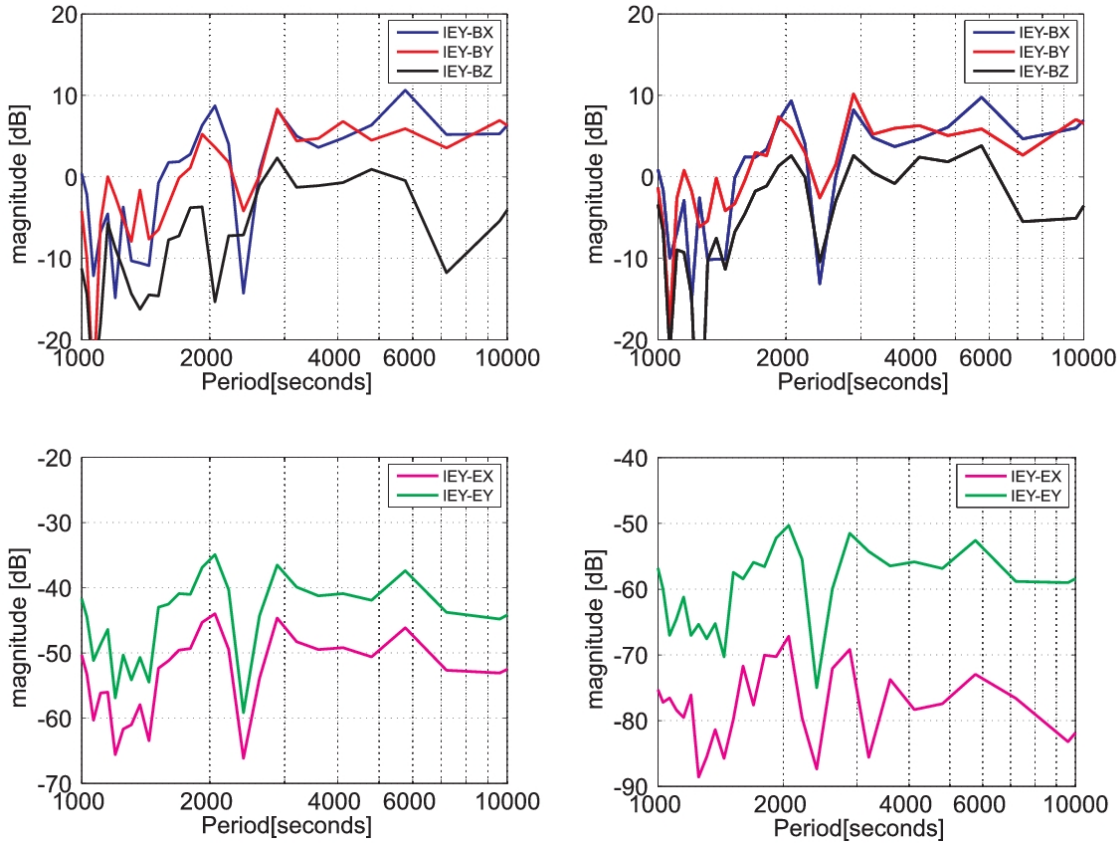

Figure 3.19: Summer time transfer functions between IEY and the electric and magnetic field components of sites (left) PB05 and (right) PB09. A time delay of 15 min is taken into account for computation (see text and Fig. 3.18). (top) Transfer functions between IEY and ground-based horizontal magnetic field components. (bottom) Transfer functions between IEY and horizontal electric field components.

TF_{IEY-EY} which exhibits phases of around 50 degree and at approximately 2000 s a phase of zero degree (not shown).

To better quantify a seasonally varying coupling between IEY and IPOC electromagnetic fields we subtract winter time TFs from summer time data. The seasonal differences between IEY and IPOC horizontal magnetic fields are very similar at sites PB05 (Figure 3.20 a) and PB09 (not shown). At both sites, the seasonal difference of TF_{IEY-BY} is more pronounced than TF_{IEY-BX}, except for a peak at approximately 30 min which also represents the maximum value. Considering TF_{IEY-BX}, a stronger seasonal difference can be observed at periods of 90, 60 and 30 min. The spectral shape of the differences is nearly identical with those of the IEY-IPOC electric field TFs.

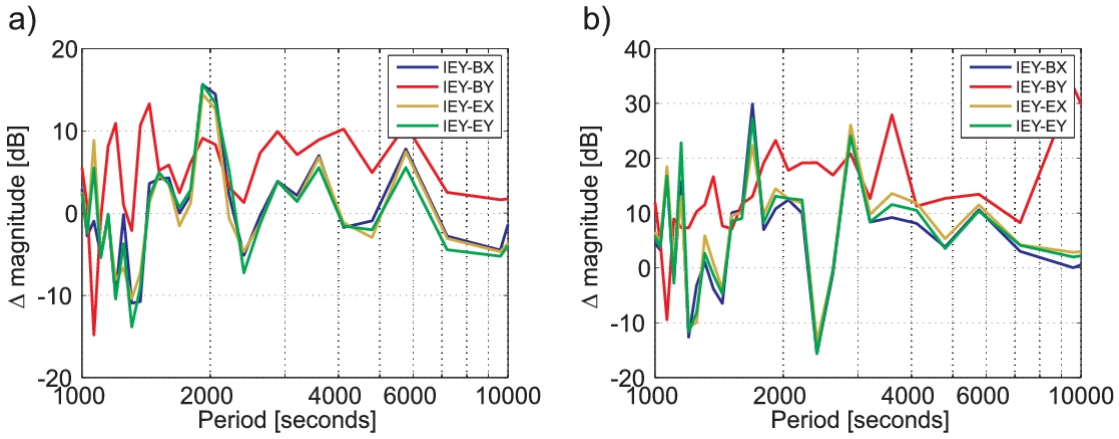

Figure 3.20: (a) Differences between summer and winter transfer functions, comparing IEY and electric and magnetic field components at site PB05. (b) Differences between daytime and nighttime transfer functions at site PB05.

The amplitude of the penetrating interplanetary electromagnetic fields is mainly controlled by the conductivity of the ionosphere (Kikuchi et al., 1996) which means the difference in TFs between day and night should be larger than the difference between summer and winter times. In order to test if the transfer functions fulfill this criterion we calculated the differences between daytime and nighttime transfer functions for site PB05. The TFs are calculated using data from 30 days and nights from southern hemisphere summer time. The resulting daytime-nighttime variations show larger amplitudes than the differences between summer and winter time (Figure 3.20 b). For TF_{IEY-EX}, TF_{IEY-EY} and TF_{IEY-BX}, the differences between daytime and nighttime transfer functions have similar values. The differences peak at periods of approximately 30 and 45 min. The daytime nighttime difference of IEY-B_y shows a main peak at 60 min; minor peaks occur at 30 and 45 min.

Discussion

PSD time series of horizontal and vertical magnetic fields recorded at 7 monitoring stations in Northern Chile exhibit a pronounced temporal variation of the east-west component with an amplitude of about 5 dB for periods between 100 and several thousand seconds. This pronounced variation of B_y is observed between solstice seasons and daytime and nighttime. Seasonal variations are also observed for the north-south and vertical magnetic components but with 3 orders of magnitude smaller power. For the calculation of the seasonal PSD time series, continuous magnetic field time series of 3 subsequent days are

used, and hence, the PSDs represent an average over daytimes and nighttimes and varying geomagnetic activity levels. The ratio between north-south magnetic field and east-west electric field is constant throughout the seasons and also for day and night. In contrast, the ratio between east-west magnetic field and north-south electric field varies with day

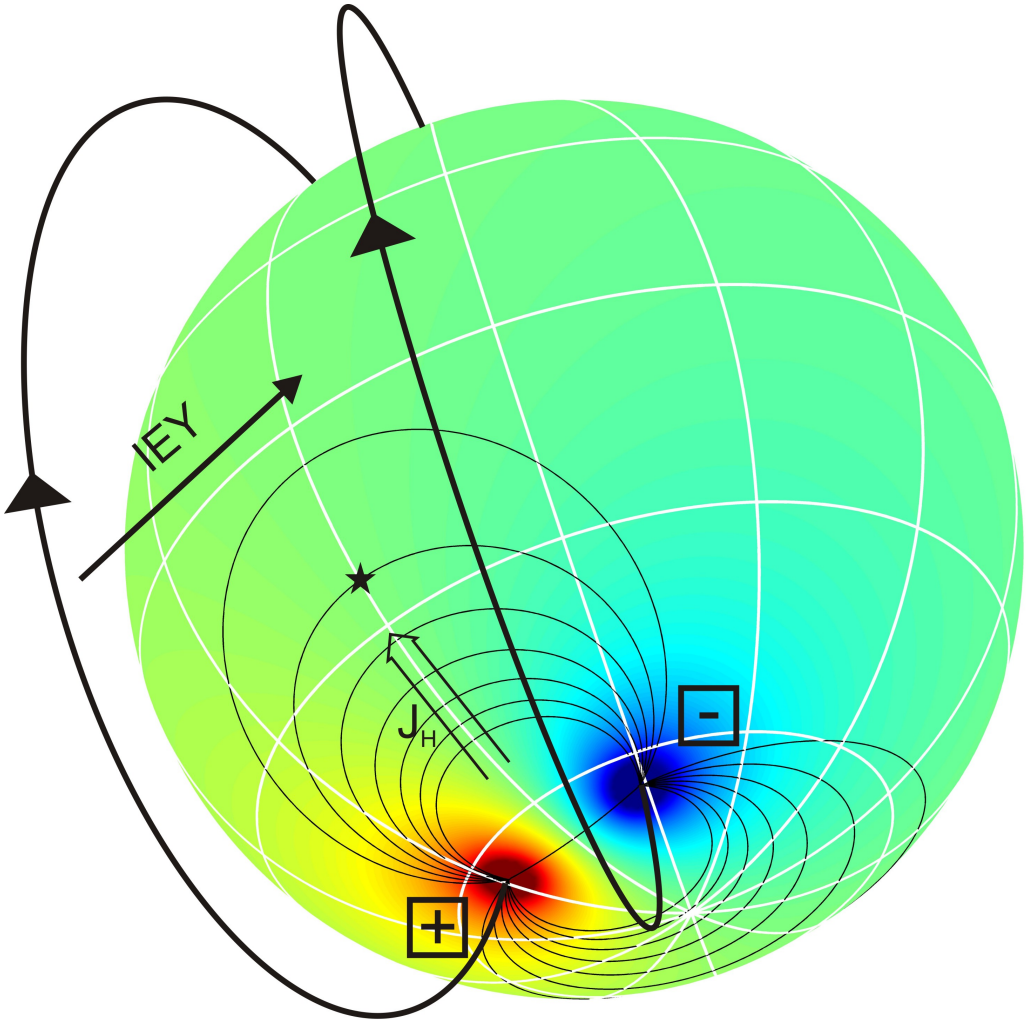

Figure 3.21: Conceptual model illustrating aspects of the ionosphere current system (following Sutcliffe & Lühr, 2010) under the assumption of homogeneous conductivity of the ionosphere. The electric potential is colour coded (arbitrary scale), black lines indicate potential field lines in the ionosphere, the Hall current is indicated by J_H. The electric field in polar latitudes is imposed by magnetospheric field aligned currents. The black star represents the location of the IPOC network at local noon relative to the source of this ionospheric current system. The white lines illustrate the geographical coordinate system.

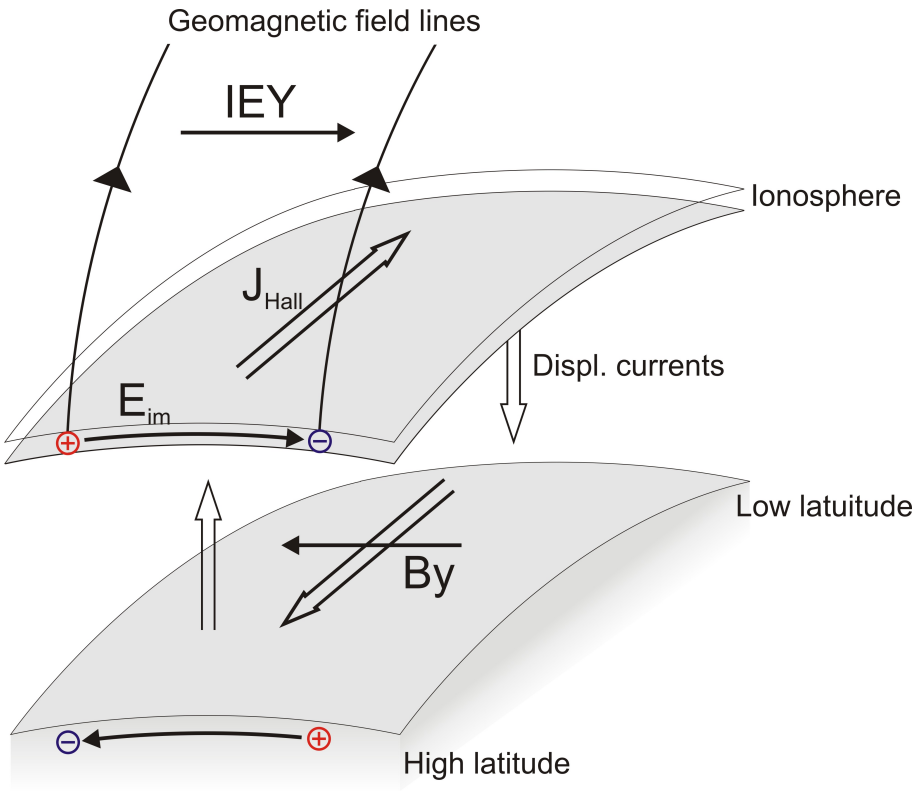

Figure 3.22: Schematic picture, following Kikuchi et al. (1978), of the electric field which is imposed in the polar ionosphere by field aligned currents. This dawn-dusk electric field in the ionosphere causes counter currents in the ground and the circuit is closed by vertical displacement currents. The propagation to the equatorial ionosphere is caused by parallel plate transmission lines (Kikuchi et al., 1996).

time and season. As the amplitudes of the PSDs seasonal variations are approximately uniform over the area of the IPOC network, we can exclude an influence of seasonal varying electrical properties of the nearby Pacific Ocean as cause. Such an influence should affect the magnetic fields at sites near the coast more than sites further inland.

Using segments of a day for the computation of PSDs shows that the seasonal variation originates primarily from the time sector 08:00 to 16:00 LT. During summer, we observe for this daytime segment significant coherences between the interplanetary electric field IEY and ground based electric and magnetic fields at periods of approximately 30 and 45 min. The statistical significance of this result is confirmed by analysis of 30 consecutive days during southern hemisphere summer. To our knowledge, it is the first time that significant coherences between satellite-based IEY and ground-based geo-electric field measurements could be established. For the analysis we used data from quiet days

with Ap < 20. Manoj et al. (2008) reported similar coherences at identical signal periods between IEY and equatorial ionospheric eastward electric fields derived from radar (JULIA) measurements when using data from 45 days (with Ap > 20). Those authors found a maximum coherence of 0.7 in a wide period range centred at 2 h which was interpreted as an indication of prompt penetration of the interplanetary electric fields to the equatorial ionosphere. Manoj et al. (2008) observed also a peak at a period of 30 min, but only for days with high magnetic activity (Ap > 20). However, the results of Manoj et al. (2008) refined prior observations by Earle & Kelley (1987), who suggested a frequency dependence of the electric field prompt penetration by comparing high- and low-latitude radar-based electric field measurements. The latter authors reported a highest efficiency for the prompt penetration at periods of 3 to 5 h.

Here, we can establish coherence values of 0.25 to 0.4 between ground and satellite based electric and magnetic field components at periods of approximately 90, 45, 30 and 22.5 min for 30 subsequent low-activity winter days. These periods reflect a fundamental mode of 90 min and up to four harmonics of the electric field penetration during local winter at the point of observation. Coherence values below 0.2 are observed for nighttime IPOC data. The difference between coherences of summer and winter times can be explained by the larger amplitude of other geomagnetic pulsations during summer which are present in addition to the prompt penetration effect.

TFs between IEY and ground-based electric and magnetic field components from two representative IPOC stations describe the directional dependency of the prompt penetration effect. Daytime data from 30 consecutive summer days consistently show a coupling between ground based electric and magnetic fields with the IEY. Maximum TFs at periods of approximately 30, 45 and 90 min correspond to periods where coherences between IEY and IPOC electric and magnetic fields are significant.

The transfer functions have in principle the same magnitude for the two horizontal B field components (see Fig. 3.19) with two exceptions. TF_{IEY-BX} is larger than TF_{IEY-BY} at periods of approximately 30 and 90 min, which can be explained by the geometry of the potential distribution of high-latitude electric fields at mid latitudes and low latitudes in the atmospheric waveguide (Sutcliffe & Lühr, 2010).

A conceptual model of the global electric field distribution in the ionosphere is shown in Figure 3.21. Field-aligned currents along the geomagnetic field lines impose an east-west aligned electric field in the ionosphere at high latitudes. This electric field evokes Hall and Pedersen currents in the ionosphere which generate magnetic fields and induce currents in the ground according to the model of Kikuchi et al. (1978). We refer to this model in the following. At high- and mid-latitudes the Hall current is directed north-south and causes east-west magnetic fields in the atmospheric wave guide. Vertical displacement

currents between Earth's surface and lowermost ionosphere are closing this toroidal current circuit (see Figure 3.22). In contrast, at equatorial latitudes the highly conductive Cowling channel controls the orientation of the effect between ionosphere and surface of the Earth by the eastward directed equatorial electrojet.

Comparison of TF_{IEY-EX} and TF_{IEY-EY} reveals much stronger coupling (by orders of magnitude) of the ground based east-west electric field components then the north-south components with the IEY. While the spectral shapes of TF_{IEY-EX} and TF_{IEY-EY} are very similar, they have different magnitudes. The shift reflects a good alignment of the penetration E field with the ground-based E_y component at local noon (see Fig. 3.21); the ground-based E_x component is almost orthogonal to the IEY component at local noon.

The ionospheric electric field caused by IEY drives Pedersen currents which flow in east-west direction around noon. Their effect can be sensed by the ground-based B_x component. It is interesting to note that the transfer function of B_x exhibits the same spectral shape as the two E field components (see Fig. 3.19). Even more exciting is the fact that the difference between summer and winter and daytime and nighttime transfer functions of B_x and the E fields show virtually the same curves (see Fig. 3.20). This means the IEY effect on these three components is coupled to the ground through Pedersen currents in the same way during both time sectors and all seasons.

Perpendicular to the Pedersen currents, Hall currents are flowing here predominantly in north-south direction (see Fig. 3.22). Their effect is sensed by the B_y component. The transfer function between IEY and B_y shows some similarities with the spectra of the other components during summer season (see Fig. 3.19) but also differences in details. Rather unexpected is the totally different spectral shape and higher amplitude level of the differences between seasons or local time sectors (Figs 3.20a and 3.20b). At least two conclusions can be drawn:

1. The height-integrated Hall conductivity varies strongly with season and local time (e.g. Du & Stening, 1999) which directly influences the signal in the waveguide. Therefore B_y shows larger differences.

2. More importantly, there is no electric field variation observed on ground responding to the IEY related Hall currents.

For the explanation of these observations we follow the concept of Kikuchi et al. (1978) assuming a wave in the space between ionosphere and ground. As shown in the conceptual model (Fig. 3.21) the interplanetary electric field is coupled via field-aligned currents into the high-latitude ionosphere. The resulting potential distribution sets up a global electric field that drives primarily Pedersen currents. Magnetic fields of these currents can be sensed on Earth, but they induce also currents in the ground. Electric and magnetic signals

at the surface caused by Pedersen currents exhibit spectral ratios that are independent of season and local time.

Conversely, the Hall currents caused by IEY generate magnetic signatures, but there is no electric field response. We suggest that the changing Hall current sets up a wavefield in the space between ionosphere and Earth with displacement currents in the atmosphere and return currents at Earths surface (see Fig. 3.22). A magnetic signal is detectable in the atmosphere but evanescent below the surface and above the ionosphere. Therefore, no induction takes place in the ground. If not considered, this can lead to a false interpretation of magnetotelluric data.

CHAPTER 4

The deep hydraulic system of the Andean subduction zone in Northern Chile

In this chapter I describe the removal of the observed source field effect from the VTF time series and the effort to explain the residual VTF variations by computation of 3D models of electrical resistivity structure of the subsurface.

4.1 Residual variations in the VTF time series

Identifying variations in VTF time series (see section 3.2) associated with changing electrical resistivity structure in the subsurface could give information about dynamic fluid processes in the north Chilean segment of the Andean subduction zone. In the previous chapter, I showed that the δT_i time series are heavily distorted by a varying source field effect. This source field effect dominates the temporal variation of the δT_i and thus might mask any variations which are possibly caused by internal parts of magnetic fields recorded by the IPOC sites.

δT_i variations caused by subsurface processes are extracted by a similar procedure like in section 3.3.1. Time series of daily differences δT_i are computed and a filter is applied to extract variations in the requested period range (Fig. 4.1). It is assumed that the electrical resistivity of the subsurface in the considered induction volumes (period $>$ 100 s) remains constant in time spans of at least several months. Consequently, a low-pass filter is applied to suppress variations with periods $<$ one year. The resulting low-pass filtered δT_i^{LP} time series exhibit an anomalous long term variation at the nearby IPOC sites PB04 and PB05 in a period range between 1500 and 4000 seconds (Fig. 4.2, period 2050 s). The amplitude of these variations is just above the noise level.

To quantify the amplitude and distribution of this variation in space, the same procedure as described in section 3.3.1 is used. The maximum and minimum δT_i^{LP} in the

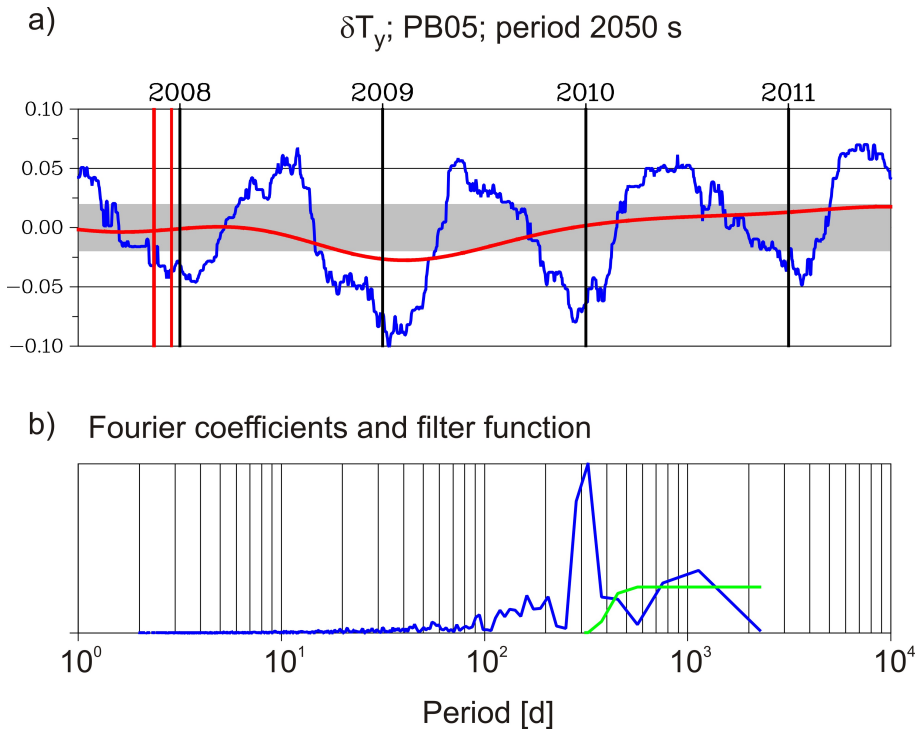

Figure 4.1: a) Smoothed time series of daily differences δT_y for site PB05 at a period of 2050 s for more than 4 years (blue curve). The red curve represents the low pass filtered δT_y^{LP} time series which contains only periods > one year. The red vertical lines indicate the occurrence of the 2007 Tocopilla earthquake and of the main aftershocks. The grey colour indicates error bounds of 0.02. The data errors of the daily VTFs depend on different parameters, e.g. instrument noise or daily varying source field characteristics. Since I use only three days of EM time series for statistical estimation of daily VTFs for periods > 1000 s, only a relative small amount of time windows can be stacked. In this case an estimation of an error bound is questionable, consequently I chose the value of 0.02 which is typically used for inversion of VTF data (e.g. Tietze, 2012; Tietze & Ritter, 2013). A variation within these error bounds can be considered as insignificant. b) Coefficients of the Fourier transformed time series. They are multiplied by the filter function in green, which is an adapted Parzen window. Subsequently, an inverse Fourier transformation is applied.

years 2008 and 2009 are searched to compute the absolute value of the difference vector $\left|\Delta\vec{P}(\tau)\right|$ (equation 3.3; Figure 3.8). I interpolate the $\left|\Delta\vec{P}(\tau)\right|$ laterally over the network (Fig. 4.3; colour coded). The sense of the variation is emphasized by induction vectors which represent the endpoints of the variation.

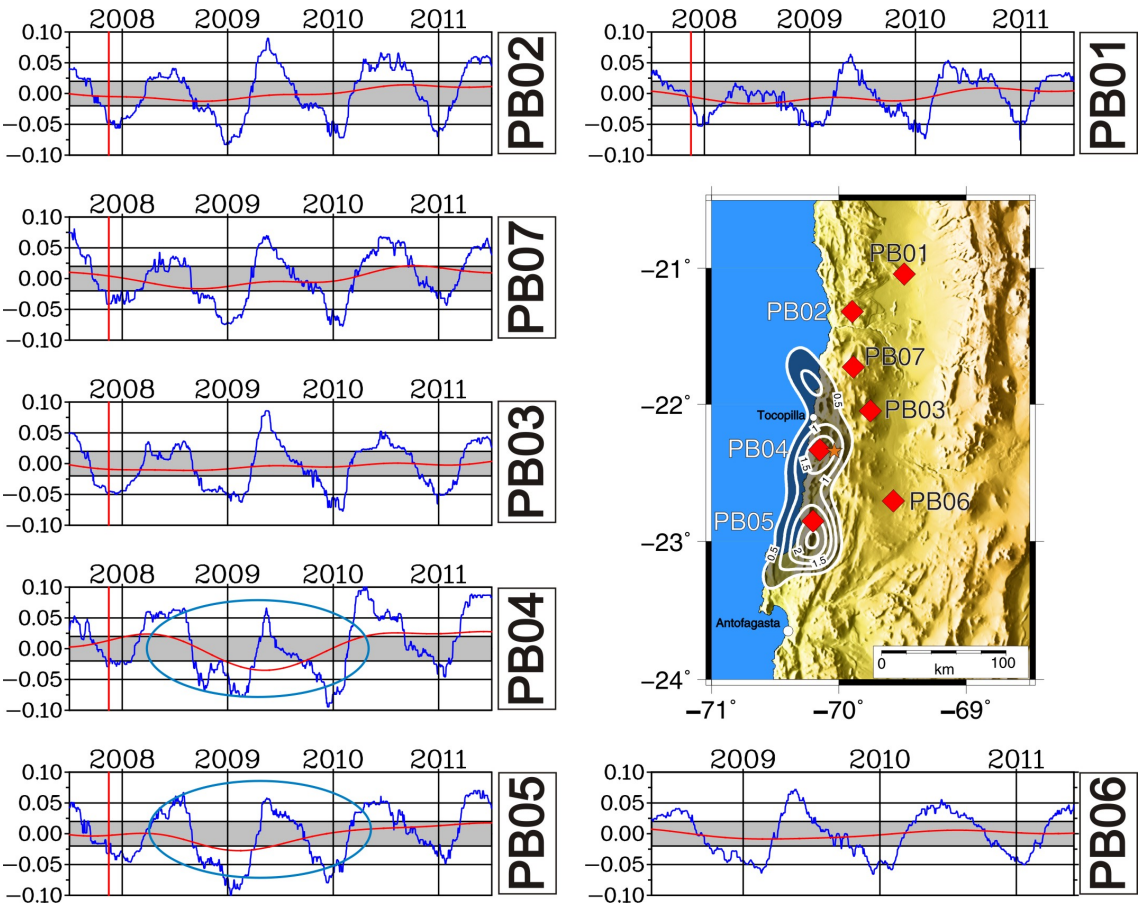

Figure 4.2: Original time series of real parts of δT_y for a period of 2050 seconds at several sites (blue curves). The red curves represent the low-pass filtered δT_i^{LP} time series which contains only periods > one year. The occurrence of the M7.7 2007 Tocopilla earthquake is indicated by vertical red line. The grey colour indicates the error bounds of 0.02 as usually used for inversion of VTFs. This means only variations > 0.02 are significant. In the map, station positions are indicated by red symbols. The epicentre of the M7.7 2007 Tocopilla earthquake is indicated by a orange star and the slip area of this event is indicated by contour lines after Schurr et al. (2012).

Generally, the absolute values of $\left|\Delta\vec{P}(\tau)\right|$ are below 0.02 and laterally uniform across the array for periods < 1500 s. This situation changes for periods > 1500 and < 4000 s, for which values reach approximately 0.05 at the sites PB04 and PB05. This enhanced amplitude of variation appears at only two neighbouring sites implying that this is not an external source field effect. Otherwise it would be observed at all sites of the network. Location and time of this variation indicate a modification of electrical resistivity structure

in the years 2008 and 2009 in the same region where enhanced co-seismic slip of the M7.7 2007 Tocopilla earthquake was observed (Fig. 4.3; Schurr et al., 2012). In order to verify and quantify a correlation, 3D forward model calculations are applied.

Figure 4.3 *(following page)*: Low pass filtered variation amplitudes $\left|\Delta\vec{P}(\tau)\right|$ (colour code) evaluated over a time span of approx. 1.5 years after the 2007 Tocopilla main shock, at exemplary periods. The green induction vectors indicate the initial state; the blue induction vectors the maximum deviation from the median. A significant shift of the arrow heads to the west is observed at sites PB04 and PB05 (c.f. Fig. 4.2) for periods of 2050 and 2900 seconds, indicated by the colour coded variation amplitudes. This area coincides roughly with the area of maximum slip of the M7.7 2007 Tocopilla earthquake, indicated as black contour lines with slip values in meter (Schurr et al., 2012).

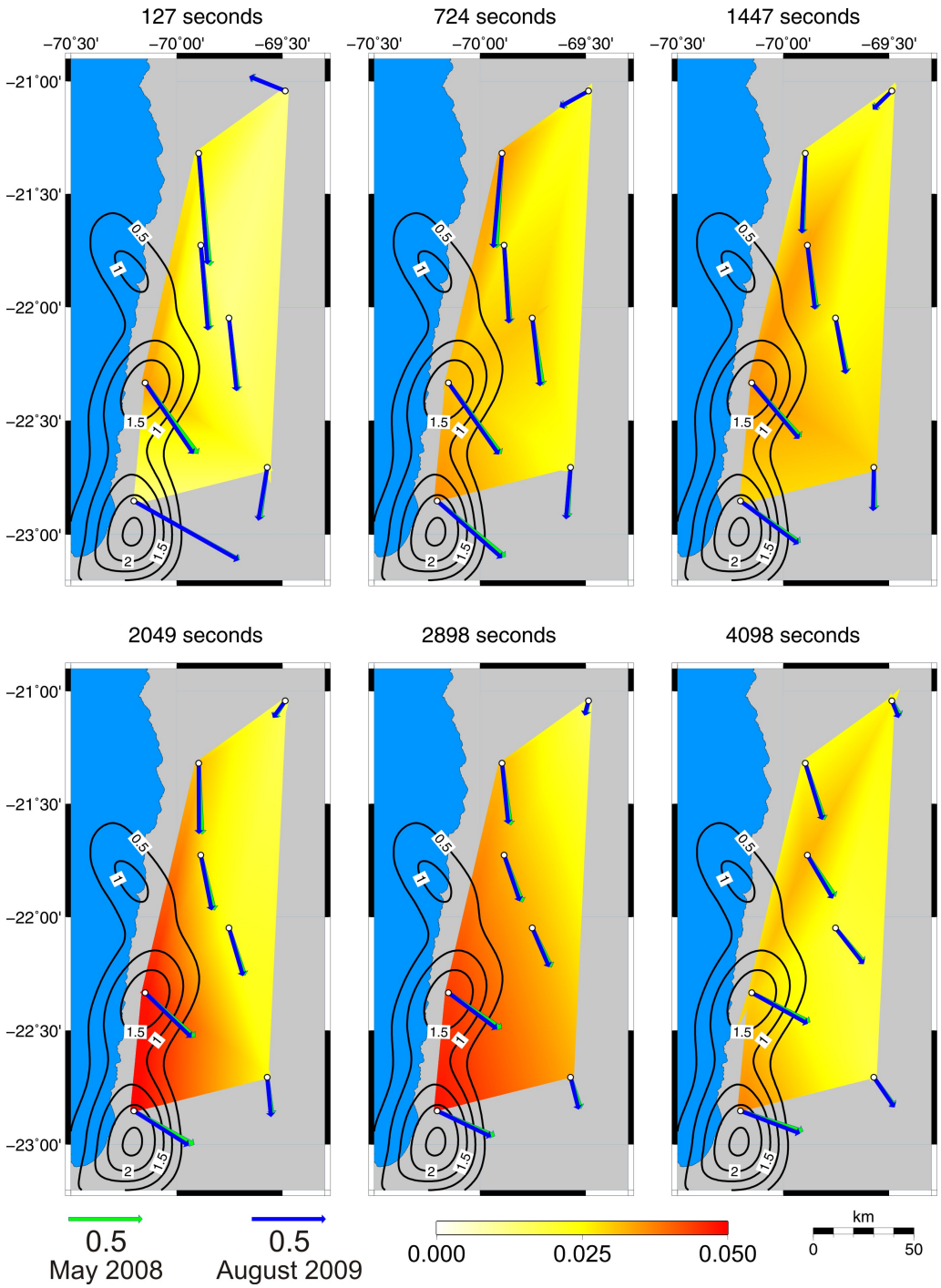
127 seconds
724 seconds
1447 seconds
2049 seconds
2898 seconds
4098 seconds
−70°30'
−70°00'
−69°30'
−21°00'
−21°30'
−22°00'
−22°30'
−23°00'
0.5
1
1.5
2
0.5
May 2008
0.5
August 2009
0.000
0.025
0.050
km
0
50

4.2 Principles of MT forward modelling and inversion

If the long term variations of VTFs are indeed caused by temporal changes of subsurface resistivity structure, what part of the subduction system needs to be modified to explain the data? To quantify such a variation, the following concept is applied: First, a 3D reference resistivity model is derived by 3D inversion of long term impedance and VTF data from the IPOC stations. This reference model and also the fitted data are defined to represent the long-term stable condition of the resistivity structure of the subduction system. The 3D electrical resistivity structure of the reference model is subsequently altered and the corresponding 3D forward model responses are computed at each of the IPOC stations. The obtained VTF data is compared with the data from the reference model to test if the modification can simulate the observed variation at sites PB04 and PB05 (Fig. 4.2). By trial and error, this process is repeated until a satisfying variation of VTFs at the requested sites (PB04 + PB05), components (T_y) and period lengths (1000 - 4000 s) (c.f. Fig. 4.3) is achieved. For 3D forward modelling and inversion of MT and VTF data, I used the the ModEM package (Egbert & Kelbert, 2012) with parallelisation schemes described by Meqbel (2009).

Principally, 3D forward modelling can be referred to as an operator $\mathbf{F(m)}$ which projects the model parameters $\mathbf{m}$ into data space, with an n-dimensional data vector $\mathbf{d}$, contaminated by errors $\mathbf{e}$:

$$\mathbf{F}(\mathbf{m}) = \mathbf{d} + \mathbf{e} \quad . \tag{4.1}$$

This implies that equation 1.9 for the electric field,

$$\Delta\vec{E} = i\omega\mu_0\sigma\vec{E} = k^2\vec{E} \quad , \tag{4.2}$$

is solved for $\vec{E}$ via parametrisation by finite differences of discrete model parameters. A 3D model of the earth is generated, consisting of discrete cubes of individual electrical resistivities ($1/\sigma$). The EM fields at the edges and faces of the cubes in the whole model are approximated by application of boundary conditions which are also used to simulate horizontal and uniform source fields. Depending on the location of the points of observation at the Earth model's surface in relation to the grid cells, the requested MT transfer functions are finally interpolated. This data is referred to as synthetic or predicted data.

3D inversion is an iterative process by which measured data are reproduced within some error bounds by predicting data from a 3D resistivity model. This is achieved by iterative minimisation of the misfit between measured and predicted data. The data misfit function $\Psi_d(\mathbf{m})$ to be minimised is defined as:

$$\Psi_d(\mathbf{m}) = ||\mathbf{Wd} - \mathbf{WF}(\mathbf{m})||^2 \quad , \tag{4.3}$$

W denotes a diagonal matrix containing the reciprocals of the data errors. This is a ill-posed problem since a large number of unknown model parameters (grid cells) is calculated by a relative small number of data points (Parker, 1980). For this reason, a regularisation term is added to stabilise the solution of this function (not shown).

Function Ψ_d cannot be minimised by a linear least squares approach since the forward operator **F** is not a linear function. In the case of the parallel version of ModEM, a non-linear conjugate gradient (NLCG) algorithm, which avoids computation of several large matrices, is used for inversion. This inversion scheme searches at each iteration step for the direction of the largest gradient of the penalty function Ψ_d with respect to a prior model. This determines the model update for the next iteration of the inversion. The inversion stops when a certain criterion based on the error of the data, or a given error floor is satisfied.

4.3 A 3D reference resistivity model derived by inversion of impedances and VTFs

For lack of alternatives I attempt to derive a reference 3D resistivity image of this part of the north Chilean subduction system from eight MT stations of our network. With the site distribution, a sufficient areal coverage can be achieved to obtain an image of the large scale resistivity structure to depths of several tens of kilometres below the coastal cordillera and the longitudinal valley. I appreciate that spatial resolution may be poor but at least the inversion model is based on real data.

All four components of the MT impedance tensor and VTFs were inverted. I had to resort to data beginning with January 2011, because the earlier recorded electric field data could not be used, at least not for longer time spans. Due to the extreme dry conditions of the Atacama Desert, it took several attempts before I managed to find an electrode installation which provided the necessary long term stability (section 2.2.2). Eventually, I could process 150 days, averaging over summer and winter time to suppress influences of seasonal varying source fields as found in section 3.3.1. The long recording time resulted in excellent quality for the east-west electric field components and reasonable data quality for the north-south electric field components which are typically more contaminated with noise because of strong current channelling in the Coastal Cordillera due to the coast effect (Lezaeta, 2001). The MT and VTF data were rotated by 3 degrees to account for the declination in the area.

For 3D inversion, I tested a number of grids with varying cell size to accommodate average site distances of approximately 50 km and a period range of 10 to 10^5 seconds. Eventually, I resorted to a grid of 70 x 70 x 40 cells and a horizontal resolution of 15 by 15 km in the core. The thickness of the first layer was set to 0.5 km and the vertical increasing factor to 1.4; the total depth of the model is approximately 3,600 km. All starting models included a fixed ocean using rough 3D bathymetry and an average resistivity of 0.3 Ωm for the ocean water. After some forward modelling tests, I set the remaining background resistivity of the starting/prior model to 10 Ωm.

I inverted full impedance and VTF data at 15 periods between 10 and 10^5 seconds. At all sites, I observe Z_{xy} impedance tensor elements by orders of magnitude larger than the corresponding Z_{yx} components. Tietze (2012) pointed out that in this situation conductive structures, associated with the smaller impedance component, are not recovered if common error bounds of $|Z_{xy}\ Z_{yx}|^{\frac{1}{2}}$ are used for all impedance components. Consequently, I set the error floors to 3% for both off diagonal elements of the impedance tensor, and used error floors of 3% of $|Z_{xy}\ Z_{yx}|^{\frac{1}{2}}$ for the diagonal elements; errors for the VTFs were set to 0.02.

For the inversion model shown in Figures 4.4 and 4.5, the starting normalized misfit of 17.8 reduced after 160 iterations to 4.4. The impedance data and fit curves are presented as apparent resistivity and phase curves in Figure 4.6, also the real parts of VTFs are shown. The overall data fit is satisfying, at site PB05 phases above 90° were fitted and curve shapes and large split-up of the impedance components are generally reproduced at all sites. Also the main-diagonal apparent resistivity and phase components show principally a good fit. Special attention was paid to fit VTFs which are also well reproduced by inversion. This is remarkable since at several sites the induction vectors at periods < 4000 s are pointing nearly coast-parallel towards south/south-east (Fig. 4.3), which is expressed by large negative T_x components in Figure 4.6. For the survey area in Northern Chile, located

Figure 4.4 *(following page)*: Horizontal sections of electrical resistivity resulting from 3D inversion of impedances and VTFs at 8 monitoring sites (white circles, site names are indicated in the top panel at the left hand side). This model was obtained after 160 iterations with a total RMS of 4.4. Structure (I) is not resolved (no site coverage), structure (II) is robust and required by the data. The black lines connecting the panels show the longitudinal location where the vertical electrical resistivity section in Figure 4.5, indicating the depth extend of structure (II), was extracted. Data and fit curves are shown in Figure 4.6. Shaded areas bordered by dashed black lines indicate areas with low resolution (see section 4.4).

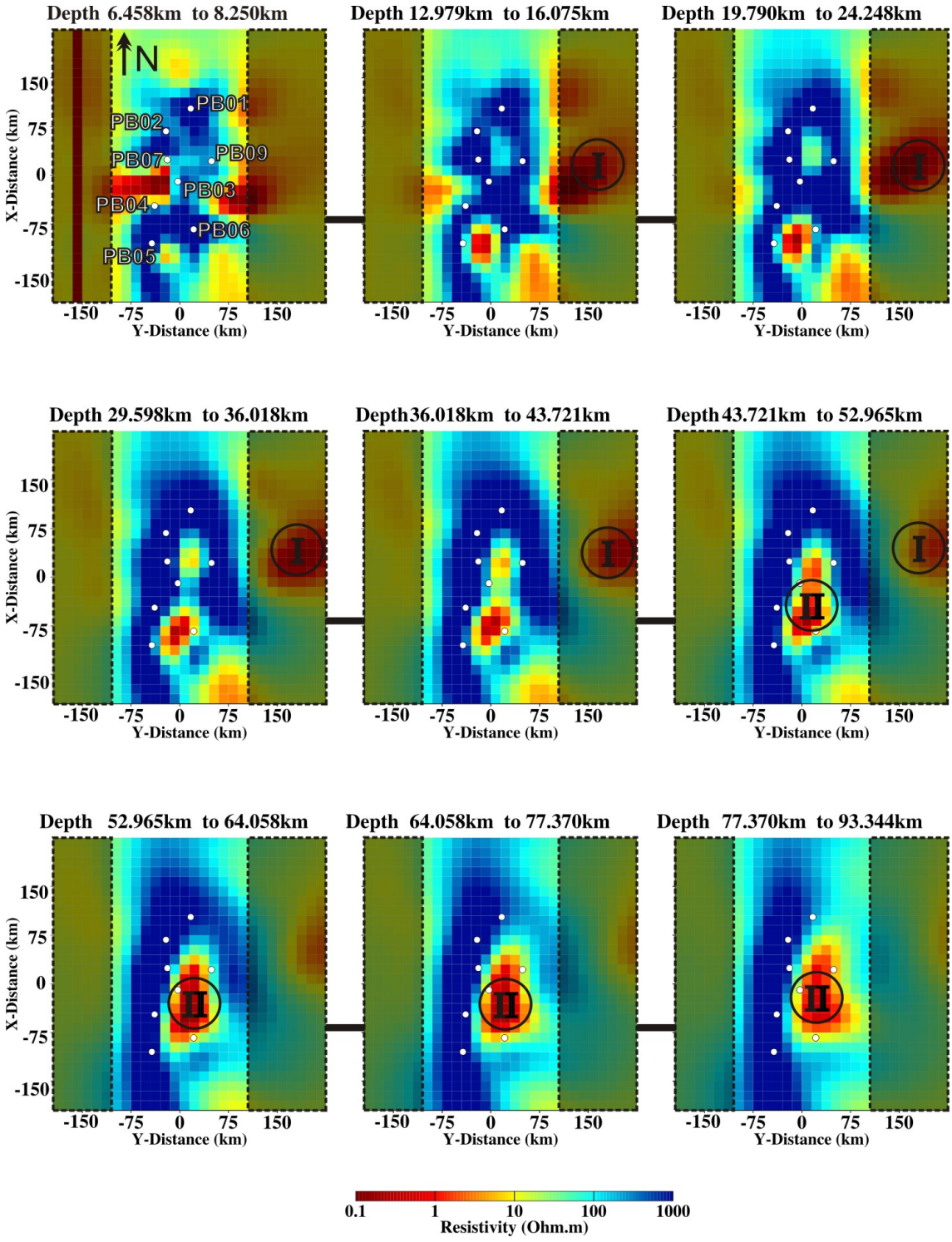
Depth 6.458km to 8.250km
Depth 12.979km to 16.075km
Depth 19.790km to 24.248km
Depth 29.598km to 36.018km
Depth36.018km to 43.721km
Depth43.721km to 52.965km
Depth 52.965km to 64.058km
Depth 64.058km to 77.370km
Depth 77.370km to 93.344km
N
PB01
PB02
PB07
PB09
PB03
PB04
PB06
PB05
I
II
X-Distance (km)
Y-Distance (km)
150
75
0
-75
-150
0.1
1
10
100
1000
Resistivity (Ohm.m)

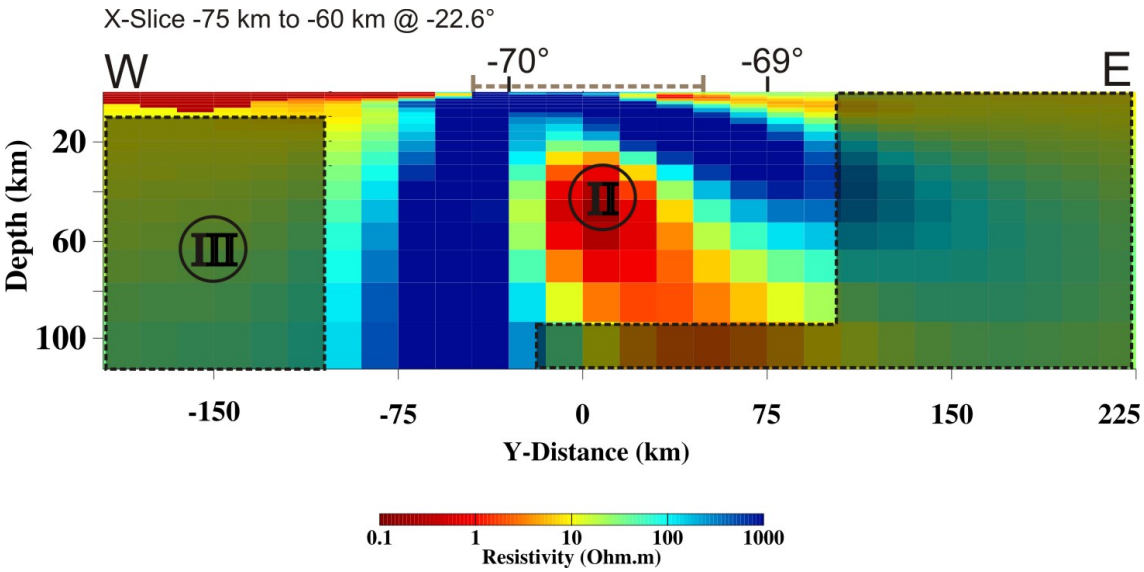

Figure 4.5: Vertical electrical resistivity section displaying structure (II) with depth. The width of the section corresponds to the width of the horizontal sections in Figure 4.4. The latitudinal location is indicated by the horizontal black line connecting the slices in Figure 4.4 which also shows the location of stations. The east-west extend of the IPOC-MT network is indicated by the brown dashed line at the upper edge of the section. Shaded areas indicate areas with low resolution (no site coverage).

directly at the Pacific Ocean, normally a predominant coast effect would be expected which causes induction vectors pointing away from the big volume of highly conductive seawater. This effect of oblique striking induction vectors was observed before by different authors in Northern Chile (Schwarz & Krüger, 1997; Brasse & Eydam, 2008), who suggested anisotropy as a cause when using 2D interpretation tools. In this study, the resulting electrical resistivity structure from 3D inversion fits the VTF and impedance data without any anisotropic structures in the Coastal Cordillera and Longitudinal Valley. The rotation of the predicted induction vectors to a coast parallel angle at several sites is in the inversion model mainly achieved by shallow, oblique striking electrical resistivity structures, but at shallow depth the resolution is limited due to the sparse site distribution. For a detailed interpretation of these features, a finer grid and a significantly denser site coverage would be necessary.

In the survey area in Northern Chile several shallow structures exist which could be responsible for near-surface electrical conductors of the inversion model. A highly conductive pattern at surface (depth of 0 - 1 km) north of sites PB02, PB03 and PB07 (Fig. 4.7) could reflect the influence of the Salar Grande and parts of the Atacama Fault

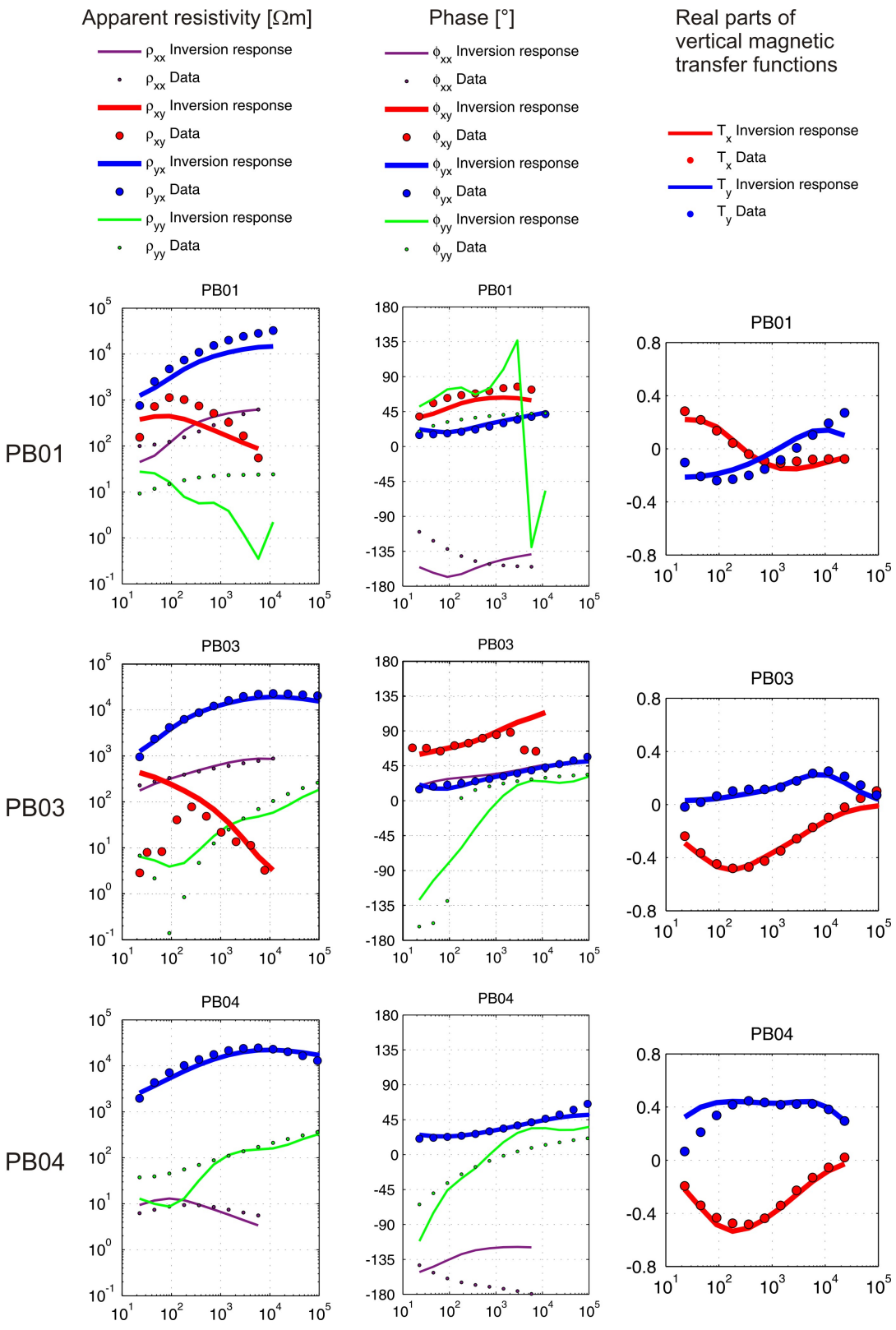
Apparent resistivity [Ωm]
ρxx Inversion response
ρxx Data
ρxy Inversion response
ρxy Data
ρyx Inversion response
ρyx Data
ρyy Inversion response
ρyy Data
Phase [°]
ϕxx Inversion response
ϕxx Data
ϕxy Inversion response
ϕxy Data
ϕyx Inversion response
ϕyx Data
ϕyy Inversion response
ϕyy Data
Real parts of vertical magnetic transfer functions
Tx Inversion response
Tx Data
Ty Inversion response
Ty Data
PB01
PB03
PB04

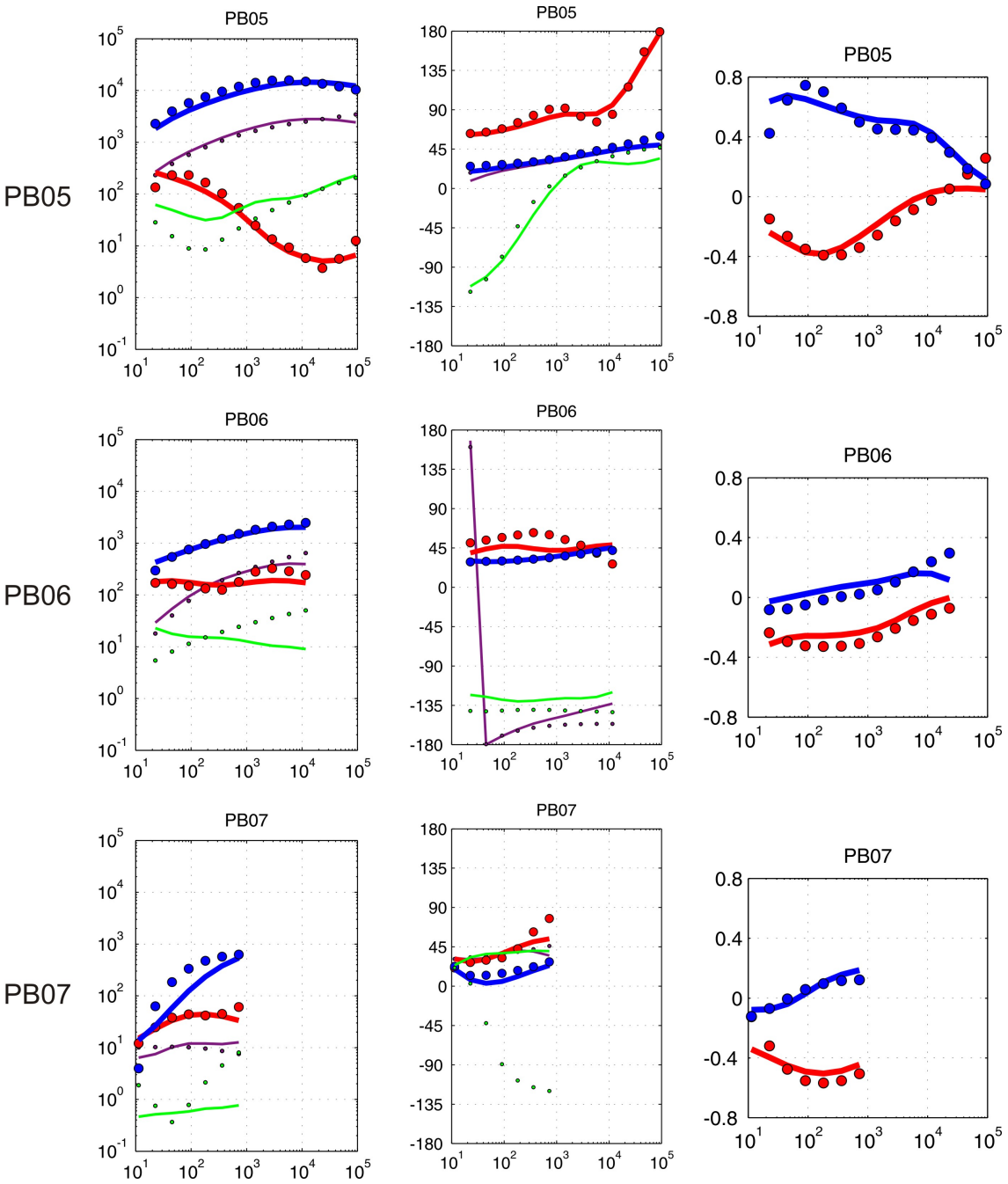
PB05
PB06
PB07
PB05
PB05
PB05
PB06
PB06
PB06
PB07
PB07
PB07

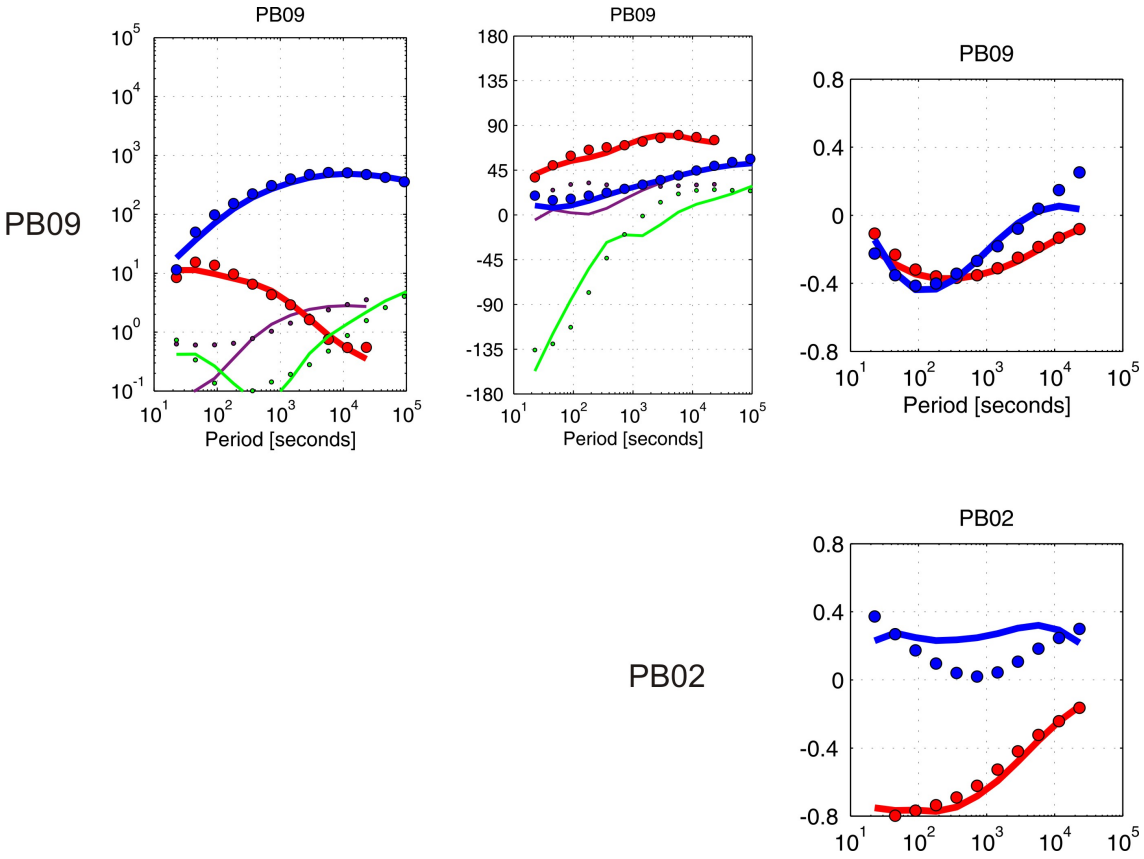

Figure 4.6: *(preceding pages)* Data and fit curves obtained by the 3D inversion, points indicate measured data, solid lines indicate inversion response. Shown is the data fit for all four components of apparent resistivity and phase and real parts of the vertical magnetic transfer functions. The large split up of apparent resistivity components is reasonably fitted; also the phase $> 90°$ at site PB05 is reproduced by the inversion. Several components were excluded from inversion due to poor data quality.

System (Fig. 4.8). Lezaeta (2001) showed that a good conducting structure at this location causes nearly coast parallel induction vectors. North of PB06 there is another conductive, shallow structure (not shown) which might be related to the Rio Loa and salt deposits in the Longitudinal Valley (c.f. Chong, 1984).

Generally, the model derived by 3D inversion exhibits a pronounced three-dimensional character of the electrical resistivity structure of the subsurface in the survey area (Fig. 4.7). Parts of the volume below the region with station coverage appears predominantly as highly resistive ($> 1000\ \Omega m$). This highly resistive subsurface is consistent with the observed large Z_{yx} components (Fig. 4.6) and with earlier results by Schwarz & Krüger

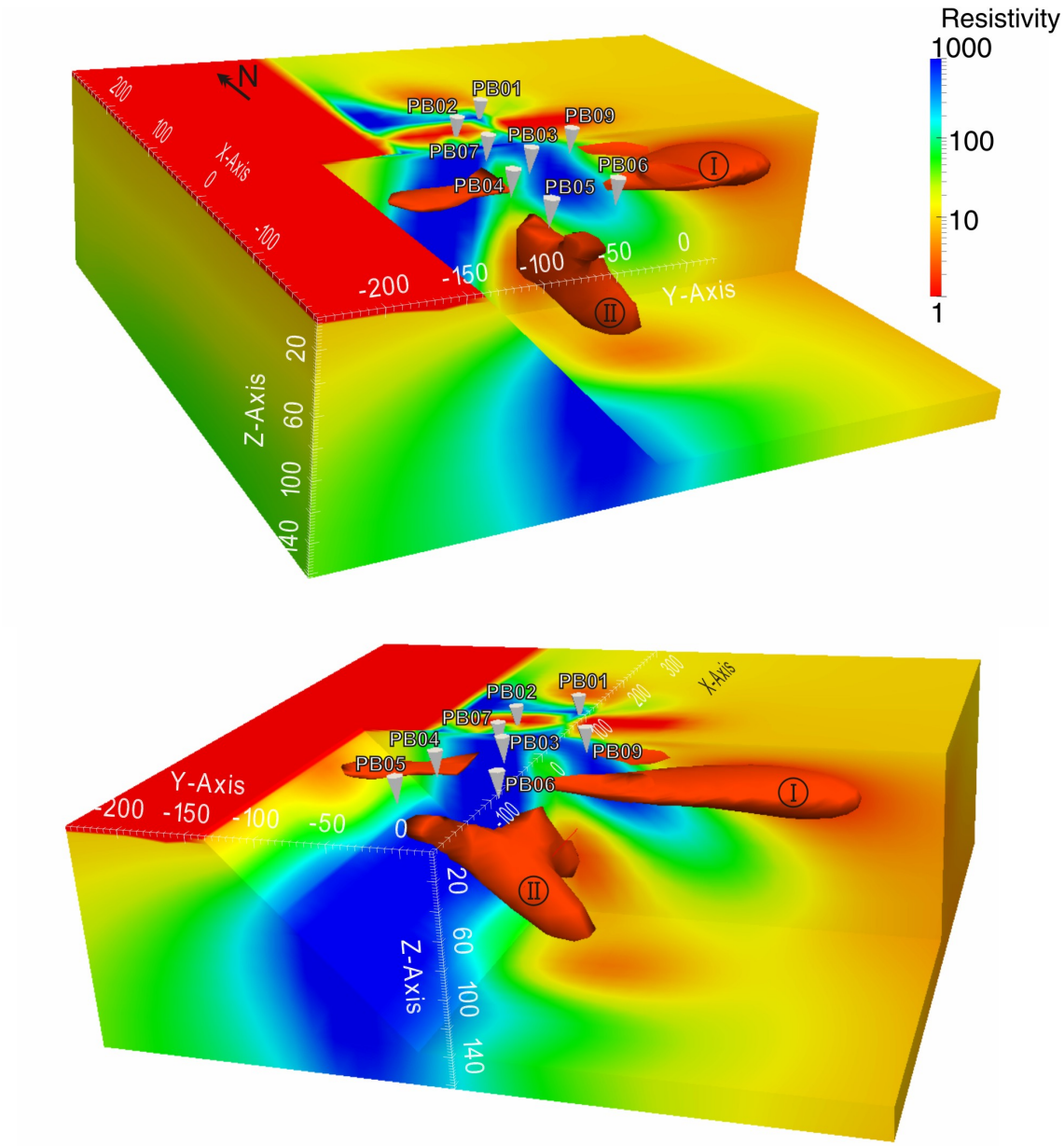

Figure 4.7: Partially recessed 3D views of the electrical resistivity model obtained by inversion, shown in Figures 4.4 and 4.5, illustrating the three-dimensional character of the model (depth 0 - 160 km). The resistivity values are interpolated and the bodies in the open volume are iso-surfaces at 2 Ωm. Station locations are indicated by the white polygons. The axes indicate kilometres from model centre. Upper panel: View form SW. Lower panel: View from SE.

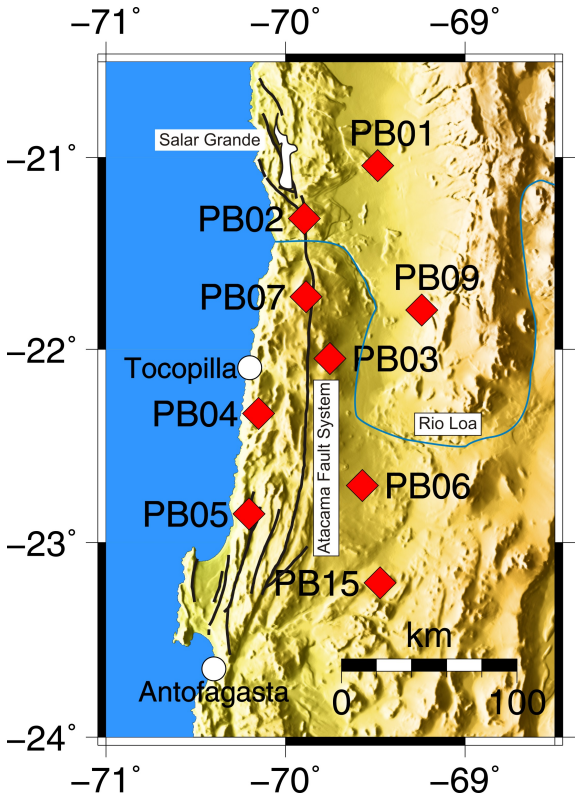

Figure 4.8: Map indicating the location of IPOC MT monitoring sites and parts of the Atacama Fault system, Rio Loa and Salar Grande Basin. White circles indicate cities of Antofagasta and Tocopilla.

(1997); Echternacht et al. (1997); Brasse et al. (2002) for the same region. It may reflect the subducted cold oceanic lithosphere. Different highly conductivity features, labelled (I) and (II) in Figures 4.4, 4.5 and 4.7 can be observed at greater depths.

4.4 3D inversion model resolution tests

In several steps I tested the robustness of the main structural features obtained by the 3D inversion (Figs 4.4 and 4.5). This procedure is essential since I refer to only eight sites covering an area of approximately 250 x 100 km^2. A feature which is only observed by data of one station is not completely reliable even though the data is based on EM time series of 150 days which were carefully processed and handled. It is desirable that an electrical resistivity structure is at least sensed and required by two stations and several data components. That implies that only regional structures at greater depths can be resolved and evaluated.

With this in mind, the main electrically conductive sub-domains of the 3D inversion model were masked one at a time. The electrical resistivity values were replaced by those of the immediate vicinity. The predicted data of each resistivity model variation were computed by 3D forward modelling using ModEM. The resulting data was compared with the inversion data in order to check for an influence on the various impedance and VTF components. If an noticeable influence is observed, the electrical resistivity of this feature was gradually restored to find out which part of a body or structure is responsible for the influence on the data. Also the depth resolution of the entire model and the areas to the east and west were checked.

Not clearly resolved is structure labelled (I) in Figure 4.4, located north-east of the station network. Its influence is only sensed noticeably by the diagonal components ρ_{yy} and ϕ_{yy} in the period range 10^2 - 10^4 s at site PB09 (not shown). Also moderate changes of electrical resistivity in the volume labelled (III) below the Pacific Ocean (Fig. 4.5) have no significant influence on the stations data. This part of the model parameter space do not cause an effect in the data, consequently it belongs to the Null Space.

In contrast, all tests on the conductive structure (II), located towards the centre of the network, confirmed that it is required by several data components and stations. In particular $\phi_{xy} > 90°$ at site PB05 (Fig. 4.9), but also ρ_{xy}, ϕ_{yy} and real T_y components at

Figure 4.9 *(following page)*: Exemplary 3D resolution test. a) Vertical section showing a modification of the inversion model (Fig. 4.5) by replacing conductive structure (II) with electrical resistivity of 100 Ωm. The longitudinal extend of the IPOC-MT network is indicated by a brown dashed line on top of the section. b) Comparison of predicted data from the modified model, data from the inversion and real data. A significantly worse data fit for different components of apparent resistivities ρ, phases ϕ and VTFs at different stations can be observed if structure (II) is masked.

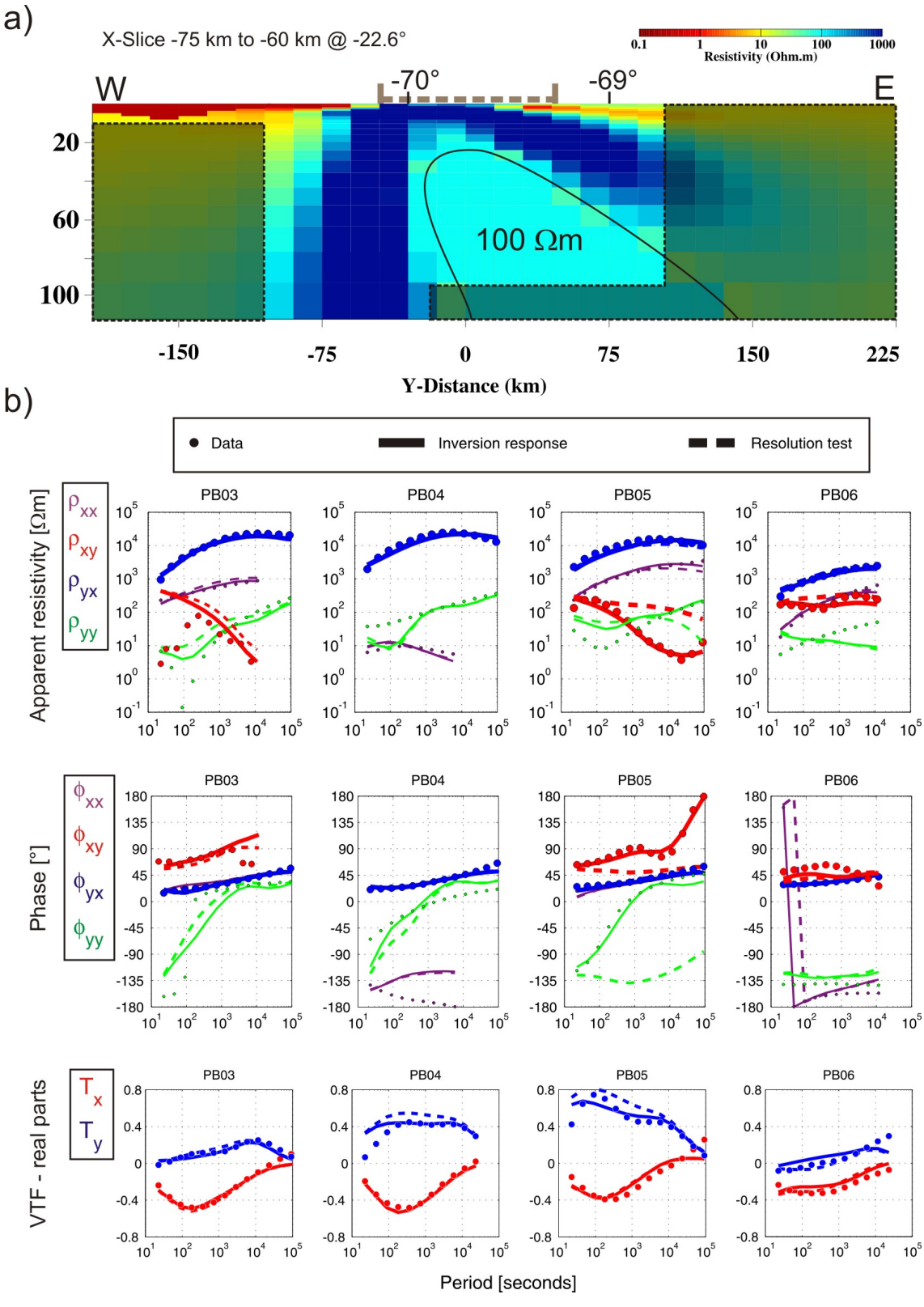
a)
X-Slice -75 km to -60 km @ -22.6°
Resistivity (Ohm.m)
0.1
1
10
100
1000
W
-70°
-69°
E
20
60
100
100 Ωm
-150
-75
0
75
150
225
Y-Distance (km)
b)
Data
Inversion response
Resolution test
Apparent resistivity [Ωm]
ρxx
ρxy
ρyx
ρyy
PB03
PB04
PB05
PB06
Phase [°]
ϕxx
ϕxy
ϕyx
ϕyy
VTF - real parts
Tx
Ty
Period [seconds]

several stations show an noticeable influence. Checking the lower boundary of structure (II) shows that it must extend at least to a depth of approximately 90 km (Fig. 4.5). As mentioned in section 4.3, the inversion includes structure (II) - thereby reaching an acceptable misfit - only if the smaller off-diagonal component (Z_{xy}) is weighted appropriately by setting individual error bounds for all impedance tensor elements.

The result of the 3D inversion is unexpected since a conductive structure marked as (II) in Figure 4.5 below the Coastal Cordillera and Longitudinal Valley was not found in former studies in this area (Schwarz & Krüger, 1997; Echternacht et al., 1997; Brasse et al., 2002). Evans (2002) suggested that in principle only offshore MT data is able to sense the electrical resistivity structure of the hydrated mantle wedge overlying the slab at an ocean-continent subduction zone. This author used a 2D model based on Echternacht et al. (1997) and computed synthetic TE and TM phases at on- and offshore sites. The results of Evans (2002) show that a conductive structure at the position of the mantle wedge generally have greater influence on the TM mode compared to TE. The TE mode of Evans (2002) corresponds to the Z_{xy} component of our study. In contrast to Evans (2002), a conductive feature at the Andean subduction zone in Northern Chile at the location of the hydrated mantle wedge was imaged using exclusively onshore data including VTFs. Structure (II) was revealed only if the smaller off-diagonal component Z_{xy} is weighted appropriately in 3D inversion by setting individual error bounds for all impedance tensor elements.

4.5 Simulation of spatio-temporal variations of the 3D electrical resistivity structure

In this section I examined if changes in the VTFs, as observed over a time-span of 1.5 years at two adjacent sites (c.f. sec. 4.1), can be explained by changes of subsurface resistivity structure. The 3D reference resistivity model obtained by 3D inversion was used as a starting point for simulating the observed variation of VTFs as described in section 4.1 (Figs 4.2, 4.3 and 4.7). At this point again, the non-uniqueness of the magnetotelluric inverse problem has to be considered (c.f. section 4.2).

In principle I try to find a model modification which causes a specific data variation. To solve an ill-posed inverse problem, which is the result of a small number of stations and spatially under-sampled data, a limited frequency band and coarse model parametrisation (Parker, 1980) for such a small data variation as observed is not feasible. Consequently, I manipulated the resistivity structure of the reference model and calculated the forward response. The resulting VTFs were compared to the VTFs obtained by the inversion in

order to identify changes produced by the modified resistivity structure. This procedure was repeated by trial-and-error until I found a modification of electrical resistivity which could reproduce the observed VTF variation from section 4.1.

Since the variation of VTFs is observed only at two adjacent MT monitoring sites (c.f. Fig. 4.3), I aim to reproduce this variation with one single structure and with the simplest possible shape. I assume one electrical resistivity value for the entire structure to be modified. Consequently, location, size, shape and uniform resistivity of the anomalous volume have to be identified. I tested a series of volume shapes (different cuboid shapes and combinations of cuboid shapes), orientations, resistivity values (0.1 - 10 Ωm) and locations. In total, I computed more than 50 3D forward calculations until a suitable modification was found. It turned out that the edges of the modified volume cannot be adjusted axes-parallel.

Figures 4.10 and 4.11 illustrate our preferred solution. The anomalous volume measures approximately 90 x 60 x 25 km^3 and is located at approximately 50 km depth with its major axis extending in north-west/south-east direction. Its resistivity of 0.5 Ωm corresponds to a decrease of 1.5 to 2.5 orders of magnitude from the reference model. Changes of VTF responses caused by the modified volume are most pronounced at sites PB04 and PB05, where the amplitude of T_y (real part) reduced by values of approximately 0.04 at periods of 10^3 - 10^4 seconds (Figs. 4.12 and 4.13). For the other VTF components and at other sites differences are below the resolution threshold (< 0.02).

The influence of the modified resistivity structure on the predicted data depends on the resistivity structure of the reference model. As the reference model was obtained from only eight stations, it is quite limited in resolution, and shape and resistivity of the modified volume may differ slightly for a better reference model. However, the depth of the modified electrical resistivity volume would be most likely similar.

Figure 4.10 *(following page)*: Anomalous volume which can explain the VTF variation. a) Horizontal sections of electrical resistivity obtained by 3D forward modelling. The hatched area (white outline) indicates the volume of varied resistivity. White circles indicate station locations. b) Vertical section of electrical resistivity, the latitudinal location is indicated by the horizontal black line connecting the slices in (a). The longitudinal extend of the IPOC-MT network is indicated by the brown dashed line on top of the section. Shaded areas (dashed black outlines) indicate areas with low resolution.

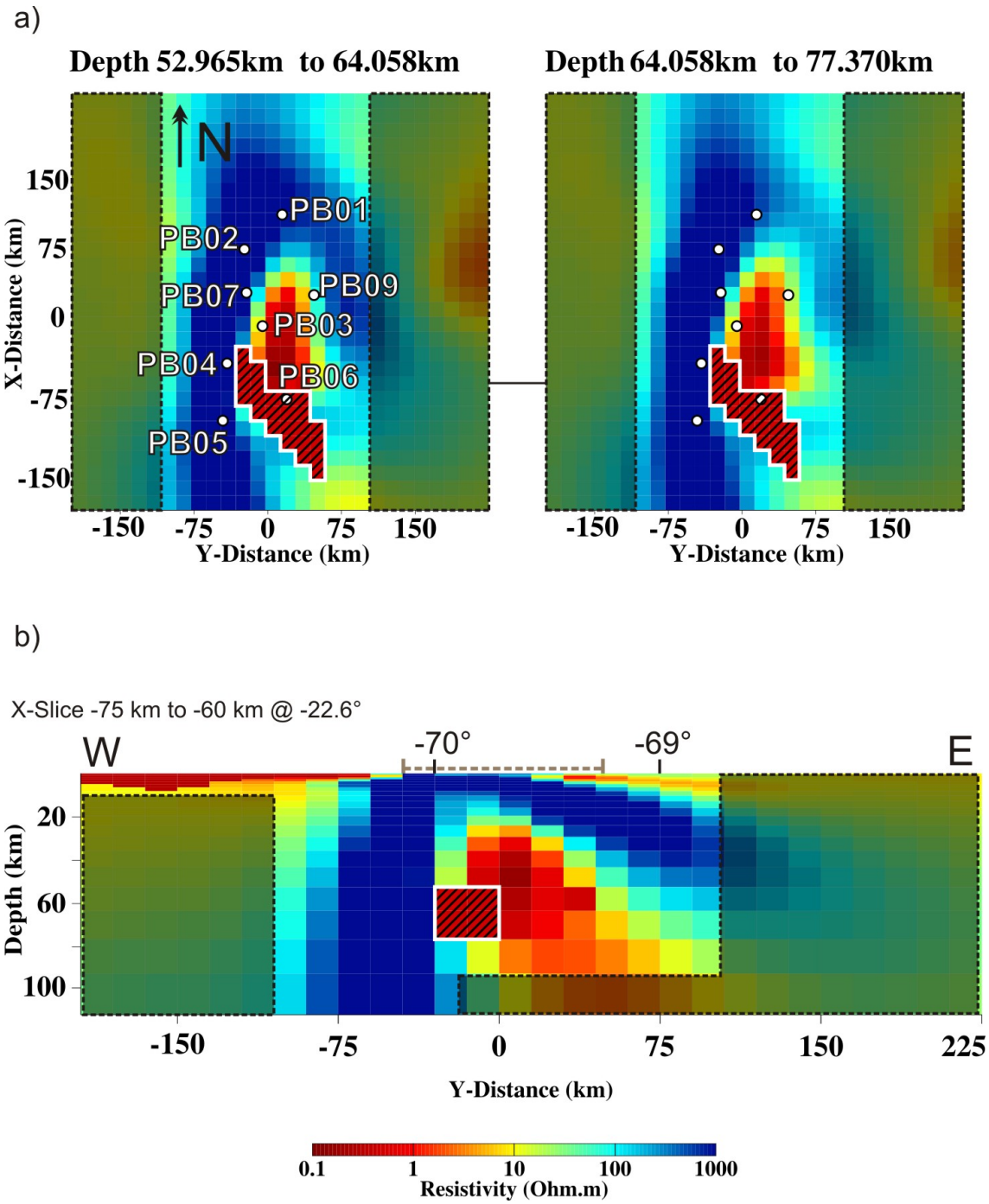
a)
Depth 52.965km to 64.058km
Depth 64.058km to 77.370km
N
PB01
PB02
PB07
PB09
PB03
PB04
PB06
PB05
X-Distance (km)
Y-Distance (km)
b)
X-Slice -75 km to -60 km @ -22.6°
W
E
-70°
-69°
Depth (km)
Y-Distance (km)
0.1
1
10
100
1000
Resistivity (Ohm.m)

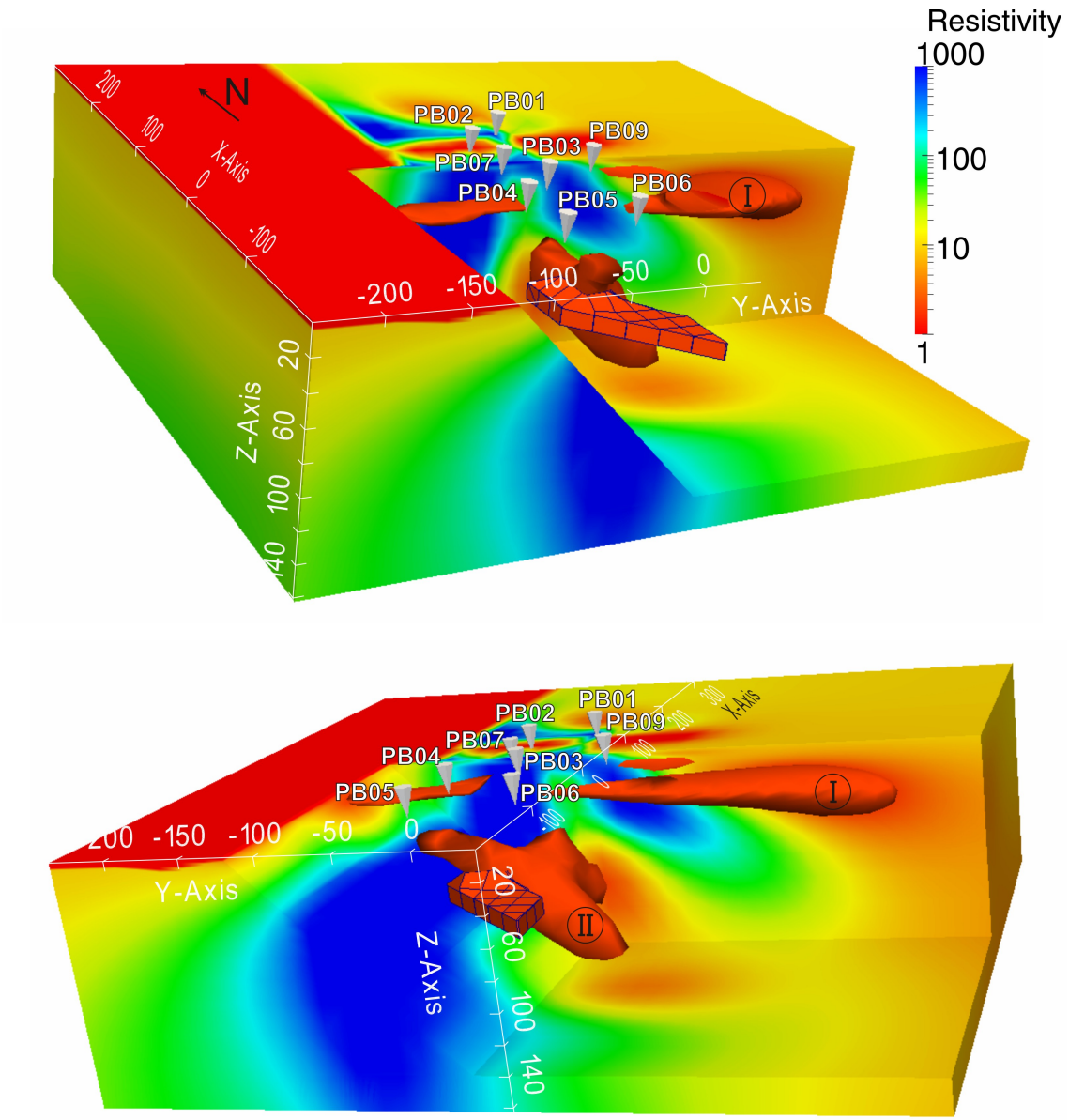

Figure 4.11: Partially recessed 3D views of the electrical resistivity model obtained by 3D forward modelling, shown in Figure 4.10, illustrating the three-dimensional character of the volume of varied resistivity. The resistivity values are interpolated and the bodies in the open volume are iso-surfaces at 2 Ωm. Station locations are indicated by grey polygons. Upper panel: View form SW. Lower panel: View from SE. Structure I is poorly resolved.

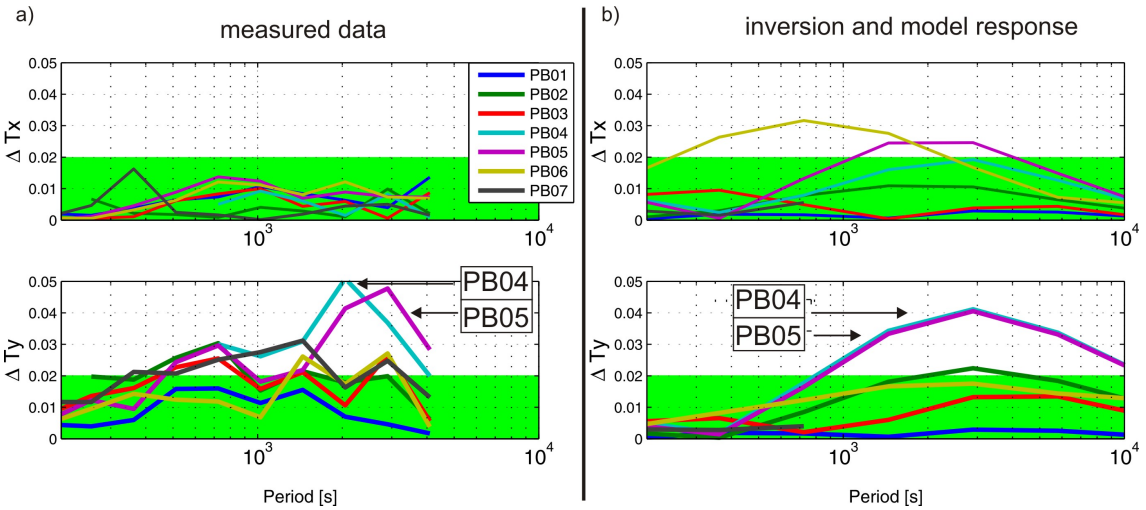

Figure 4.12: Comparison of differences ΔT_i of VTFs (real parts) vs. period. a) Temporal differences between VTFs from January 2008 and March 2009, extracted from the LP filtered time series (c.f. Fig. 4.2). The first date represents the "initial state", the second date the condition of maximum variation. The green box indicates the significance level of 0.02 (c.f. Fig. 4.2). Only ΔT_y at sites PB04 and PB05 are significantly above the noise level. b) Differences between VTFs of the reference model (Fig. 4.7) and from forward modelling (Fig. 4.11). ΔT_y at sites PB04 and PB05 show an amplitude behaviour similar to a), but over a wider period range. At PB06 and PB05, we also observe an unwanted ΔT_x slightly above the 0.02 error bound.

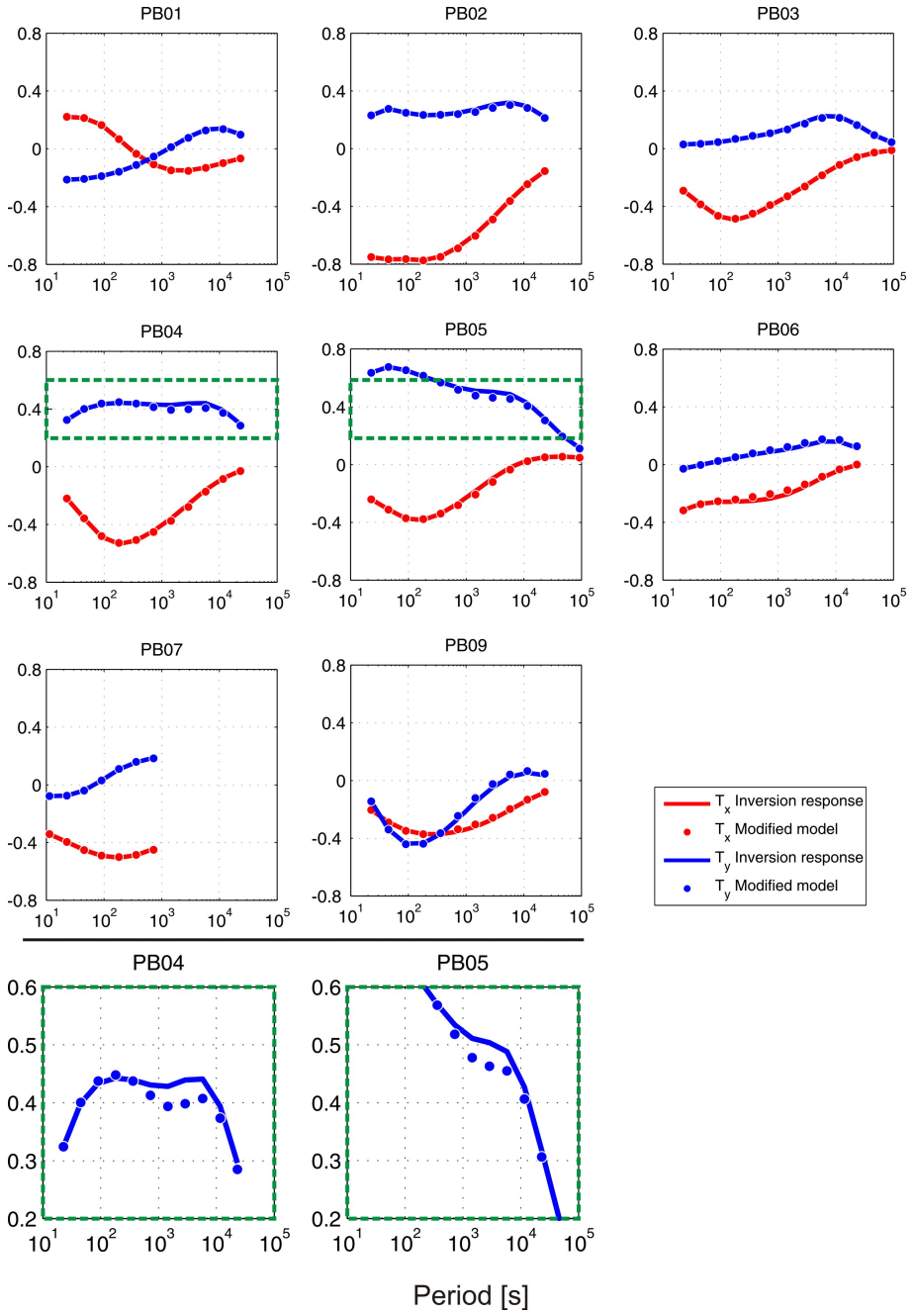

Figure 4.13: Comparison of VTF responses (real parts) of the reference model (solid curves, c.f. Fig. 4.5) and the modified model (circles, c.f. Fig. 4.10). Pane views of T_y responses at sites PB04 and PB05 indicated by green boxes are displayed in bottom panels. The variation of T_y fits in amplitude and period range roughly the observed variation in the real data (c.f. Fig. 4.12).

4.6 Discussion and interpretation

The most prominent feature of the 3D electrical resistivity inversion model is conductive structure (II) located below the Coastal Cordillera and Longitudinal Valley at approximately 20 - 80 km depth (Fig. 4.14 a). Projected locations of the M7.7 2007 Tocopilla earthquake and its aftershocks, which occurred during the subsequent six days (white circles in Figs 4.14 a and b), are used to delineate the plate interface (Schurr et al., 2012). Also shown in Figures 4.14 (a) and (b) are the continental Moho and the subducted Nazca Moho as interpreted from migrated P receiver functions by Sodoudi et al. (2011). Closer inspection of our inversion model with seismological results shows a strong spatial coincidence of conductor (II) with the suggested location of a hydrated mantle wedge (Fig. 4.14 a).

Schurr et al. (2012) pointed out that the missing intersection between oceanic crust and the continental Moho in the seismological section may be a consequence of a low seismic impedance contrast between serpentinised mantle rocks and a mafic lower crust. Active serpentinisation is considered to be associated with the release of fluids which decrease the electrical resistivity of the corresponding region in the subsurface (e.g. Hyndman & Peacock, 2003; Becken et al., 2011). The existence of the high conductivity of structure (II), which is a robust feature in our 3D inversion, is consistent with a hydratisation of the mantle wedge.

The western boundary of structure (II) coincides also with a significant contrast in measured heat flow (Fig. 4.15). However, our resistivity model suggests that the western limit of the hydrated mantle wedge is located significantly further west than indicated by the temperature model of Springer (1999). This may be the consequence of the different physical parameters to be compared, electrical resistivity and temperature. Shankland & Ander (1983) suggested that changes of temperature have a minor effect on the resistivity of fluids in this depths compared to other influences, e.g. fluid concentration.

Chlieh et al. (2004) suggested a down-dip variation of the frictional behaviour of the seismogenic coupling zone in Northern Chile. These authors found that the thrust interface is inter-seismically locked down to a depth of approximately 35 km, followed by a kinematic transition zone extending to a depth of approximately 55 km where the inter-seismic slip rate increases from zero to plate convergence rate. The down-dip limit of this transition zone matches with the extent of the Tocopilla earthquake slip area (Fig. 4.16 a). Below this range, the thrust interface appears as an aseismic creeping zone overlain by the serpentinised mantle wedge (Schurr et al., 2012). Audet et al. (2009) interpreted the aseismic creeping zone as a permeable plate boundary section located down-dip of the inter-seismically sealed zone (Fig. 4.16 b). A permeability of this section could allow con-

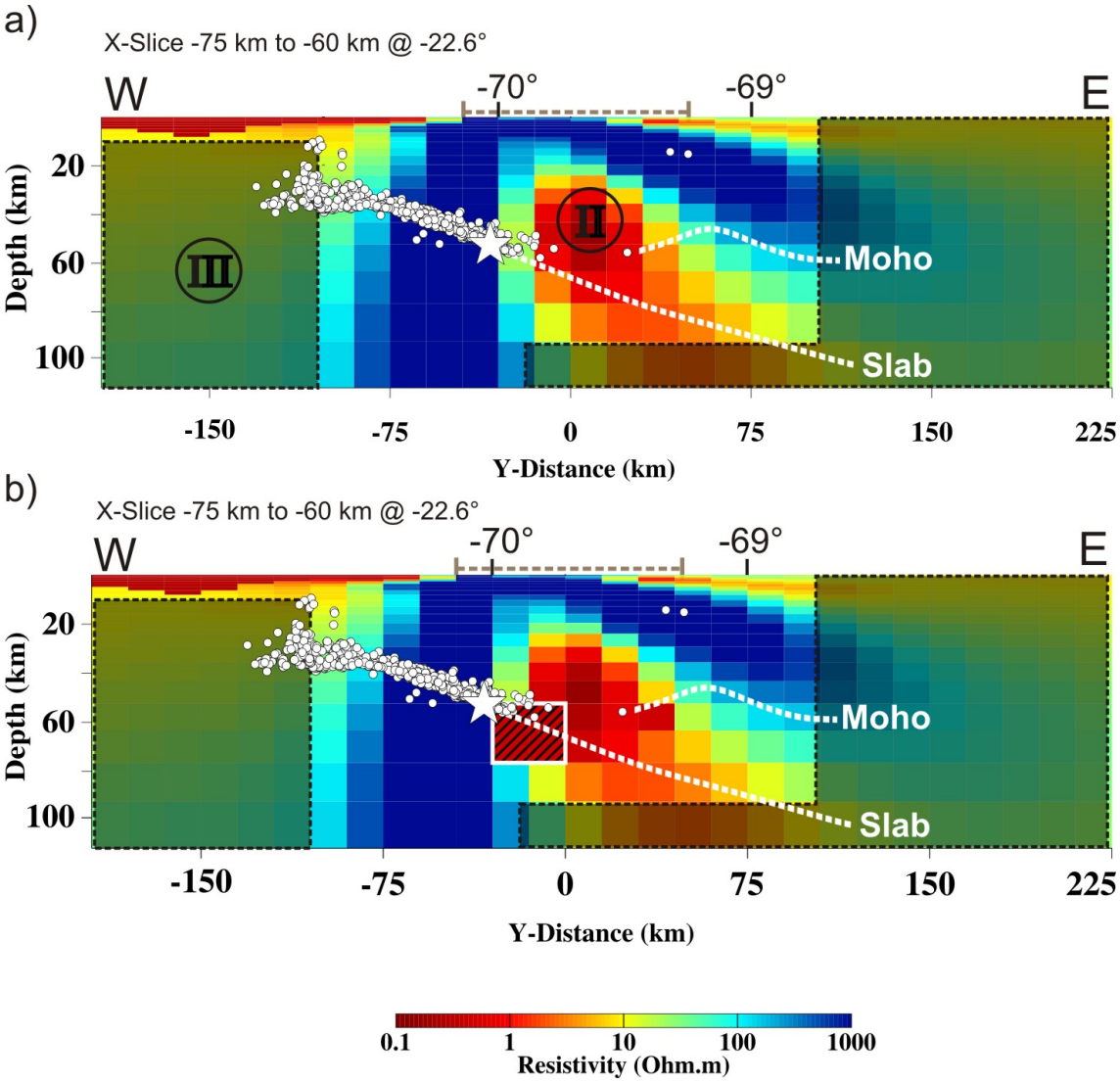

Figure 4.14: Vertical sections of a) the 3D inversion result (upper panel, c.f. Fig. 4.5) and b) the 3D forward model which generates the observed variation of VTFs (lower panel, c.f. Fig. 4.10 b). The east-west extent of the IPOC-MT network is indicated by the brown dashed lines on top of the sections. White circles indicate projection of aftershocks of the M7.7 2007 Tocopilla Earthquake (taken from Schurr et al., 2012). The white star indicates the main shock which occurred roughly 30 km north of the displayed section. Slab and Moho as found by Sodoudi et al. (2011) are marked by white dashed lines. The zone of modified resistivity (hatched area with white outline) is located directly down dip of the M7.7 2007 Tocopilla earthquake slip area at the predicted intersection of oceanic crust and continental Moho. Shaded areas indicate zones with low resolution.

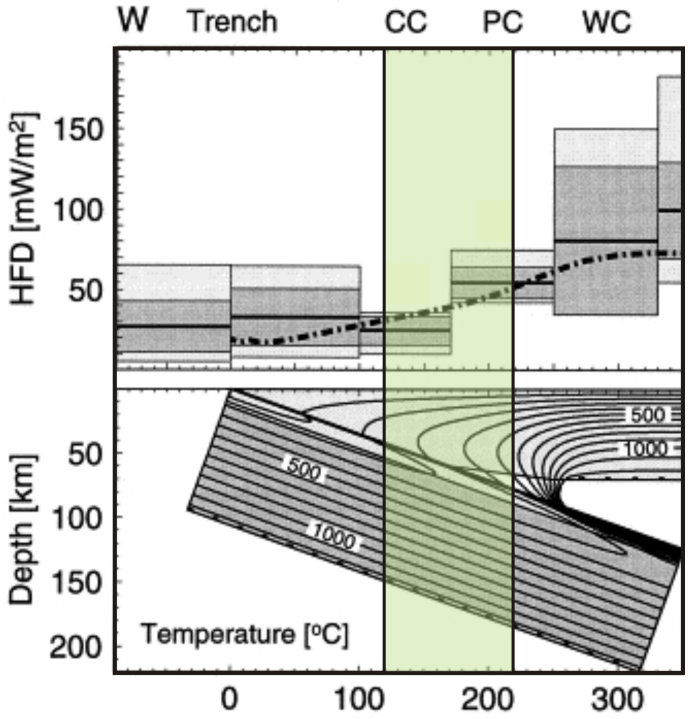

Figure 4.15: Modified from Springer (1999). The upper panel compares measured heat-flow density (HFD, horizontal solid black lines) for different morpho-tectonic units (CC - Coastal Cordillera, PC - Precordillera, WC - Western Cordillera) and surface heat-flow density obtained from 2D temperature model calculation (dashed/dotted line) between 15° and 30°S. Shaded areas indicate confidence limits of measured HFD values. The 2D temperature model is plotted in the lower panel. Green shaded area indicates the longitudinal extent of the IPOC MT network.

tinuous inter-seismically fluid flow upwards, resulting in hydration of the mantle wedge above. Such a hydrated mantle wedge may be imaged as high-conductive structure (II) in this study.

Evans (2002) suggested that only offshore MT data can resolve a hydrated mantle wedge at an ocean-continent subduction zone. In contrast, I image a conductive feature at the Andean subduction zone in Northern Chile at the location of the hydrated mantle wedge using exclusively onshore data including VTFs. As mentioned in section 4.3, structure (II) was found by 3D inversion only if the smaller off-diagonal component Z_{xy} is weighted appropriately by setting individual error bounds for all impedance tensor elements.

The result of 3D forward modelling of varying VTFs indicates an increase in electrical

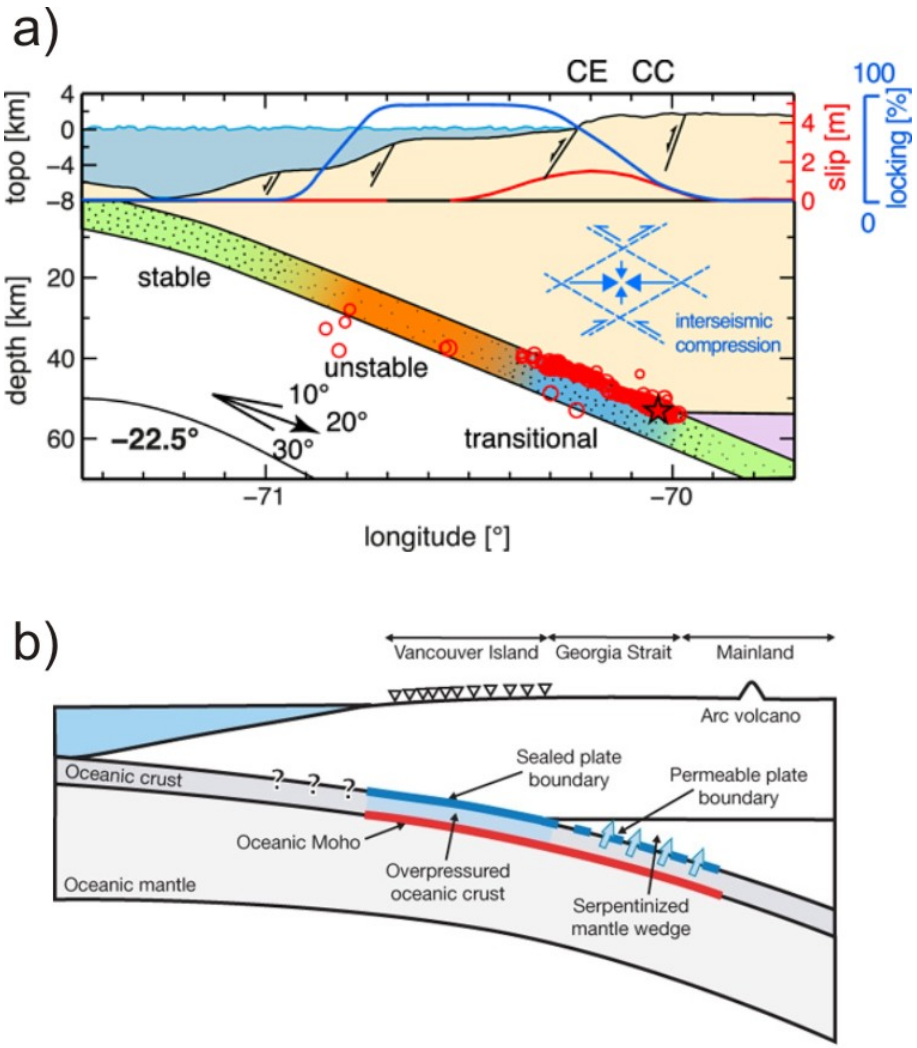

Figure 4.16: a) Compilation of seismological results from Schurr et al. (2012) (CC - Coastal Cordillera, CE - Coastal Escarpment). Red circles indicate projected aftershock locations from the section 15 km north and south of 22.5°S. The red curve indicates slip of the Tocopilla earthquake, the blue curve shows the locking of the seismogenic zone. See also caption of Figure 2.4. b) Schematic interpretation of receiver function results from Northern Cascadia subduction zone (Fig. taken from Audet et al., 2009).

conductivity of 1.5 to 2.5 orders of magnitude in a volume of approximately 90 x 60 x 25 km^3 (Fig. 4.11). This increase occurs roughly at the intersection of the slab with the continental Moho for a period of approximately one and a half years following the Tocopilla main shock. It is remarkable that the location of our anomalous zone appears to be located directly down-dip of the M7.7 2007 Tocopilla main shock at the plate interface of the

subduction zone. This anomalous zone differs in space and time significantly from large scale fluid flow above the rupture plane of the Mw8.1 1995 Antofagasta earthquake as interpreted by Husen & Kissling (2001) based on increased vp/vs ratios during 30 days after the Antofagasta Earthquake. Schurr et al. (2012) suggested that the slip of the M7.7 2007 Tocopilla earthquake reduced stress in the locked segment and transition zone of the thrust interface but, simultaneously, increased the stress in the adjacent down-dip segment. The temporarily varying resistivity structure is located directly down-dip of the transition zone in the aseismic creeping zone (Fig. 4.16 a). I speculate that co-seismical increase of stress in this subduction segment causes an enhanced fluid migration into the overlying mantle wedge. Higher volumes of fluids cause the observed increase in electrical conductivity during one and a half years after rupturing this zone. Subsequently, aseismic creep reduces stress in this segment, and the excess of fluids may gradually be dissipated and the initial state of electrical conductivity in this volume may be recovered. Future studies with a denser site spacing could refine the inversion model and, thus, the anomalous volume of varying electrical resistivity.

CHAPTER 5

Summary

The magnetotelluric (MT) component of the IPOC network is a unique opportunity to study the dynamic behaviour of an active deep subduction system and to push the knowledge frontier about using MT for monitoring. In total, nine permanent MT observation sites were installed since 2006 in Northern Chile to detect possible changes of the electrical resistivity structure associated with the deep hydraulic system of the Andean subduction zone. In this thesis, I describe the novel concepts which were developed for monitoring purposes and results obtained from processing and interpreting more than 4 years of electromagnetic (EM) data.

A major issue for MT monitoring in the hyper-arid climate of the Atacama is stable recording of electric field data. I developed a concept for the installation of Ag/AgCL electrodes which makes it possible to leave the electrodes unattended in the ground for more than one year. To my knowledge, it was not possible before to leave Ag/AgCL electrodes in such conditions for more than three months. Tools and techniques were developed to automatically add data to the IPOC-MT database, either read-out directly on site or transmitted by satellite. Also I coded an automatic data processing scheme to handle the enormous data volume.

Time series of vertical magnetic transfer functions (VTF) of more than four years reveal strong seasonal variation caused by a geomagnetic source field inhomogeneity. For EM depth sounding methods, we assume spatially uniform sources generated far away from the observation point at Earth's surface. As this assumption is violated in Northern Chile, all east-west components of the VTFs (T_y) vary with season. As a consequence, induction vectors in local summer are systematically smaller and deviated towards SW when compared to winter observations. At some periods and sites the variation amplitudes exceed 100% of the absolute value of T_y. If not taken into account, this can lead to biased MT modelling and consequently to misinterpretation of the data.

Time series of power spectral densities (PSD) of horizontal and vertical magnetic fields

recorded at seven of the monitoring stations revealed the cause for this source field inhomogeneity. The magnetic fields exhibit a pronounced temporal variation of the east-west component with an amplitude of approximately 5 dB for periods between 100 and several thousand seconds. This pronounced variation of B_y is observed between solstice seasons and daytime and nighttime. Seasonal variations are also observed for the north-south and vertical magnetic components but with 3 orders of magnitude smaller power. The ratio between north-south magnetic field and east-west electric field is constant throughout the seasons and also for day and night. In contrast, the ratio between east-west magnetic field and north-south electric field varies with day time and season. Using segments of a day computing PSDs shows that the seasonal variation originates primarily from the time sector 08:00 to 16:00 LT.

To verify an influence of the interplanetary electric field (IEF) we used solar wind data from the Advanced Composition Explorer satellite. During summer, we observe for time sector 08:00 to 16:00 LT significant coherences between the interplanetary electric field component IEY and ground based electric and magnetic fields at periods of approximately 30 and 45 min. To our knowledge, it is the first time that significant coherences between satellite-based IEY and ground-based geo-electric field measurements could be established. Coherences between IEY and our ground based data vary with season and local time. Transfer functions computed between IEF and ground-based electric and magnetic fields show local maxima at periods of 90 min and harmonics. The coupling between the B_y component and the IEF shows significant seasonal variability, much larger than for the other electromagnetic field components.

We conclude that seasonal variations of VTFs are caused by two different ionospheric currents systems. A global circuit of Pedersen currents in the ionosphere is primarily driven by the IEF. Resulting time-varying magnetic fields induce electric currents in the ground. Related ground-based magnetic (primarily north-south) and electric (primarily east-west) fields vary coherently at all local times and seasons. Conversely, magnetic fields caused by the IEF-driven Hall currents depend much on local time and season. We show for the first time that these ionospheric Hall currents cause no induction in the ground but generate magnetic signatures that are confined to the waveguide between ionosphere and Earth's surface.

After removing the seasonal variation from VTF time-series I observe significant long-term variation of VTFs over a time span of approximately 1.5 years in the aftermath of the M7.7 2007 Tocopilla earthquake. This variation is limited to two adjacent monitoring sites and a period range of 1000 to several thousand seconds. Using eight monitoring stations of the network, I computed as reference a 3D inversion model imaging the regional electrical resistivity structure of this segment of the plate boundary. The resulting resistivity struc-

tures are generally in good agreement with seismological data. A zone of high electrical conductivity below a depth of 30 km coincides spatially with a region where the hydrated mantle wedge is expected. Resolution tests confirmed the sensitivity of the predicted data to this conductor. Subsequently, the 3D reference model was systematically altered to simulate the observed variations of VTFs with forward modelling. Eventually, I could identify an approximately 100 by 50 km wide and 20 km thick region at a depth of 50 km where increased electrical conductivity can explain the observed temporal variation in the VTFs. This volume of temporary higher conductivity is located directly down-dip of the transition zone of the thrust interface in the aseismic creeping segment and below the tip of the conductive material associated with the hydrated mantle wedge. I speculate that co-seismic increase of stress in this permeable subduction segment causes enhanced fluid migration upwards into the overlying mantle wedge. Higher volumes of fluids cause the observed increase in electrical conductivity for one and a half years after rupturing this zone. Subsequently, aseismic creep reduces stress in this segment, and the excess of fluids may gradually be dissipated and the initial state of electrical conductivity in this volume may be recovered. Future studies with denser site spacing could refine the inversion model and, thus, the anomalous volume of varying electrical resistivity.

Acknowledgements

Completing this doctoral thesis has been a fantastic experience, but at times also a challenge. Many people have contributed in one way or another, to only some of them I can give particular mention here.

Foremost, I would like to express my sincere gratitude to my supervisor PD Dr. Oliver Ritter for his continued encouragement and invaluable suggestions during this work. He introduced me to the Chilean Atacama Desert and the already existing IPOC stations. I am grateful for inspiring discussions about the ideas behind using MT for monitoring, the opportunity to visit national and international conferences and, in particular, the freedom to develop my own scientific ideas. The field campaigns all over the world were also a great experience.

I am deeply indebted to Prof. Dr. Hermann Lühr who greatly helped me with his comprehensive knowledge of geomagnetic fields. He increased my understanding of the magnetosphere in many discussions and helped to clarify ideas for publishing parts of this thesis.

I would like to express my very great appreciation to Prof. Dr. Guillermo Chong Díaz who made the measurements in the Chilean Desert possible and supported our field campaigns. I also would like to include my gratitude to Prof. Dr. Gabriel González López for the logistic help in Antofagasta. Without the comprehensive knowledge of PD Dr. Günter Asch of how to run autonomous stations unattended for several months in the Atacama Desert, this work would not have been possible.

I am very thankful to Dr. Ute Weckmann who helped to manage and carry out the installation of the IPOC monitoring sites in Northern Chile. Also, I would like to acknowledge her kind help during my first days at GFZ. I would like to thank Thomas Krings, who began working with the IPOC-MT data, for sharing his experiences and insights.

I want to express my special thanks to Dr. Kristina Tietze for her enduring help in two great but very demanding field trips to Chile. As we shared the office I enjoyed numerous discussions about MT and many other things. I am particularly grateful to Dr. Naser Meqbel who helped me a lot with the MODEM 3D inversion scheme and who improved my understanding about MT inversion greatly. I also enjoyed many conversations with him about science and beyond. Advice given by Dr. Rita Streich has been a great help concerning numerical problems. Also, help from Paul Sass during one field trip to Chile

was invaluable. I would like to thank Dr. Gerard Muñoz for increasing my understanding of the MT method in many discussions on the theoretical background.

Without the kind help of Prof. Klaus Batallie in Concepcion, the field trip to Isla Mocha would not have been possible. Also I would like to thank Amerika Manzanares who ensured the availability of satellite data. I want to thank Carsten Müller and Stefan Rettig from the Niemegk Observatory for help with the instruments and Raul Patricio Ortiz for the hard work in the Desert installing MT equipment.

I am very grateful to all my present and former colleagues of the Geo-Electromagnetics working group at GFZ for the inspiring and friendly working atmosphere. I would like to acknowledge particularly those who provided many comments and corrections on earlier versions of this thesis. Sintia Windhi was an awesome officemate, thank you.

The MT working group (MT-AG), consisting of the Geo-Electromagnetics working groups of Free University Berlin (Dr. Heinrich Brasse) and GFZ Potsdam, provided an excellent opportunity to discuss new scientific ideas.

I would like to thank the IPOC working group for providing the technical infrastructure and to discuss my results over the years. This project and in particular my PhD position was funded by the GFZ German Research Centre for Geosciences. The instruments for the experiments were initially provided by the Geophysical Instrument Pool Potsdam (GIPP).

Bibliography

Allmendinger, R. W. & González, G., 2010. Invited review paper: Neogene to Quaternary tectonics of the coastal Cordillera, northern Chile, *Tectonophysics*, **495**(1-2), 93–110.

Allmendinger, R. W., Jordan, T. E., Kay, S. M., & Isacks, B. L., 1997. The Evolution of the Altiplano-Puna Plateau of the Central Andes, *Annual Review of Earth and Planetary Sciences*, **25**(1), 139–174.

Anderson, C. W., Lanzerotti, L. J., & Maclennan, C. G., 1976. Local time variation of induction vectors as indicators of internal and external current systems, *Geophysical Research Letters*, **3**(8), 495.

Angermann, D., Klotz, J., & Reigber, C., 1999. Space-geodetic estimation of the Nazca-South America Euler vector, *Earth and Planetary Science Letters*, **171**(3), 329–334.

Audet, P., Bostock, M. G., Christensen, N. I., & Peacock, S. M., 2009. Seismic evidence for overpressured subducted oceanic crust and megathrust fault sealing., *Nature*, **457**(7225), 76–8.

Becken, M., Ritter, O., Bedrosian, P. A., & Weckmann, U., 2011. Correlation between deep fluids, tremor and creep along the central San Andreas fault., *Nature*, **480**(7375), 87–90.

Béjar-Pizarro, M., Carrizo, D., Socquet, a., Armijo, R., Barrientos, S., Bondoux, F., Bonvalot, S., Campos, J., Comte, D., de Chabalier, J. B., Charade, O., Delorme, a., Gabalda, G., Galetzka, J., Genrich, J., Nercessian, a., Olcay, M., Ortega, F., Ortega, I., Remy, D., Ruegg, J. C., Simons, M., Valderas, C., & Vigny, C., 2010. Asperities and barriers on the seismogenic zone in North Chile: state-of-the-art after the 2007 Mw 7.7 Tocopilla earthquake inferred by GPS and InSAR data, *Geophysical Journal International*, **183**(1), 390–406.

Brändlein, D., Lühr, H., & Ritter, O., 2012. Direct penetration of the interplanetary electric field to low geomagnetic latitudes and its effect on magnetotelluric sounding, *Journal of Geophysical Research*, **117**(A11), A11314.

Brasse, H. & Eydam, D., 2008. Electrical conductivity beneath the Bolivian Orocline and its relation to subduction processes at the South American continental margin, *Journal of Geophysical Research*, **113**(B7), B07109.

Brasse, H., Lezaeta, P., Rath, V., Schwalenberg, K., Soyer, W., & Haak, V., 2002. The Bolivian Altiplano conductivity anomaly, *Journal of Geophysical Research*, **107**(B5), 2096.

Cagniard, L., 1953. Basic theory of the magneto-telluric method of geophysical prospecting, *Geophysics*, **18**(3), 605–635.

Cahill, T. & Isacks, B. L., 1992. Seismicity and shape of the subducted Nazca Plate, *Journal of Geophysical Research*, **97**(B12), 17503.

Chlieh, M., de Chabalier, J. B., Ruegg, J. C., Armijo, R., Dmowska, R., Campos, J., & Feigl, K. L., 2004. Crustal deformation and fault slip during the seismic cycle in the North Chile subduction zone, from GPS and InSAR observations, *Geophysical Journal International*, **158**(2), 695–711.

Chong, G., 1984. *Die Salare in Nordchile*, Schweizerbart'sche Verlagsbuchhandlung, Stuttgart.

Comte, D. & Pardo, M., 1991. Reappraisal of great historical earthquakes in the northern Chile and southern Peru seismic gaps, *Natural Hazards*, **4**(1), 23–44.

Delouis, B., Monfret, T., Dorbath, L., Pardo, M., Rivera, L., Comte, D., Haessler, H., Caminade, J., Ponce, L., Kausel, E., et al., 1997. The $M_w = 8.0$ Antofagasta (Northern Chile) Earthquake of 30 July 1995: A Precursor to the End of the Large 1877 Gap, *Bulletin of the Seismological Society of America*, **87**(2), 427–445.

Du, J. & Stening, R. J., 1999. Simulating the ionospheric dynamo-I. Simulation model and flux tube integrated conductivities, *Journal of Atmospheric and Solar-Terrestrial Physics*, **61**(12), 913–923.

Earle, G. D. & Kelley, M. C., 1987. Spectral studies of the sources of ionospheric electric fields, *Journal of Geophysical Research*, **92**(A1), 213.

Echternacht, F., Tauber, S., Eisel, M., Brasse, H., Schwarz, G., & Haak, V., 1997. Electromagnetic study of the active continental margin in northern Chile, *Physics of the Earth and Planetary Interiors*, **102**(1-2), 69–87.

Egbert, G. D., 2002. Processing And Interpretation Of Electromagnetic Induction Array Data, *Surveys in Geophysics*, **23**(2-3), 207–249.

Egbert, G. D. & Kelbert, A., 2012. Computational recipes for electromagnetic inverse problems, *Geophysical Journal International*, **189**(1), 251–267.

Egbert, G. D., Eisel, M., Boyd, O. S., & Morrison, H. F., 2000. DC trains and Pc3s: Source effects in mid-latitude geomagnetic transfer functions, *Geophysical Research Letters*, **27**(1), 25.

Eisel, M. & Egbert, G. D., 2001. On the stability of magnetotelluric transfer function estimates and the reliability of their variances, *Geophysical Journal International*, **144**(1), 65–82.

Evans, R. L., 2002. On the importance of offshore data for magnetotelluric studies of ocean-continent subduction systems, *Geophysical Research Letters*, **29**(9), 1302.

Guéguen, Y. & Palciauskas, V., 1994. *Introduction to the Physics of Rocks*, Princeton Univ. Press, Princeton, N.J.

Hacker, B. R., 2008. H2O subduction beyond arcs, *Geochemistry Geophysics Geosystems*, **9**(3), Q03001.

Hartley, A. J. & Evenstar, L., 2010. Cenozoic stratigraphic development in the north Chilean forearc: Implications for basin development and uplift history of the Central Andean margin, *Tectonophysics*, **495**(1-2), 67–77.

Husen, S. & Kissling, E., 2001. Postseismic fluid flow after the large subduction earthquake of Antofagasta, Chile, *Geology*, **29**(9), 847–850.

Hyndman, R. D. & Peacock, S. M., 2003. Serpentinization of the forearc mantle, *Earth and Planetary Science Letters*, **212**(3-4), 417–432.

Hyndman, R. D., Yamano, M., & Oleskevich, D. A., 1997. The seismogenic zone of subduction thrust faults, *The Island Arc*, **6**(3), 244–260.

Kappler, K. N., Morrison, H. F., & Egbert, G. D., 2010. Long-term monitoring of ULF electromagnetic fields at Parkfield, California, *Journal of Geophysical Research*, **115**(B4), B04406.

Kawasaki, K. & Akasofu, S.-I., 1972. Geomagnetic disturbances in the polar cap: Spq and DP-2, *Planetary and Space Science*, **20**(8), 1163–1172.

Kikuchi, T., Araki, T., Maeda, H., & Maekawa, K., 1978. Transmission of polar electric fields to the Equator, *Nature*, **273**(5664), 650–651.

Kikuchi, T., Lühr, H., Kitamura, T., Saka, O., & Schlegel, K., 1996. Direct penetration of the polar electric field to the equator during a DP 2 event as detected by the auroral and equatorial magnetometer chains and the EISCAT radar, *Journal of Geophysical Research*, **101**(A8), 17161.

Krings, T., 2007. *The influence of robust statistics, remote reference, and horizontal magnetic transfer functions on data processing in magnetotellurics*, Diploma thesis, WWU Münster-GFZ Potsdam, Potsdam, Germany.

Lezaeta, P., 2001. *Distortion analysis and 3-D modeling of magnetotelluric data in the southern central Andes*, Ph.D. thesis, Fachber. Geowiss., Freie Universität Berlin, Germany.

Lezaeta, P., Chave, A., Jones, A. G., & Evans, R., 2007. Source field effects in the auroral zone: Evidence from the Slave craton (NW Canada), *Physics of the Earth and Planetary Interiors*, **164**, 21–35.

Manoj, C., Maus, S., Lühr, H., & Alken, P., 2008. Penetration characteristics of the interplanetary electric field to the daytime equatorial ionosphere, *Journal of Geophysical Research*, **113**(A12), A12310.

Matsushita, S. & Balsley, B. B., 1972. A question of DP-2, *Planetary and Space Science*, **20**(8), 1259–1267.

Meqbel, N. M. M., 2009. *The electrical conductivity structure of the Dead Sea Basin derived from 2D and 3D inversion of magnetotelluric data*, Phd thesis, Fachber. Geowiss., Freie Universität Berlin, Germany.

Motagh, M., Schurr, B., Anderssohn, J., Cailleau, B., Walter, T. R., Wang, R., & Villotte, J.-P., 2010. Subduction earthquake deformation associated with 14 November 2007, Mw 7.8 Tocopilla earthquake in Chile: Results from InSAR and aftershocks, *Tectonophysics*, **490**(1-2), 60–68.

Nadeau, R. M. & Dolenc, D., 2005. Nonvolcanic tremors deep beneath the San Andreas Fault., *Science (New York, N.Y.)*, **307**(5708), 389.

Nicolls, M. J., Kelley, M. C., Chau, J. L., Veliz, O., Anderson, D., & Anghel, A., 2007. The spectral properties of low latitude daytime electric fields inferred from magnetometer

observations, *Journal of Atmospheric and Solar-Terrestrial Physics*, **69**(10-11), 1160–1173.

Nishida, A., 1968a. Geomagnetic Dp 2 fluctuations and associated magnetospheric phenomena, *Journal of Geophysical Research*, **73**(5), 1795–1803.

Nishida, A., 1968b. Coherence of geomagnetic DP 2 fluctuations with interplanetary magnetic variations, *Journal of Geophysical Research*, **73**(17), 5549–5559.

Obara, K., 2002. Nonvolcanic deep tremor associated with subduction in southwest Japan, *Science (New York, N.Y.)*, **296**(5573), 1679–81.

Oncken, O., Hindle, D., Kley, J., Elger, K., Victor, P., & Schemmann, K., 2006. Deformation of the Central Andean Upper Plate System - Facts, Fiction, and Constraints for Plateau Models, in *The Andes*, Frontiers in Earth Sciences, pp. 3–27, eds Oncken, O., Chong, G., Franz, G., Giese, P., Gtze, H.-J., Ramos, V., Strecker, M., & Wigger, P., Springer Berlin Heidelberg.

Park, S. K., 1991. Monitoring resistivity changes prior to earthquakes in Parkfield, California, with telluric arrays, *Journal of Geophysical Research*, **96**(B9), 14211.

Park, S. K., 1996. Precursors to earthquakes: Seismoelectromagnetic signals, *Surveys in Geophysics*, **17**(4), 493–516.

Parker, R. L., 1980. The inverse problem of electromagnetic induction: Existence and construction of solutions based on incomplete data, *Journal of Geophysical Research*, **85**(B8), 4421.

Parzen, E., 1962. On estimation of a probability density function and mode, *The annals of mathematical statistics*, **33**(3), 1065–1076.

Peacock, S. A., 1990. Fluid processes in subduction zones, *Science (New York, N.Y.)*, **248**(4953), 329–37.

Peacock, S. M. & Hyndman, R. D., 1999. Hydrous minerals in the mantle wedge and the maximum depth of subduction thrust earthquakes, *Geophysical Research Letters*, **26**(16), 2517–2520.

Raleigh, C. B. & Paterson, M. S., 1965. Experimental deformation of serpentinite and its tectonic implications, *Journal of Geophysical Research*, **70**(16), 3965.

Ritter, O., Junge, A., & Dawes, G., 1998. New equipment and processing for magnetotelluric remote reference observations, *Geophysical Journal International*, **132**(3), 535–548.

Rogers, G. & Dragert, H., 2003. Episodic tremor and slip on the Cascadia subduction zone: the chatter of silent slip, *Science (New York, N.Y.)*, **300**(5627), 1942–3.

Rüpke, L., 2004. Serpentine and the subduction zone water cycle, *Earth and Planetary Science Letters*, **223**(1-2), 17–34.

Scheuber, E. & Reutter, K.-J., 1992. Magmatic arc tectonics in the Central Andes between 21° and 25°S, *Tectonophysics*, **205**(1-3), 127–140.

Schmidt, M. W. & Poli, S., 1998. Experimentally based water budgets for dehydrating slabs and consequences for arc magma generation, *Earth and Planetary Science Letters*, **163**(1-4), 361–379.

Schmucker, U., 1969. Conductivity anomalies, with special reference to the Andes, in *Applications of Modern Physics to the Earth and Planetary Interiors*, pp. 125–138, ed. S.K. Runcorn, 1969, New York, interscien edn.

Schmucker, U., 1987. Substitute conductors for electromagnetic response estimates, *Pure and Applied Geophysics*, **125**(2-3), 341–367.

Schurr, B., Asch, G., Rosenau, M., Wang, R., Oncken, O., Barrientos, S., Salazar, P., & Vilotte, J.-P., 2012. The 2007 M7.7 Tocopilla northern Chile earthquake sequence: Implications for along-strike and downdip rupture segmentation and megathrust frictional behavior, *Journal of Geophysical Research*, **117**(B5), B05305.

Schwarz, G. & Krüger, D., 1997. Resistivity cross section through the southern central Andes as inferred from magnetotelluric and geomagnetic deep soundings, *Journal of Geophysical Research*, **102**(B6), 11957.

Segall, P., 1989. Earthquakes triggered by fluid extraction, *Geology*, **17**(10), 942.

Shankland, T. J. & Ander, M. E., 1983. Electrical conductivity, temperatures, and fluids in the lower crust, *Journal of Geophysical Research*, **88**(B11), 9475.

Sodoudi, F., Yuan, X., Asch, G., & Kind, R., 2011. High-resolution image of the geometry and thickness of the subducting Nazca lithosphere beneath northern Chile, *Journal of Geophysical Research*, **116**(B4), B04302.

Springer, M., 1999. Interpretation of heat-flow density in the Central Andes, *Tectonophysics*, **306**(3-4), 377–395.

Stern, R. J., 2002. Subduction zones, *Reviews of Geophysics*, **40**(4).

Sutcliffe, P. R. & Lühr, H., 2010. A search for dayside geomagnetic Pi2 pulsations in the CHAMP low-Earth-orbit data, *Journal of Geophysical Research*, **115**(A5), A05205.

Thompson, R. O. R. Y., 1979. Coherence significance levels, *Journal of Atmospheric Sciences*, **36**, 2020–2021.

Tietze, K., 2012. *Investigating the electrical conductivity structure of the San Andreas fault system in the Parkfield-Cholame region, central California, with 3D magnetotelluric inversion*, Ph.D. thesis, Fachber. Geowiss., Freie Universität Berlin, Germany.

Tietze, K. & Ritter, O., 2013. Three-dimensional magnetotelluric inversion in practice–the electrical conductivity structure of the San Andreas Fault in Central California, *Geophysical Journal International*.

Tikhonov, A. N., 1950. On determining electrical characteristics of the deep layers of the earth's crust, *Dokl. Akad. Nauk SSSR*, **73**(2), 295–297.

Victor, P., Sobiesiak, M., Glodny, J., Nielsen, S. N., & Oncken, O., 2011. Long-term persistence of subduction earthquake segment boundaries: Evidence from Mejillones Peninsula, northern Chile, *Journal of Geophysical Research*, **116**(B2), B02402.

von Huene, R., 2003. Subduction erosion and basal friction along the sediment-starved convergent margin off Antofagasta, Chile, *Journal of Geophysical Research*, **108**(B2), 2079.

von Huene, R. & Scholl, D. W., 1991. Observations at convergent margins concerning sediment subduction, subduction erosion, and the growth of continental crust, *Reviews of Geophysics*, **29**(3), 279.

Weckmann, U., Magunia, a., & Ritter, O., 2005. Effective noise separation for magnetotelluric single site data processing using a frequency domain selection scheme, *Geophysical Journal International*, **161**(3), 635–652.

Wiese, H., 1962. Geomagnetische Tiefentellurik Teil II: Die Streichrichtung der untergrundstrukturen des elektrischen Widerstandes, erschlossen aus geomagnetischen Variationen, *Geofisica Pura e Applicata*, **52**(1), 83–103.

Appendix

PB01	Installation	02.05.2007
	Coordinates	W −69.48705 ° S −21.042792 °
	EDL	6037
	SBX	42
	Geomagnet	15
	Dipole length	X 80,3 m Y 81,4 m
	Contact resistivities	EX G 0,07 E+ 75,79 E- 0,12 kΩ EY G 0,07 E+ 75,79 E- 0.15 kΩ
PB02	Installation	03.05.2007
	Coordinates	W −69.896014 ° S −21.319614 °
	EDL	6033
	SBX	66
	Geomagnet	12
	Dipole length	X 80,9 m Y 84,8 m
	Contact resistivities	EX G 1,52 E+ 39,79 E- 1,33 kΩ EY G 1,56 E+ 2,63 E- 52.58 kΩ

PB03	Installation	07.03.2007
	Coordinates	W −69.753244 ° S −22.048456 °
	EDL	6039
	SBX	48
	Geomagnet	13
	Dipole length	X 80,4 m Y 71,5 m
	Contact resistivities	EX G 0,22 E+ 1,18 E- 625,7 kΩ EY G 0,4 E+ 0,83 E- 704,04 kΩ
PB04	Installation	10.03.2007
	Coordinates	W −70.149414 ° S −22.333639 °
	EDL	6040
	SBX	25
	Geomagnet	9
	Dipole length	X 100,0 m Y 101,3 m
	Contact resistivities	EX G 1,52 E+ 39,79 E- 1,33 kΩ EY G 1,56 E+ 2,63 E- 52,58 kΩ
PB05	Installation	09.03.2007
	Coordinates	W −70.202458 ° S −22.852742 °
	EDL	6041
	SBX	43
	Geomagnet	17
	Dipole length	X 80,0 m Y 81,3 m
	Contact resistivities	EX G 1,2 E+ 36,42 E- 14,57 kΩ EY G 6,18 E+ 19,19 E- 9,22 kΩ

PB06	Installation	27.02.2007
	Coordinates	W −69.572006 ° S −22.705772 °
	EDL	6032
	SBX	24
	Geomagnet	6
	Dipole length	X 79,3 m Y 80,8 m
	Contact resistivities	EX G 0,12 E+ 330,42 E- 0,31 kΩ EY G 0,30 E+ 253,22 E- 0,11 kΩ
PB07	Installation	06.03.2007
	Coordinates	W −69.886181 ° S −21.72675 °
	EDL	6038
	SBX	23
	Geomagnet	7
	Dipole length	X 81,3 m Y 80,5 m
	Contact resistivities	EX G 0,29 E+ 3,22 E- 759,19 kΩ EY G 0,05 E+ 2358,18 E- 2,85 kΩ

PB09	Installation	20.04.2010
	Coordinates	W $-69.2419\,^\circ$ S $-21.7964\,^\circ$
	EDL	6010
	SBX	90
	Geomagnet	24
	Dipole length	X 80,8 m Y 80,0 m
	Contact resistivities	EX G 0,29 E+ 3,22 E- 759,19 kΩ EY G 0,05 E+ 2358,18 E- 2,85 kΩ
PB15	Installation	04.08.2011
	Coordinates	W $-69.47293\,^\circ$ S $-23.20733\,^\circ$
	EDL	6031
	SBX	21
	Geomagnet	16
	Dipole length	X 80,8 m Y 80,7 m
	Contact resistivities	EX G 84,08 E+ 87,55 E- 0,18 kΩ EY G 80,65 E+ 32,96 E- 65,94 kΩ

Table 1: All contact resistivities are measured in august 2011 and represent the state of the optimised electrodes.

Erklärung

Hiermit versichere ich, dass ich die vorliegende Dissertation selbständig ohne Hilfe Dritter verfasst habe. Andere als die angegebenen Quellen und Hilfsmittel wurden nicht verwendet. Die den benutzten Quellen wörtlich oder dem Sinn nach entnommen Abschnitte sind als solche kenntlich gemacht. Dies gilt auch für Zeichnungen, Skizzen, bildliche Darstellungen und dergleichen, sowie für Quellen aus dem Internet. Die Dissertation hat in dieser oder ähnlicher Form weder ganz noch in Teilen einer in- oder ausländischen Hochschule zum Zwecke der Promotion vorgelegen.

Teile von Kapitel 3 sind veröffentlicht in:

Brändlein, D., Lühr, H. & Ritter, O., 2012. Direct penetration of the interplanetary electric field to low geomagnetic latitudes and its effect on magnetotelluric sounding, *Journal of Geophysical Research*, 117, A11314.

Berlin, 02. Juni 2013 _____

Curriculum Vitae

For reasons of data protection, the curriculum vitae is not included in the online version.

Aus Gründen des Datenschutzes erscheint der Lebenslauf nicht in der elektronischen Fassung.

Publications

Paper (ISI journals)

Brändlein, D., Lühr, H. & Ritter, O., 2012. Direct penetration of the interplanetary electric field to low geomagnetic latitudes and its effect on magnetotelluric sounding, *Journal of Geophysical Research*, 117, A11314.

Invited Talks

Brändlein, D., Ritter, O. & Weckmann, U., 2012. A permanent array of magnetotelluric stations located at the South American subduction zone in Northern Chile, Universidad de Concepcion, Chile.

Conference paper

2012

Brändlein, D., Ritter, O. & Weckmann, U., 2012. The influence of seasonally varying geomagnetic source fields on magnetotelluric monitoring in Northern Chile, *21st IAGA WG 1.2 Workshop on Electromagnetic Induction in the Earth*, Darwin (Australia).

Brändlein, D. & Ritter, O., 2012. Electrical resistivity of the mantle at the South American subduction system in Northern Chile, in *Proceedings of the 24th Schmucker-Weidelt-Colloquium on Electromagnetic Depth Sounding*, Neustadt / Weinstr. (Germany). ISSN 0946-7467.

2011

Brändlein, D., Ritter, O. & Weckmann, U., 2011. A permanent array of magnetotelluric stations located at the South American subduction zone in Northern Chile, *24th Schmucker-Weidelt-Colloquium on Electromagnetic Depth Sounding*, Neustadt / Weinstr. (Germany).

Brändlein, D., Ritter, O. & Weckmann, U., 2011. A permanent array of magnetotelluric stations located at the South American subduction zone in Northern Chile, *71th annual meeting of the German Geophysical Society (DGG)*, Köln (Germany).

Brändlein, D., Ritter, O. & Weckmann, U., 2011. A permanent array of magnetotelluric stations located at the South American subduction zone in Northern Chile, *22. Colloquium on Latin American Earth Sciences (LAK)*, Heidelberg (Germany).

2010

Brändlein, D., Ritter, O. & Weckmann, U., 2010. A permanent array of magnetotelluric stations located at the South American subduction zone in Northern Chile, in *Proceedings of the 23rd Schmucker-Weidelt-Colloquium on Electromagnetic Depth Sounding*, Seddiner See (Germany). ISSN 2190-7021.

Brändlein, D., Ritter, O., Weckmann, U. & Tietze, K., 2010. A permanent array of magnetotelluric stations located at the South American subduction zone in Northern Chile, *20th IAGA WG 1.2 Workshop on Electromagnetic Induction in the Earth*, Giza (Egypt).

Brändlein, D., Ritter, O., Weckmann, U., & Tietze, K., 2010. A permanent array of magnetotelluric stations located at the South American subduction zone in Northern Chile, *General Assembly European Geosciences Union*, Vienna (Austria).

Brändlein, D., Ritter, O., Weckmann, U., & Tietze, K., 2010. A permanent array of magnetotelluric stations located at the South American subduction zone in Northern Chile, *70th annual meeting of the German Geophysical Society (DGG)*, Bochum (Germany).

Brasse, H., Diaz, D., **Brändlein, D.**, Ticona, F., 2010. Magnetotelluric studies of the Central Andean volcanic arc, *70th annual meeting of the German Geophysical Society (DGG)*, Bochum (Germany).

2009

Brändlein, D., Ritter, O. & Weckmann, U., 2009. A permanent array of magnetotelluric stations located at the South American subduction zone in Northern Chile, *23rd Schmucker-Weidelt-Colloquium on Electromagnetic Depth Sounding*, Seddiner See (Germany).